



**STUDY OF A TOROIDAL DIELECTRIC LENS**

**VITOR CARVALHO DE ALMEIDA**

**DISSERTAÇÃO DE MESTRADO EM ENGENHARIA ELÉTRICA  
DEPARTAMENTO DE ENGENHARIA ELÉTRICA**

**FACULDADE DE TECNOLOGIA  
UNIVERSIDADE DE BRASÍLIA**

**UNIVERSIDADE DE BRASÍLIA  
FACULDADE DE TECNOLOGIA  
DEPARTAMENTO DE ENGENHARIA ELÉTRICA**

**STUDY OF A TOROIDAL DIELECTRIC LENS**

**ESTUDO DE UMA LENTE DIELÉTRICA TOROIDAL**

**VITOR CARVALHO DE ALMEIDA**

**ORIENTADOR: PROF. DR. SÉBASTIEN R.M.J. RONDINEAU**

**DISSERTAÇÃO DE MESTRADO EM ENGENHARIA  
ELÉTRICA**

**PUBLICAÇÃO: PPGEA.TD-788/22**

**BRASÍLIA/DF: JUNHO - 2022**

**UNIVERSIDADE DE BRASÍLIA  
FACULDADE DE TECNOLOGIA  
DEPARTAMENTO DE ENGENHARIA ELÉTRICA**

**STUDY OF A TOROIDAL DIELECTRIC LENS**

**VITOR CARVALHO DE ALMEIDA**

**DISSERTAÇÃO DE MESTRADO SUBMETIDA AO DEPARTAMENTO DE ENGENHARIA ELÉTRICA DA  
FACULDADE DE TECNOLOGIA DA UNIVERSIDADE DE BRASÍLIA COMO PARTE DOS REQUISITOS  
NECESSÁRIOS PARA A OBTENÇÃO DO GRAU DE MESTRE.**

**APROVADA POR:**

---

**Prof. Dr. Sébastien Roland Marie Joseph Rondineau – ENE/Universidade de Brasília  
Orientador**

---

**Prof. Dr. Leonardo Rodrigues Araujo Xavier de Menezes – ENE/Universidade de Brasília  
Membro Interno**

---

**Prof. Dr. Daniel Orquiza De Carvalho – ENE/Universidade de Brasília  
Suplente**

---

**Prof. Dr. Sebastian Yuri Cavalcanti Catunda – DCA/Universidade Federal do Rio Grande do Norte  
Membro Externo**

**BRASÍLIA, 30 DE JUNHO DE 2022.**

## FICHA CATALOGRÁFICA

ALMEIDA, VITOR CARVALHO DE

Study of a Toroidal Dielectric Lens [Distrito Federal] 2022.

xx, 109p., 210 x 297 mm (ENE/FT/UnB, Mestre, Engenharia Elétrica, 2022).

Dissertação de mestrado – Universidade de Brasília, Faculdade de Tecnologia.

Departamento de Engenharia Elétrica

1. Lente de Luneburg

2. Lente Toroidal

3. Formador de feixe

4. Banda X

I. ENE/FT/UnB

II. Título (série)

## REFERÊNCIA BIBLIOGRÁFICA

ALMEIDA, V. C. (2022). Study of a Toroidal Dielectric Lens . Dissertação de mestrado em Engenharia Elétrica, Publicação PPGEA.TD-788/22, Departamento de Engenharia Elétrica, Universidade de Brasília, Brasília, DF, 109p.

## CESSÃO DE DIREITOS

AUTOR: Vitor Carvalho de Almeida

TÍTULO: Study of a Toroidal Dielectric Lens .

GRAU: Mestre ANO: 2022

É concedida à Universidade de Brasília permissão para reproduzir cópias desta dissertação de mestrado e para emprestar ou vender tais cópias somente para propósitos acadêmicos e científicos. O autor reserva outros direitos de publicação e nenhuma parte dessa dissertação de mestrado pode ser reproduzida sem autorização por escrito do autor.

---

Vitor Carvalho de Almeida

Departamento de Engenharia Elétrica (ENE) - FT

Universidade de Brasília (UnB)

Campus Darcy Ribeiro

CEP 70919-970 - Brasília - DF - Brasil

## ACKNOWLEDGMENTS

*My sincere acknowledgement to my colleagues from the Telecommunications Laboratory, at University of Brasília, who gave me great support during my journey through the post graduation program. Thank you to the "RF guys": Matheus Pereira, Guilherme Felix, Jeann Feitosa, Vinicius Lisboa, Elpidio Araújo, and Daniel Souza. It was a pleasure to work and learn with all of you! Also, thank you to Kewin Kuster for all the very useful help with the research, and to André Felipe, who very patiently guided me through the details of 3D printing technology, and took his time to actively help me with the printing processes.*

*Thank you to my dissertation advisor, Sébastien Rondineau, for opening my mind to the great world of high frequency signals, also for his valuable time disposed to technical explanation, new ideas, and possible paths for solutions when I faced big problems. I am thankful not only for the technical help, but also for the advises about everything, the funny times on the laboratory, and for all those cups of coffee.*

*Thank you to my family for the education and support in all the moments of my life, specially during the hard and stressful times. Thank you Valdenor and Keila for being such great parents, and thank you to my sister Vanessa for all the times when we were studying together and supporting each other.*

## RESUMO

**Título:** Estudo de uma Lente Dielétrica Toroidal

**Autor:** Vitor Carvalho de Almeida

**Orientador:** Prof. Dr. Sébastien R.M.J. Rondineau

**Programa de Pós-Graduação em Engenharia Elétrica**

**Brasília, 30 de junho de 2022**

Este trabalho apresenta uma lente dielétrica em forma toroidal, particularmente construída com a distribuição de constante dielétrica utilizada em uma Lente de Luneburg. Este novo modelo de lente é caracterizado em termos de seu comprimento elétrico, com simulações realizadas em banda X. Devido à minimização de regiões de sombra, a lente toroidal pode irradiar em mais direções, em comparação com os formatos mais comumente encontrados na literatura, como esférico e cilíndrico. Dado o novo formato, também é apresentado um estudo dos impactos da curvatura do toróide no diagrama de radiação.

A lente toroidal pode ser utilizada em aplicações multicanal, utilizando um conjunto de antenas posicionadas ao longo de uma seção de sua superfície. Neste trabalho é utilizada uma guia de onda aberta, modelo WR90, mas outros tipos de antena também são sugeridos com base em trabalhos similares.

A lente foi fabricada utilizando tecnologia de impressão 3D. A permissividade elétrica do material utilizado na impressão foi caracterizada anteriormente, bem como seu modelo para variações na proporção de preenchimento. Além do comportamento eletromagnético, também foi realizado um estudo sobre as possíveis estruturas de célula unitária da lente impressa.

A análise computacional foi feita por meio de simulações utilizando o método dos elementos finitos. Entretanto, foi iniciado um estudo sobre um modelo analítico para a lente toroidal descrita em coordenadas toroidais.

A robustez da lente toroidal foi demonstrada pelas medições de diagrama de radiação, com resultados correspondendo satisfatoriamente às simulações.

**Palavras-chave:** Lente de Luneburg, Lente Toroidal, Formador de feixe, Banda X.

## **ABSTRACT**

**Title:** Study of a Toroidal Dielectric Lens

**Author:** Vitor Carvalho de Almeida

**Supervisor:** Prof. Dr. Sébastien R.M.J. Rondineau

**Graduate Program in Telecommunications and Communications Network Engineering**

**Brasília, June 30, 2022**

This work presents the studies about a dielectric lens with toroidal shape, particularly built with the distribution of dielectric constant used on a Luneburg Lens. This new model of lens is characterized in terms of its electrical length, with simulations performed at X-band. Due to the minimization of shadow regions, the toroidal lens can radiate in more directions, in comparison to the shapes most commonly found in the literature, such as spherical and cylindrical. Given the new shape, it is also presented a study of the impacts of the curvature of the torus on the radiation pattern.

The toroidal lens can be used in multi-channel applications, using a set of antennas placed along a section of its surface. In this work it is used a WR90 open-ended waveguide, but other types of antennas are also suggested based on similar works.

The lens was fabricated using 3D printing technology. The electrical permittivity of the material used on the printing was previously characterized, as well as its model for infill ratio variations. Besides the electromagnetic behavior, it was also done a study on the possible unit cell structure of the printed lens.

The computational analysis was done by simulations using finite element method. However, it is initiated a study of an analytical model for the toroidal lens described in toroidal coordinates.

The robustness of the toroidal lens was demonstrated by the radiation pattern measurements, with results having a great fit with simulations.

**Keywords:** Luneburg Lens, Toroidal Lens, Beamforming, X-band.

## SUMMARY

---

<b>1</b>	<b>INTRODUCTION.....</b>	<b>1</b>
1.1	APPLICATIONS.....	1
1.2	TOROIDAL LENS.....	2
1.3	STATE OF THE ART.....	4
1.3.1	CONFORMAL ANTENNAS.....	6
1.3.2	TOROIDAL LENS.....	8
1.4	ANALYTICAL METHODS.....	9
1.5	OBJECTIVES.....	9
1.5.1	MAIN OBJECTIVES.....	9
1.5.2	SPECIFIC OBJECTIVES.....	10
1.6	ORGANIZATION OF THE DISSERTATION.....	10
<b>2</b>	<b>DEFINITIONS.....</b>	<b>11</b>
2.1	COORDINATE SYSTEM.....	11
2.2	TRANSVERSE MODES.....	11
2.3	WAVEGUIDE.....	12
2.4	ANTENNA.....	12
2.4.1	APERTURE ANTENNA.....	13
2.5	FAR-FIELD.....	13
2.6	RADIATION PATTERN.....	14
2.6.1	DIRECTIVITY.....	14
2.6.2	FEATURES.....	15
2.7	APERTURE EFFICIENCY.....	15
2.8	ISOLATION.....	16
2.9	RELATIVE PERMITTIVITY.....	16
2.9.1	EFFECTIVE DIELECTRIC CONSTANT.....	17
2.10	LENS.....	18
2.11	3D PRINTING.....	18
2.12	GRADIENT INDEX LENSES.....	19
2.12.1	MAGNETIC INCLUSIONS.....	21
<b>3</b>	<b>SIMULATIONS.....</b>	<b>24</b>
3.1	MODELING THE TOROIDAL LENS.....	24
3.2	SYMMETRY PLANES.....	25
3.3	FEM SIMULATIONS.....	27
3.4	SIMULATION RESULTS.....	31
3.5	CHARACTERIZATION OF FIGURES OF MERIT.....	44
3.5.1	CHARACTERIZATION OF $\theta_{3\text{dB}}$ ON THE MAGNETIC PLANE.....	44
3.5.2	CHARACTERIZATION OF $\theta_{3\text{dB}}$ ON THE ELECTRIC PLANE.....	46



3.5.3 DIRECTIVITY CHARACTERIZATION .....	47
3.6 TOROIDAL LENS DESCRIBED IN TOROIDAL COORDINATES .....	49
<b>4 MATERIALS AND METHODS.....</b>	<b>52</b>
4.1 MATERIAL CHARACTERIZATION .....	52
4.1.1 DATA ACQUISITION .....	53
4.1.2 NRW RETRIEVAL METHOD .....	55
4.1.3 MODEL FITTING .....	57
4.1.4 ALTERNATIVE MATERIALS.....	58
4.2 UNIT CELL .....	59
4.2.1 MATERIAL DEPOSITION .....	63
4.2.2 PARABOLIC HOLES – A POTENTIALLY ALTERNATIVE METHOD .....	66
4.3 LENS PROTOTYPE .....	67
4.3.1 VALIDATION OF THE 3D-PRINTED STRUCTURE .....	68
4.3.2 LENS.....	69
4.4 ANTENNA .....	72
4.4.1 POTENTIAL ALTERNATIVES .....	74
4.5 TEST FIXTURE .....	74
4.6 TEST SETUP .....	78
<b>5 MEASUREMENTS .....</b>	<b>82</b>
<b>6 CONCLUSION.....</b>	<b>89</b>
6.1 FUTURE WORKS .....	89
<b>REFERENCES .....</b>	<b>90</b>
<b>A STUDY ON THE ANALYTICAL SOLUTION FOR THE TOROIDAL LENS....</b>	<b>96</b>
A.1 TOROIDAL COORDINATES.....	96
A.2 TOROIDAL WAVE FUNCTIONS .....	97
A.2.1 BASIS FUNCTIONS .....	97
A.2.1.1 CONVERGENCE .....	99
A.2.2 CHARGE-LESS MEDIUM .....	100
A.2.3 PARALLEL FUNCTIONS .....	101
A.2.4 CONTINUITY RELATIONS.....	101
A.2.5 INNER PRODUCTS .....	102
A.2.6 INNER PRODUCT MATRICES.....	103
A.3 MULTILAYER TORUS .....	104
A.4 CALCULATION OF COEFFICIENTS .....	106
<b>B DRAWINGS.....</b>	<b>108</b>

## LIST OF FIGURES

---

1.1	Electric field inside a Luneburg lens. The energy of an isotropic source is colimated into a plane wave at the oposite side. Source: reproduced from [1].	1
1.2	Differences from a static beam sector (left) to a beamforming system (right) applied to a mobile communication network. The static beam spread the energy on the fixed region, creating one spatial channel, on the other side the beamforming system focus the radiated power only on the useful directions, enhancing the efficiency of energy usage. Moreover it allows transmissions using the same frequency and time slot without interference. Source: reproduced from [2].	2
1.3	Cross section of a spherical lens, populated by antennas on the left-hand side. Trying to exceed the maximum antenna elements on the surface, by the red antennas for example, would create shadows, inhibiting their functionality.	3
1.4	Cross section of a torus-shaped lens. The antennas can now be placed towards multiple sectors the three-dimensional space, without shadow regions.	3
1.5	Lens constructed with slices of the same material, with the effective permittivity controlled by the drilling pattern. Source: reproduced from [3].	4
1.6	3D printed cylindrical lens with discrete layers. Source: reproduced from [4].	5
1.7	Spherical lens with parabolic hole pattern. This creates a continuous distribution of permittivity along the lens. Source: reproduced from [5].	6
1.8	Cross section of the spherical lens with parabolic holes. The parabolic profile is rotated around its own axis to create the hole. Source: reproduced from [5].	6
1.9	Single patch antenna conformed on a cylindrical surface. This type of antenna is an alternative for feeding the lens from inside the torus. It is necessary to adjust its shape to properly fit it to different elevation angles. Source: reproduced from [6].	7
1.10	Conformal patch antenna array. This type of array could be explored to achieve different radiation pattern. Source: reproduced from [7].	7
1.11	Slotted waveguide antenna. This type of feeding device can be mounted at the center of the torus, similarly to the solution proposed in [8]. Source: reproduced from [9].	8
1.12	Slotted waveguide antenna feeding a toroidal lens. Source: reproduced from [8].	8
2.1	Spherical coordinates system.	11
2.2	Types of waveguides. Source: Reproduced from [10].	12
2.3	Far-field and near-field regions. Source: Reproduced from [10].	13
2.4	Radiation pattern and its features. Source: Reproduced from [11].	15
2.5	Ray tracing of an oblique incidence on inhomogeneous medium. Source: reproduced from [10].	18
2.6	General idea of a gradient index lens. Source: Reproduced from [12].	19
2.7	Ray trajectory tracing for (a) Luneburg lens: $n(r) = \sqrt{2 - (r/R)^2}$ , (b) Eaton Lens: $n(r) = \sqrt{2R/r - 1}$ , and (c) Maxwell-Fisheye lens: $n(r) = 2n_0/(1+r^2/R^2)$ , where $n_0$ is the refractive index at the center of the lens. Source: Reproduced from [13].	20

2.8	Parameters of construction for the spherical lens. ....	20
2.9	$\epsilon_r$ distribution along the lens structure, according to Equations 2.21 and 2.22. The stratified lens is represented with 10 layers. ....	21
2.10	Simulation of the directivity on the electric (E) plane for the toroidal lens with inclusions of magnetic material with $\mu_r(r) = \epsilon_r(r)$ , $\forall r$ , comparing with the simulations of the lens with non-magnetic material. ....	22
2.11	Simulation of the directivity on the electric (E) plane for the toroidal lens with inclusions of magnetic material with $\mu_r(r) = \epsilon_r(r)$ , $\forall r$ , comparing with the simulations of the lens with non-magnetic material. ....	23
3.1	Geometry of the torus. $R_1$ is the minor radius, and $R_2$ is the major radius. $r$ is the variable that enables the analysis of the position inside and outside the solid. ....	24
3.2	Image theory. On a PEC plane, the tangential components of the electric field vanish due to compensations on the opposite directions, remaining only the perpendicular component. The same relation is valid for the PMC plane and the magnetic field. ....	26
3.3	Illustration of the E (electric) and H (magnetic) planes for the analyzed structure. ....	27
3.4	Model of the simulated toroidal lens. The excitation is done by an open waveguide antenna WR90 [14] positioned at the torus surface and pointed outwards, to the $\hat{y}$ direction. ....	28
3.5	Section view of the 10 layers toroidal lens. The thickness of the shells are uniform, with bounding radius according to Table 4.1. ....	29
3.6	Variation in antenna position along elevation angle. The path seen on the H-plane is not the same for all the angles. ....	30
3.7	Populated torus. This figure depicts the multi-channel setup, with multiple waveguides covering the space around the lens. ....	31
3.8	3D plot of directivity for the toroidal lens with concentric circles profile. ....	32
3.9	Total directivity on the E-plane for the toroidal, cylindrical, and spherical cases. ....	32
3.10	Total directivity on the H-plane for the toroidal, cylindrical, and spherical cases. ....	33
3.11	Comparison of directivity in E-plane for values of $R_1$ . The directivity increases for higher radius. ....	34
3.12	Comparison of directivity in E-plane for values of $R_2$ . The directivity increases for higher radius. ....	35
3.13	Comparison of directivity in H-plane for values of $R_1$ . The directivity increases for higher radius. ....	36
3.14	Comparison of directivity in H-plane for values of $R_2$ . The directivity increases for higher radius. ....	37
3.15	Description of the elevation angle. ....	38
3.16	Effects on directivity when the elevation angle of the antenna bore sight is changed. The variation in directivity does not cross 1.5% in relation to the $0^\circ$ elevation, but it is observed a pattern of decrease in directivity for angles close to $45^\circ$ , and an increase as the elevation angle approximates to $90^\circ$ . ....	38
3.17	Electric (E) plane of beams for WR90 positioned at different elevation angles. ....	39
3.18	Magnetic (H) plane of beams for WR90 positioned at different elevation angles. ....	39

3.19	Section view of the magnetic (H) plane for different elevation angles. The geometry seen by the optical path on the H plane varies due to the elevation angle of the antenna.	40
3.20	Map of the aperture efficiency for different parameter combinations, based on Equation 2.11.....	41
3.21	Map of the max directivity for different parameter combinations. ....	41
3.22	Map of the 3 dB aperture on E-plane for different parameter combinations. ....	42
3.23	Map of the 10 dB aperture on E-plane for different parameter combinations.....	42
3.24	Map of the 3 dB aperture on H-plane for different parameter combinations. ....	43
3.25	Map of the 10 dB aperture on H-plane for different parameter combinations. ....	43
3.26	Comparison between FEM simulation and model results for the half-power beam width in the magnetic plane.....	45
3.27	Maps of the FEM simulation and model results for the half-power beam width in the magnetic plane. ....	46
3.28	Comparison between FEM simulation and model results for the half-power beam width in the electric plane. ....	47
3.29	Maps of the FEM simulation and model results for the half-power beam width in the electric plane.....	47
3.30	Comparison between FEM simulation and model results for the total directivity. ....	48
3.31	Maps of the FEM simulation and model results for the half-power beam width in the electric plane.....	49
3.32	Cross section of the toroidal lens described in toroidal coordinates. Due to the coordinate system properties, the circular profiles that form the torus are not concentric. ....	49
3.33	3D plot of directivity for the toroidal lens described in toroidal coordinates. ....	50
3.34	Total directivity on the E-plane for the toroidal lenses with concentric circles and in toroidal coordinates. ....	50
3.35	Total directivity on the H-plane for the toroidal lenses with concentric circles and in toroidal coordinates.....	51
4.1	Sample block dimensions. The sample fits the WR90 TRL calibration kit in order to extract the dielectric constant of the material. For this work, it was used: $a = 22.90$ mm, $b = 10.11$ mm, and $L = 7.50$ mm. ....	52
4.2	TRL (Transmission-Reflection-Line) calibration and measurements. First, the Transmission data is captured by measuring the S-parameters of the two SMA-waveguide transitions connected to each other. Then, the measurement is done with the two transitions Open, and finally the transitions are connected with a $\lambda_0/4$ length line. Later, the material under test (MUT) is inserted in the line for the material measurement. When the data is computed, the reference plane of scattering parameters are shifted to the faces of the sample by applying the TRL calibration algorithm. Then it is possible to use the NRW algorithm to retrieve the dielectric constant of the material.	54

4.3	TRL waveguide calibration kit. It consists of two SMA-WR90 waveguide transistions (right) and a line element (left). The "Line" measurement is performed with the line element empty. The same line element is used to hold the sample being measured (MUT - material under test). In this picture, the MUT is the blue block inside the waveguide line on the left. ....	55
4.4	Some of the samples used for material characterization. The material is in natural color, in order to avoid influence of pigmentation differences to the analysis. ....	55
4.5	Electric field vectors of the TE <sub>10</sub> mode. Source: Reproduced from Orfanidis [10] .....	56
4.6	Effective dielectric constant modeling. Several samples were measured, varying its infill ratio to get the model for effective dielectric constant depending on this parameter. The MG model did not produce an accurate fit. The Lichtenecker's equation could have been used, but a better fit by the minimum mean square error was found for the Power Law, so that model was adopted. ....	58
4.7	Different styles of unit cell based on fixed length. With this strategy, the infill ratio is controlled by the size of the holes, which is limited by the minimum wall thickness and discretized by the nozzle diameter. ....	59
4.8	Rectangular unit cell parameters. The length of the unity cell is fixed, and the infill density is related to the hole size according to Equation 4.15. ....	60
4.9	Unit cells with discrete walls. The fixed cell size, combined with the limited nozzle diameter (0.25 mm) creates discrete values for the dielectric constant. ....	61
4.10	Woodpile structure. This is also called "grid" in 3D printing softwares. It consists of aligned and stacked rods. ....	62
4.11	Front view of the woodpile unit cell and its parameters. With this strategy the possible densities are continuous, because $L$ can assume any value above the diameter of the nozzle. ....	62
4.12	Woodpile unit cell lengths needed for the construction of the 10 layers of the lens, using the ABS with $\epsilon_r = 2.75$ . The larger cell size needed (2.45 mm) is smaller than $\lambda_0/10$ (3.00 mm), which represents a structure that will not cause considerable distortions to the wave. ....	63
4.13	Representation of the nozzle extruding the filament. The deposited material is flattened against the base to be properly merged with the previous layer (immediately below). This creates a trace slightly larger than the nozzle diameter, but that is further compensated by the pressure of the next trace on the immediate side, as presented in Figure 4.14. ....	64
4.14	Printed layers for a 100 % nominal infill ratio. The nozzle is not able to fill the whole volume of the rectangular profile. Indeed the printed profile is approximated by an ellipsoid. Therefore, the real density obtained is slightly lower than nominal because of the air filling the gaps between elliptic rods. ....	64
4.15	Microscopy of a 3D-printed sample. Source: Reproduced from Zhang's article [15]. It is possible to see the gaps between the traces and the flattening of the material, mentioned in Figure 4.13. ....	65

4.16	Infill differences for the woodpile printing pattern, using ABS. The density achieved for printed materials is 88.59% of the nominal density predicted. ....	65
4.17	Toroidal lens with continuous gradient of refractive index. ....	66
4.18	Cross section of the toroidal lens with parabolic profile cuts. The rotation of the profile around the central axis implies on suspended slabs that cannot be printed without a support. The FDM 3D printing with soluble material could be a solution to this problem [16]. ....	67
4.19	Printed slice of a five layer torus. It was used a support for angles higher than 40°. This was done as a validation of the manufacturing technique. ....	68
4.20	Slice of a stratified torus with 5 layers. It is possible to see that the layer separation was maintained, and the circular shape of the slice did not suffer distortion. Also, the variation of infill ratio can be verified by visual inspection of the sample against the light. ....	69
4.21	Printed lens. The lens have $R_1 = 35.5$ mm and $R_2 = 57.5$ mm. It was decided to print a half lens, considering only the 180° aperture for radiation. Since a directional antenna is being used. It is possible to see the grid pattern on the printing, with different infill ratio on the layers below. ....	71
4.22	Side view of the printed lens. The small stains and residual plastic attached to the lens does not affect the overall performance of the lens, as verified by the measurement results in Chapter 5. ....	71
4.23	WR90 open-ended waveguide antenna used to perform the far-field measurement experiments. The antenna has four tapered holes enable the assembly on the test fixture. In order to fit the antenna to the inner face of the torus, the front face of the waveguide was cut in a 25 mm radius. ....	72
4.24	Total directivity in the electric plane. There is a loss of 1 dB in the maximum directivity comparing to the standard waveguide. ....	73
4.25	Total directivity in the magnetic plane. There is a loss of 1 dB in the maximum directivity comparing to the standard waveguide. ....	73
4.26	WR90 open-ended waveguide antenna, fabricated in aluminium. ....	74
4.27	Perspective view of the lens fixed on the test fixture. The base is shaped to fit the surface of the lens. It is designed to be attached to the flange of the steering mechanism, represented by the brown part for reference. ....	75
4.28	Side view of the lens assembly. The base contains holes to fix the antenna with M3x8 screws, allowing the positioning of the antenna at the predefined tilt angles from 0° to 90° in steps of 10°. The male SMA connector is shown attached to the antenna to verify the space for the RF cable. ....	75
4.29	Front view of the lens assembly. ....	76
4.30	Perspective view from the back of the test fixture. The flange is the interface with the steering equipment. ....	76

4.31	Top view of the lens assembly. A 20 mm cylinder was attached to the lens structure in the same 3D printing process. The objective of this section of the part is to create a threaded interface for the six M5x25 plastic screws attaching the lens to the fixture. With this strategy, the 180° aperture is not affected by the auxiliary equipment. ....	77
4.32	Bottom view of the lens assembly. There is an oblong cut on the support to create a free path for the cable connection. ....	77
4.33	Steering equipment. It consists of a telescopic structure with 3 axis, already available on the Telecommunications Laboratory of the University of Brasilia. ....	78
4.34	Photography of the far-field measurement setup. ....	79
4.35	Measurement setup. The equipment set consists of two steering mechanisms. One with the antenna under test – connected to a spectrum analyzer –, and the other with the reference antenna – connected to a signal generator. The measurement process is controlled by a python script running on the <i>Synchronizing System</i> . ....	80
4.36	Human-Machine Interface (HMI) of the application designed for the test automation. It provides a control panel, with configuration fields and information about the test campaign. The back-end software triggers the functions on the main Python script to perform the measurements routine. ....	81
5.1	Illustration of the elevation angle (Elev) mentioned on the measurement results. The $\theta$ and $\phi$ angles, and the axis are the same from Figure 2.1. ....	82
5.2	Measurement of the radiation patter on the electric plane (E) for the lens + antenna set. "Elev" means the elevation angle in which the antenna is positioned. ....	83
5.3	Measurement of the radiation patter on the magnetic plane (H) for the lens + antenna set. "Elev" means the elevation angle in which the antenna is positioned. ....	84
5.1	Radiation pattern of the toroidal lens for the WR90 conformal antenna pointed at different elevation angles. ....	88
A.1	Toroidal Coordinate System. Source: [17] (Adapted).....	96

## LIST OF TABLES

---

3.1	$\epsilon_r$ distribution for the 10 layer torus. Layer 1 is the core, and layer 10 contains the external boundary. The radius comprehends the outer boundary of each layer, therefore the inner boundary for layer $n$ is the radius informed on layer $n - 1$ .....	27
3.2	Isolation results for two WR90 aligned in azimuth, for different elevation angles. ....	43
3.3	Isolation results for two WR90 aligned in elevation ( $0^\circ$ ), for different azimuth angles. .	43
3.4	Values found for the coefficients in Equation 3.3.....	45
3.5	Errors related to the samples of 3 dB beam width on the magnetic plane referent to the modeling function in Equation 3.3. ....	45
3.6	Values found for the coefficients of Equation 3.4.....	46
3.7	Errors related to the 3 dB beam width simulation in the electrical plane referring to the model function in Equation 3.4.....	46
3.8	Value found for the coefficients of Equation 3.5. ....	48
3.9	Errors related to the total directivity referring to the function in Equation 3.5. ....	48
4.1	$\epsilon_r$ distribution for 10 layer centered torus. Layer 1 is the core, and layer 10 contains the external boundary. ....	69
4.2	Parameters for the 3D printer used for manufacture the lens. ....	70



## LIST OF SYMBOLS

---

### Greek symbols

$\Gamma$	Reflection coefficient	
$\Omega$	Steradian	[sr]
$\chi$	Susceptibility	
$\epsilon_r$	Relative permittivity, dielectric constant	
$\epsilon$	Electric permittivity	[F/m]
$\eta_{ap}$	Aperture efficiency	
$\eta$	Intrinsic impedance of the medium	[ $\Omega$ ]
$\lambda$	Wavelength	[m]
$\mu_r$	Relative permeability	
$\mu$	Magnetic permeability	[H/m]
$\nabla$	Nabla operator	
$\omega$	Angular frequency	[rad/s]
$\phi$	Azimuth angle	[ $^\circ$ ]
$\theta$	Elevation angle	[ $^\circ$ ]

### Latin symbols

$A$	Area	[m <sup>2</sup> ]
$D$	Directivity	
$I$	Isolation	
$P$	Power intensity	[W]
$S$	S-parameter	
$T$	Transmission parameter	
$U$	Radiation intensity	[W/sr]
$\vec{B}$	Magnetic flux density	[T]
$\vec{D}$	Electric flux density	[C/m <sup>2</sup> ]
$\vec{E}$	Electric field	[V/m]
$\vec{H}$	Magnetic field	[A/m]
$\vec{J}$	Electric current density	[A/m <sup>2</sup> ]
$\vec{S}$	Poynting vector	[W/m <sup>2</sup> ]
$f$	Frequency	[Hz]
$n$	Refractive index	
$r$	Distance from origin	[m]

### Subscript symbols

$I$	Isotropic
$T$	Transverse
$eff$	Effective
$e$	Electric

$m$	Magnetic
$rad$	Radiated
$r$	Relative
$x, y, z$	Components $x, y, z$ of a vector

**Superscript symbols**

$\hat{\phantom{x}}$	Unit vector
$\rightarrow$	Vector notation
$*$	Complex conjugated

## LIST OF ACRONYMS AND ABBREVIATIONS

---

<b>3D</b>	Three-dimensional.
<b>ABS</b>	Acrylonitrile Butadiene Styrene.
<b>CSV</b>	Comma- Separated Values.
<b>EM</b>	Electromagnetic.
<b>FDM</b>	Fused Deposition Modeling.
<b>FEM</b>	Finit Element Method.
<b>HFSS</b>	High Frequency Simulation Software.
<b>HMI</b>	Human-Machine Interface.
<b>LHI</b>	Linear, Isotropic and Homogeneous.
<b>MAE</b>	Mean Absolute Error.
<b>MG</b>	Maxwell-Garnett.
<b>MIMO</b>	Multiple Input - Multiple Output.
<b>MSE</b>	Mean Squared Error.
<b>MUT</b>	Material Under Test.
<b>NRW</b>	Nicholson-Ross-Weir.
<b>PAA</b>	Phased Array Antenna.
<b>PEC</b>	Perfect Electrical Conductor.
<b>PETG</b>	Polyethylene Terephthalate + glycol.
<b>PLA</b>	Polylactic Acid.
<b>PMC</b>	Perfect Magnetic Conductor.
<b>PP</b>	Polypropylene.
<b>PVA</b>	Polyvinyl Alcohol.
<b>RF</b>	Radiofrequency.
<b>SLA</b>	Stereolithography Apparatus).
<b>SMA</b>	SubMiniature version A.
<b>TE</b>	Transverse Electric.
<b>TEM</b>	Transverse Electromagnetic.

- TM** Transverse Magnetic.
- TRL** Transmission-Reflection-Line.
- VNA** Vectorial Network Analyzer.
- WLAN** Wireless Local Network.

## NOTATION

---

$\approx$  Approximately.

**exp(x)** Exponential ( $e^x$ ).

# 1

## INTRODUCTION

The main objective of a lens is to collimate energy, transforming divergent energy into plane waves [11]. Lenses can be made of conductive material, such as Rotman Lenses, or dielectric, such as Fresnel and Luneburg Lenses, although the Luneburg lens can also be realized with conductive material, with employment of metasurfaces [18], [19]. Particularly, the Luneburg model [12] is a spherical lens with gradient refractive index along its profile. Figure 1.1 depicts the effect of the Luneburg lens on the electric fields of an isotropic source.

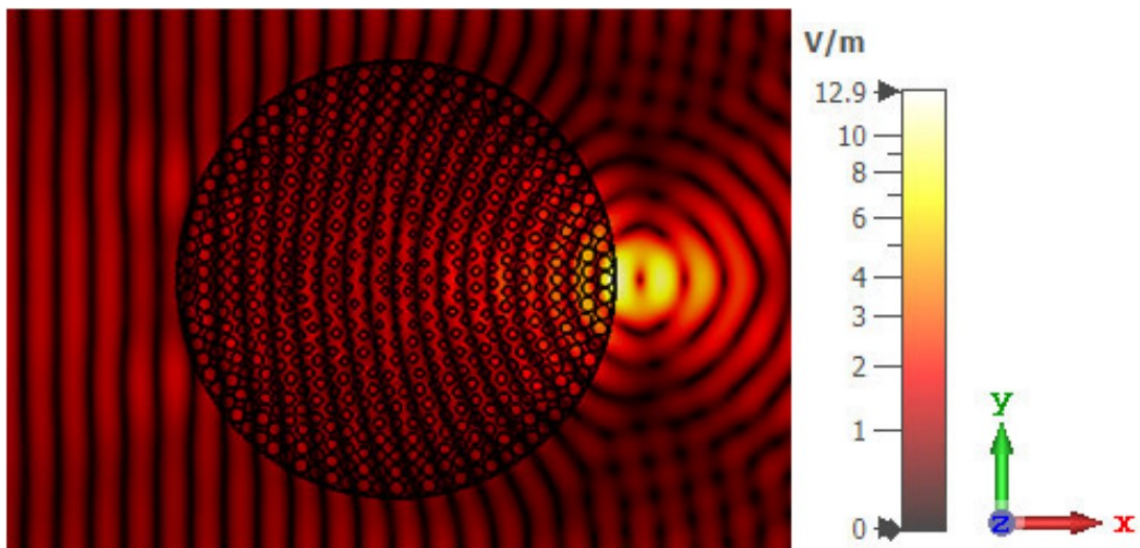


Figure 1.1 – Electric field inside a Luneburg lens. The energy of an isotropic source is colimated into a plane wave at the oposite side. Source: reproduced from [1].

### 1.1 APPLICATIONS

Luneburg lenses have commercial applicability in automotive radars [20], acting as a beamformer to focus the energy of the wave in the desired directions, achieving high scanning resolution.

According to Sahlli, [21], "Beamforming is a signal processing procedure used with multiple arrays of antennas at the transmitter side and/or receiver side to simultaneously send or detect multiple signals from multiple desired terminals to increase system capacity and performance".

Beamforming systems have been widely used in MIMO (Multiple Input - Multiple Output) applications. It increases spectral efficiency by allowing multiple transmissions using the same frequency and time slot without interference [2]. This is achieved using the radiation pattern features to focus the energy on specific directions, as depicted in Figure 1.2, creating a spatial channelization. Moreover, it optimizes the employed energy by avoiding power radiation on unwanted directions, *e.g.* unpopulated regions, in the case of mobile communication networks. The overall result is an increase in link throughput and user capacity, in comparison to static sector beams, depicted in the left of Figure 1.2.



Figure 1.2 – Differences from a static beam sector (left) to a beamforming system (right) applied to a mobile communication network. The static beam spread the energy on the fixed region, creating one spatial channel, on the other side the beamforming system focus the radiated power only on the useful directions, enhancing the efficiency of energy usage. Moreover it allows transmissions using the same frequency and time slot without interference. Source: reproduced from [2].

The lenses can also be used in totally passive devices, such as reflectors for RCS (Radar Cross Section) augmentation [22], enabling high radar visibility, which can be a solution for radar testing and calibration, support to military training activities, and can be used as highly reflective reference targets for air and marine navigation assistance. In the case of the reflector, the Eaton lens distribution could be used, because the rays would follow towards the source direction, as will be explained in Section 2.12. It is also possible to use a Luneburg lens with a metal foil on the opposite source side, acting as a reflector at the focal point, but this strategy would imply on a sectorization of the space covered by the reflector.

Gradient index lens are not only used for electromagnetic applications, but also for acoustic pressure beam focusing, such as in [23], [24], [25].

## 1.2 TOROIDAL LENS

One limitation of the spherical lens is that its antenna population limits the coverage of the space in some directions. Trying to exceed the maximum antenna elements on the surface would create shadow to other antennas, inhibiting their functionality, as depicted in Figure 1.3.

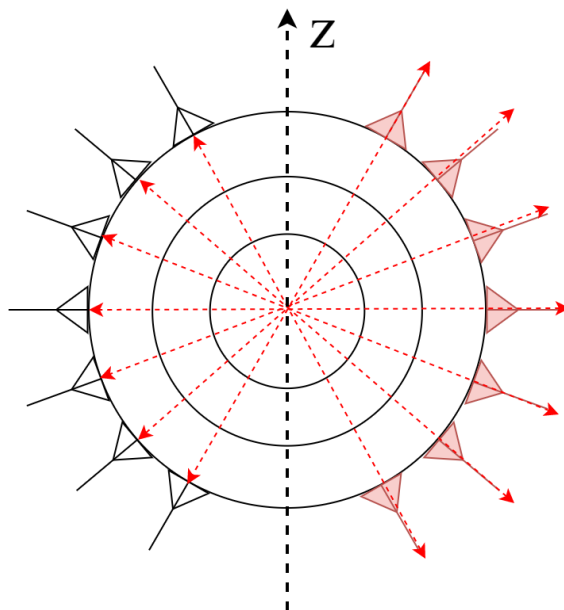


Figure 1.3 – Cross section of a spherical lens, populated by antennas on the left-hand side. Trying to exceed the maximum antenna elements on the surface, by the red antennas for example, would create shadows, inhibiting their functionality.

A torus-shaped lens could enable coverage of multiple sectors around the device, because directional antennas pointed to opposite sides would be positioned back-to-back along the torus surface, as in Figure 1.4. The antennas could also be replicated around  $z$  axis, as will be shown further in the perspective view of Figure 3.7.

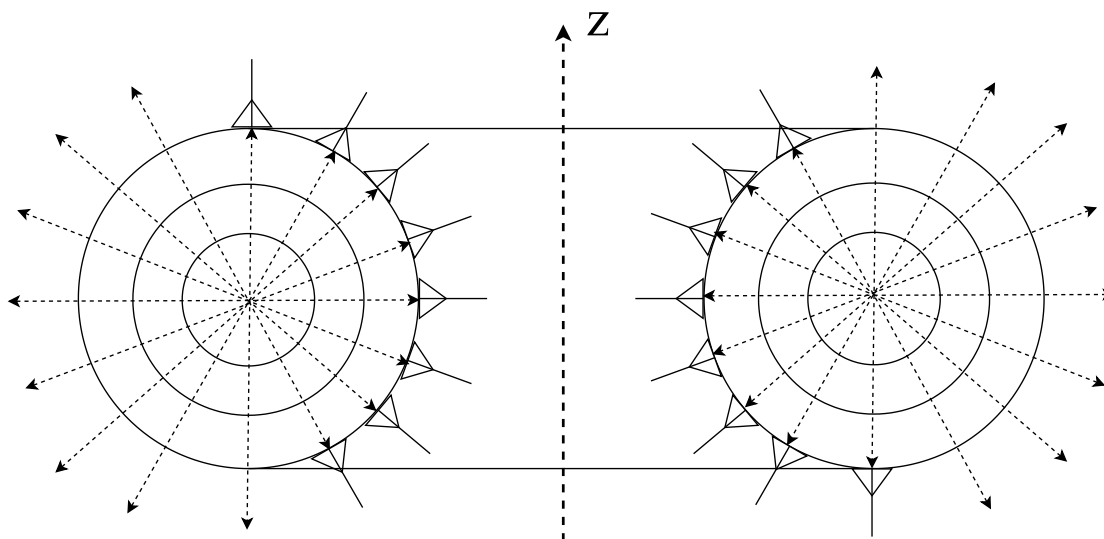


Figure 1.4 – Cross section of a torus-shaped lens. The antennas can now be placed towards multiple sectors the three-dimensional space, without shadow regions.

The extent of the covered space also applies to the Luneburg lens acting as a reflector, mentioned in Section 1.1. In that case, the antennas should be substituted by the metal foil.

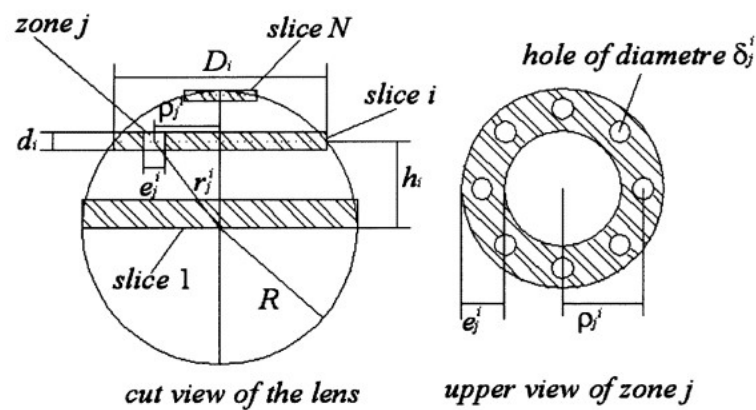


### 1.3 STATE OF THE ART

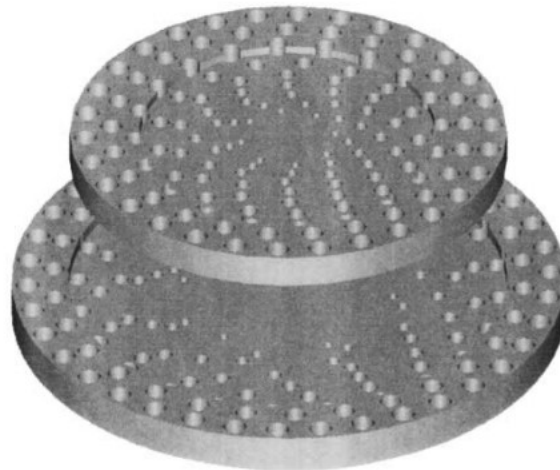
The main variation in literature for dielectric lenses is the method of fabrication. This includes the type of material, machining, and the strategy for achieving the necessary values of permittivity constant.

One of the methods is to use hemispherical shells of different materials and assembly them into a lens structure. But this implies on risks of air gaps between the shells [26]. Moreover, there is a difficulty on controlling different materials, ensuring that they accurately obey the required effective permittivity.

Some works use slices of the same material, with hole patterns creating a controlled effective permittivity based on the filling ratio, as shown in Figure 1.5 [3].



(a)



(b)

Figure 1.5 – Lens constructed with slices of the same material, with the effective permittivity controlled by the drilling pattern. Source: reproduced from [3].

The latest researches recur to additive methods, popularly known as "3D-printing", such as polymer jetting, used in [27] and FDM (Fused Deposition Modeling) used in [28]. This strategy follows the same principle of the infill ratio variation to achieve the necessary values of dielectric constant. The specific methods for doing that using FDM are addressed in Chapter 4.

Whichever the method, most works use discrete layers to accomplish the desired variation in dielectric constant, as shown in Figure 1.6.

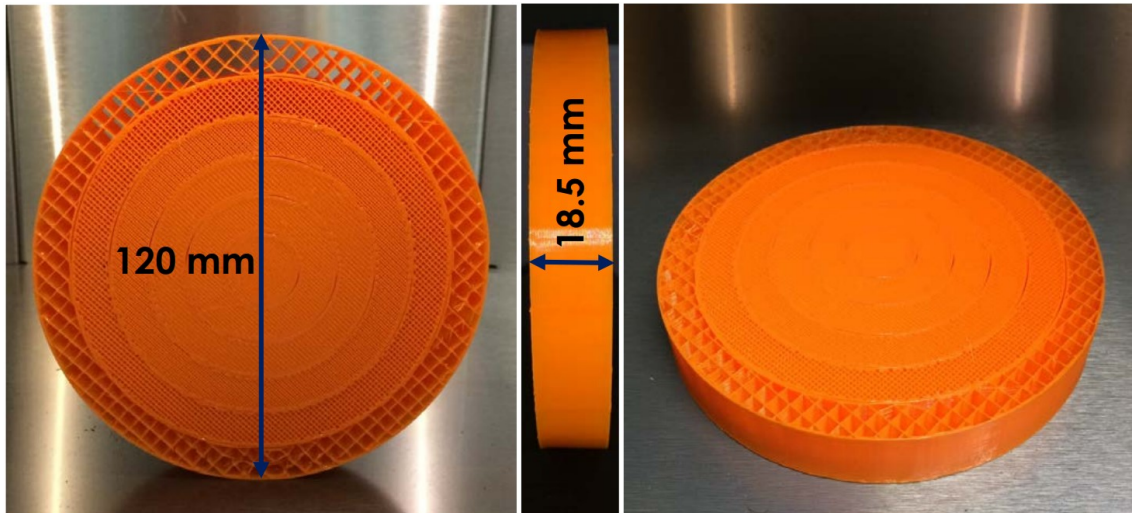


Figure 1.6 – 3D printed cylindrical lens with discrete layers. Source: reproduced from [4].

A variation of gradient index structures is the Eaton lens, which is described and tested in [29]. One interesting solution implemented by the author to fulfill the particularities of this type of lens – high range of effective dielectric constant, with abrupt increase of the value at the center – was to use a variable layer thickness.

For spherical lenses, it is proposed in [5] a hole pattern that implements Equation 2.21 continuously, using parabolic holes, as depicted in Figures 1.7 and 1.8.

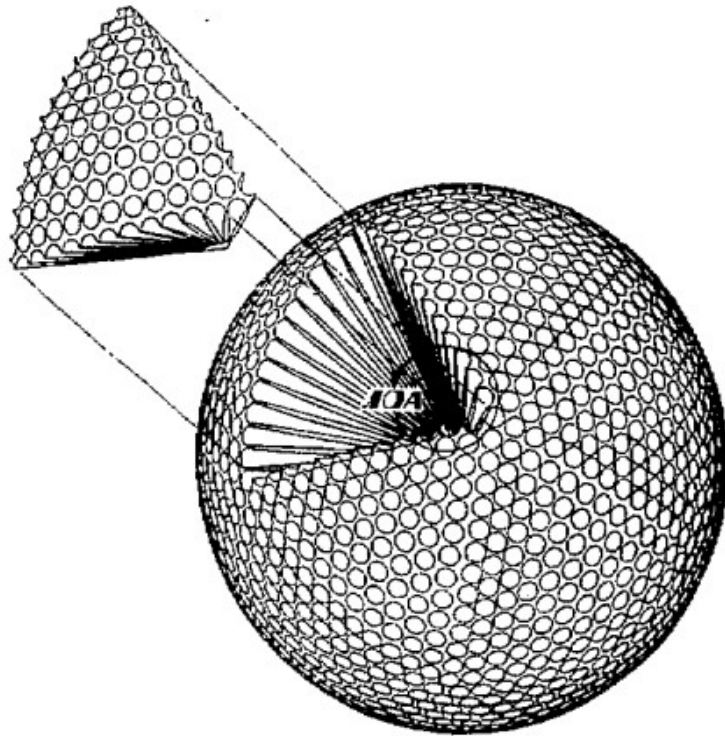


Figure 1.7 – Spherical lens with parabolic hole pattern. This creates a continuous distribution of permittivity along the lens. Source: reproduced from [5].

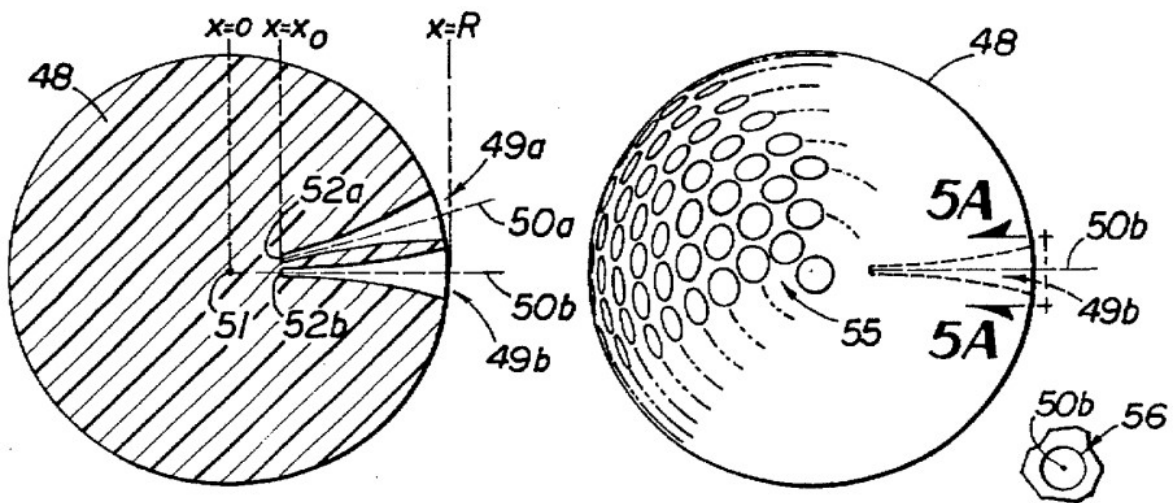


Figure 1.8 – Cross section of the spherical lens with parabolic holes. The parabolic profile is rotated around its own axis to create the hole. Source: reproduced from [5].

### 1.3.1 Conformal antennas

Since the focus of a Luneburg lens is on its surface, it is useful to have conformal antennas [30] on the system, in order to have the focused wave efficiently exciting the feeding device.

Single conformal patch antennas are used in [6], shown in Figure 1.9, and conformal patch arrays as in Figure 1.10 [7] can be explored to achieve different radiation patterns.

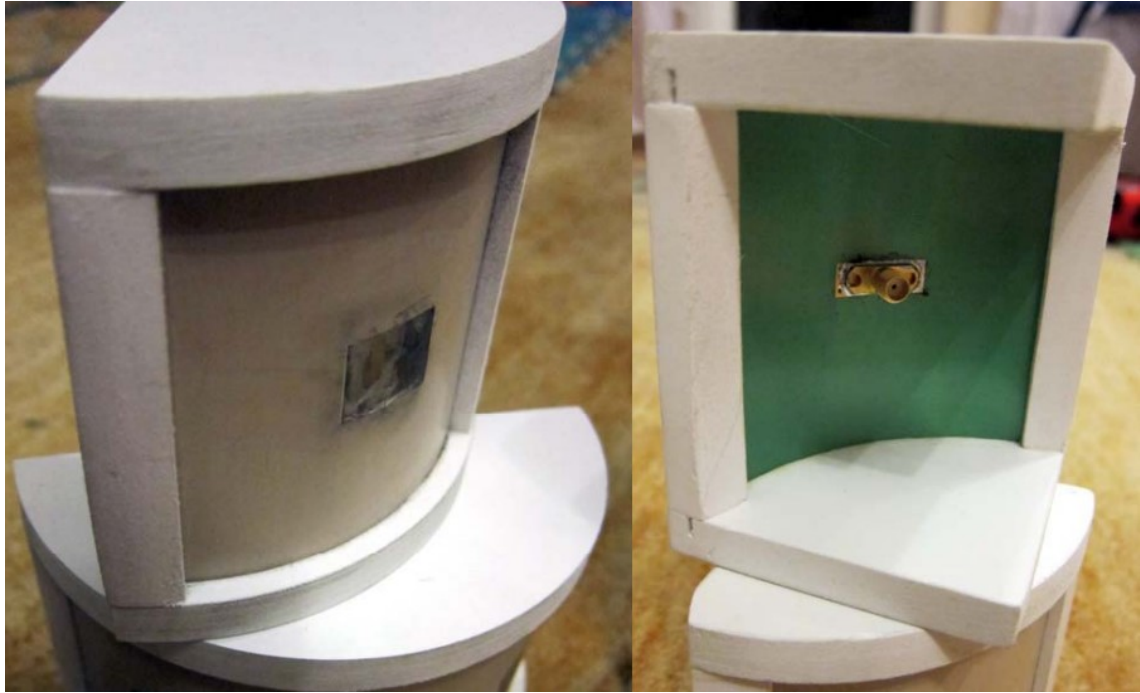


Figure 1.9 – Single patch antenna conformed on a cylindrical surface. This type of antenna is an alternative for feeding the lens from inside the torus. It is necessary to adjust its shape to properly fit it to different elevation angles. Source: reproduced from [6].

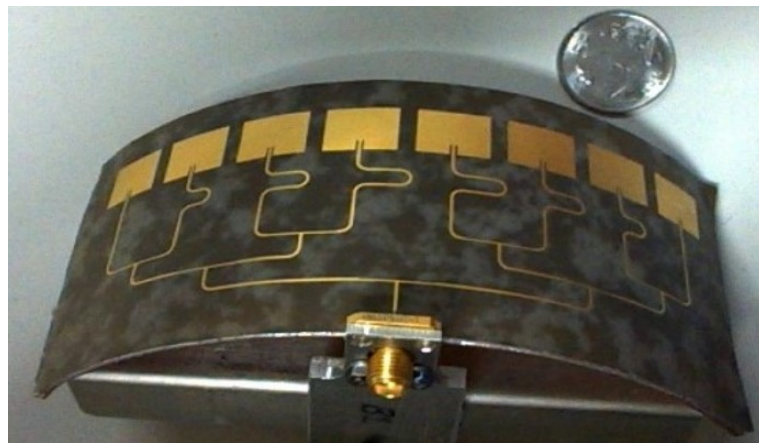


Figure 1.10 – Conformal patch antenna array. This type of array could be explored to achieve different radiation pattern. Source: reproduced from [7].

Slotted cylindrical waveguides can also be used, as shown in Figure 1.11, and a variation of this technique employs PIN diodes for selecting the beams, as proposed in [8], depicted in Figure 1.12.

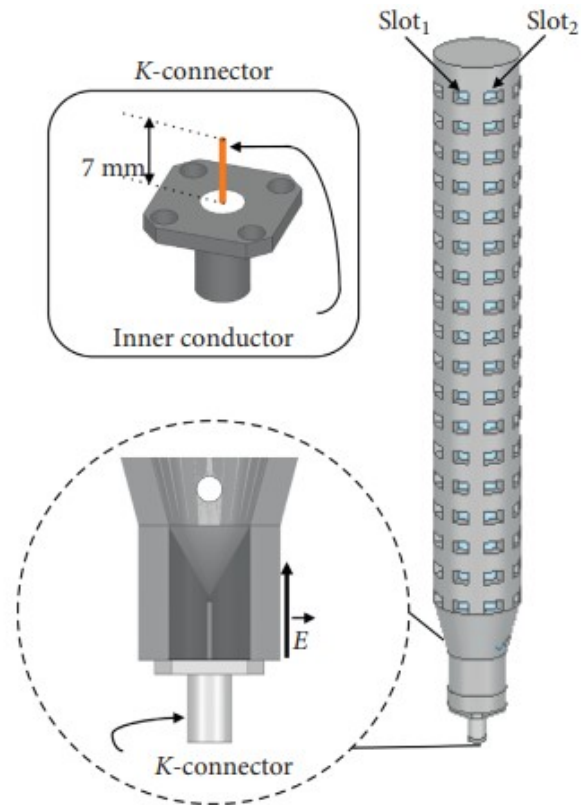


Figure 1.11 – Slotted waveguide antenna. This type of feeding device can be mounted at the center of the torus, similarly to the solution proposed in [8]. Source: reproduced from [9].

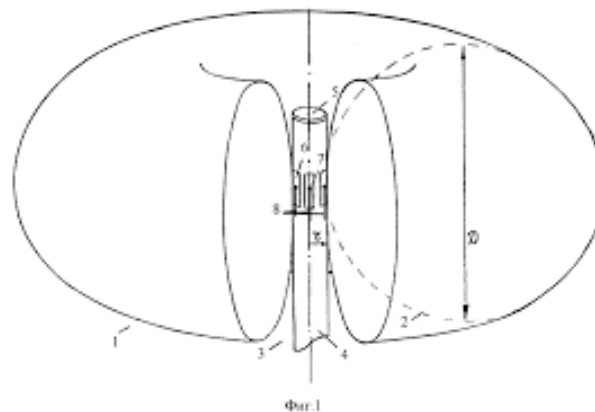


Figure 1.12 – Slotted waveguide antenna feeding a toroidal lens. Source: reproduced from [8].

### 1.3.2 Toroidal lens

A toroidal lens with homogeneous dielectric constant is proposed in [8]. The patent describes a dielectric lens with hemispherical profile, instead of circular. The feed structure is based on a cylindrical slotted waveguide radiator, with beam selection controlled by PIN diodes.

Maltsev presents in [31] and [32] a toroidal shaped lens also with homogeneous refractive index, but attached to a planar Phased Array Antenna (PAA). The same PAA strategy is used in [33] using a

toroidal Fresnel lens to scan in the azimuth plane.

The idea of a toroidal dielectric lens with gradient dielectric permittivity is described in [34]. The author proposes a technique for manufacturing the torus using multiple wedges cut from a cylinder with continuous gradient of refractive index. Its description is focused on the problem of the shadow regions explained in the previous section.

This work adds to the patent in [34] by providing quantitative results, obtained by simulation and measurement, and explaining the behavior on the horizontal plane (azimuth). Moreover, with the invention and popularization of the 3D printer, it became possible to manufacture the whole torus with the specified characteristics without the need to assembly multiple parts.

## **1.4 ANALYTICAL METHODS**

In order to reduce the computational effort and enable optimization of the lens geometry, it is desirable to have an analytical solution for the electromagnetic fields. This analysis can be done either by following the techniques using Green equations, as done in [26], or by using the reciprocity theorem, described in [35].

When employing either of the methods, the structure must be described by linear combinations of independent variables, which, in the case of the toroidal lens, can only be accomplished using toroidal coordinate system.

Another requirement is that the Helmholtz equation must be separable in the coordinate system used, which fails for the toroidal [36]. In bibliographic researches, it was found that Weston [37], [38], [39] was the only author to solve the Helmholtz equation separation problem for the toroidal coordinate system, with limitations for some special cases.

A partial work on the use of toroidal coordinates system to solve the problem of the stratified toroidal lens is presented in the Appendix A. Due to the novelty and high complexity level, besides the low quantity of references, this study could not be finished within the time disposed to the conclusion of the work presented on this document, but is attached as a proposal, incentive and baseline for future works.

## **1.5 OBJECTIVES**

### **1.5.1 Main Objectives**

1. To study the properties and of the toroidal dielectric lens.
2. To provide guidelines for designing a toroidal lens.

## 1.5.2 Specific Objectives

1. To review the spherical Luneburg lens and methods of fabrication.
2. To propose a toroidal lens based on Luneburg distribution of refractive index.
3. To characterize the material and explore the possible techniques for manufacturing the toroidal lens.
4. To map the performance of the toroidal lens in terms of its electrical dimensions and position of the antenna.
5. To develop a test setup to perform the measurement of the lens.
6. To study the antenna characteristics, and the behavior of the system *antenna+lens* in MIMO applications.
7. To propose an analytical solution for the electromagnetic fields on the toroidal lens.

## 1.6 ORGANIZATION OF THE DISSERTATION

This work is organized in 6 chapters:

This chapter presented an overview about lenses and its applications, also presenting the idea of the novel device, state of the art, and objectives of the dissertation

Chapter 2 presents the fundamental concepts, essential to the comprehension of the technical terms mentioned in this work.

Chapter 3 shows the simulations and results of the lens performance, in terms of directivity, beam width, aperture efficiency, and isolation.

Chapter 4 presents the characterization of the material, with the theory of *effective dielectric*. It also discusses the methods for fabrication of the lens, using 3D printing, including considerations about imperfections and practical limitations. Moreover, it presents the test setup for radiation pattern measurements.

Chapter 5 presents the measurement results of radiation pattern, comparing with the FEM (Finite Element Method) simulations.

Chapter 6 concludes the work with a general outline and presents the suggestion of future works.

Appendix A is also important to this dissertation. It contains the theory concerning the analytical solution of the fields of the toroidal lens in toroidal coordinates. But since this part could not be finished within the time disposed to the completion of this work, it was included in the appendices.

Appendix B presents the assembly drawing of the antenna used on the measurement setup, previously mentioned in Chapter 4.

# 2 DEFINITIONS

---

This chapter introduces the definitions of technical names, expressions and parameters mentioned in this work, essential for the comprehension of the text.

## 2.1 COORDINATE SYSTEM

The results of this work are plotted in spherical coordinates, with parameters depicted in Figure 2.1.

When referring to *Elevation* angle, it is meant the angle  $\theta$ , and *Azimuth* refers to  $\phi$ .

Unless specified, the results are presented with the antenna pointed (*i.e.* with the direction of maximum directivity) to the  $\hat{z}$  direction.

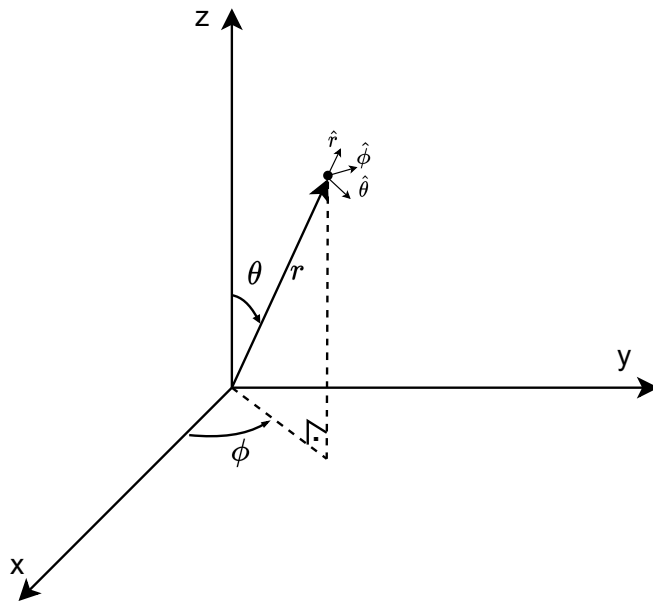


Figure 2.1 – Spherical coordinates system.

## 2.2 TRANSVERSE MODES

The analysis of transverse modes uses the transverse electric and magnetic fields:  $\vec{E}_T$  and  $\vec{H}_T$ . Those vectors are perpendicular to each other in a similar manner of a plane wave propagating in the  $\hat{z}$  direction [10]. Thus, they satisfy the Equation:



$$\vec{H}_T = \frac{1}{\eta} \hat{z} \times \vec{E}_T, \quad (2.1)$$

where  $\eta$  is the intrinsic impedance of the medium impedance. The TEM mode (Transverse Electromagnetic) is characterized by

$$E_z = H_z = 0,$$

with both modes perpendicular to  $\hat{z}$ .

The TE mode (Transverse Electric) appears when

$$E_z = 0, H_z \neq 0$$

Finally, the TM mode (Transverse Magnetic) have

$$E_z \neq 0, H_z = 0$$

## 2.3 WAVEGUIDE

A waveguide is a structure used to transfer electromagnetic power between two points of a circuit [10]. Figure 2.2 presents some types of waveguides.

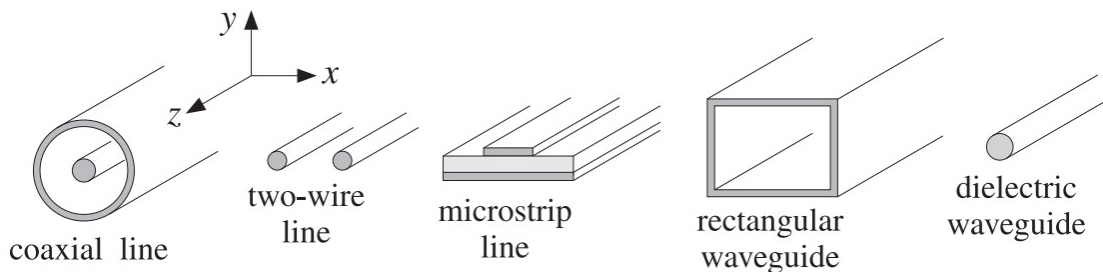


Figure 2.2 – Types of waveguides. Source: Reproduced from [10].

The type of waveguide seen in a circuit depends on the application, operating frequency, costs, etc. For example, the two-wire line has been largely used in telephone signal lines, microstrip lines are suitable for printed circuit boards, while rectangular waveguides are more adequate for high power and precision systems [40].

## 2.4 ANTENNA

According to Balanis: "the antenna is the transitional structure between free-space and a guiding device" [11]. Therefore, an antenna is used on RF systems whenever it is desirable to radiate an electromagnetic signal from a circuit to the space around (transmission), or to use the signals radiated

from other sources into an electronic circuit (reception).

### 2.4.1 Aperture antenna

Simply put, an aperture antenna is a type of antenna with an aperture at its end.

The field radiated by the an aperture antenna is determined by the fields over the aperture, which follows the Huygens' principle, explained by Orfanidis with the words: "the points on each wavefront become the sources of secondary spherical waves propagating outwards and whose superposition generates the next wavefront" [10].

The *open-ended waveguide antenna* is a sub-type of aperture antenna. In this type of antenna, the aperture is the waveguide cross section profile itself.

## 2.5 FAR-FIELD

The field analysis used in this work is based on the far-field approximations. Far-field, also known as *Fraunhofer region* is the region located very far from the current sources, at least  $2l^2/\lambda$ , where  $l$  is the maximum dimension of the antenna, as depicted in Figure 2.3.

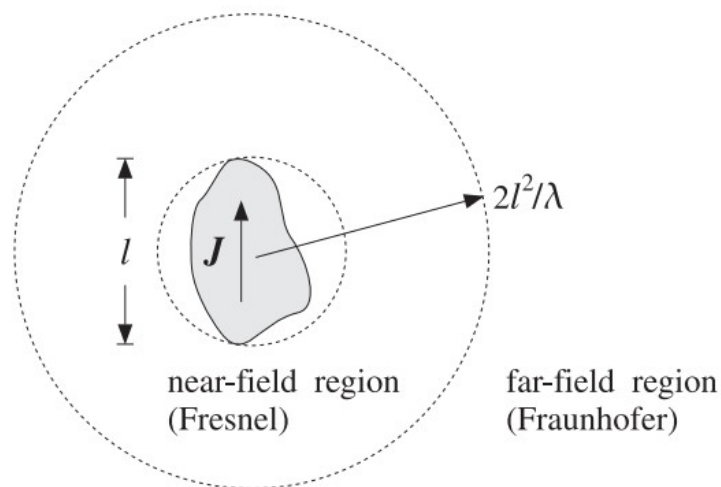


Figure 2.3 – Far-field and near-field regions. Source: Reproduced from [10].

The special feature about the far-field region is that the angular field distribution is independent from the distance to the current source (antenna), and the field components are essentially transverse [11].

## 2.6 RADIATION PATTERN

The *radiation pattern* is the angular distribution of the radiated energy [10]. It is useful for analyzing some figures-of-merit of the radiating element/system.

### 2.6.1 Directivity

Considering an harmonic regime, *i.e.*

$$\omega = 2\pi f,$$

where  $\omega$  is the angular frequency, and  $f$  is the frequency in Hz, the energy flux radiated on the far-field from the current  $\vec{J}$  (from Figure 2.3) is calculated by the time average of the Poynting vector:

$$\vec{S} = \frac{1}{2}\text{Re}(\vec{E} \times \vec{H}^*), \quad (2.2)$$

which flows radially away from the current source [10], meaning that:

$$\vec{S} = \hat{r} S_r \quad (2.3)$$

Next, defining the radiation intensity  $U(\theta, \phi)$  as the power radiated per unit solid angle:

$$U(\theta, \phi) = \frac{dS}{d\Omega} = r^2 S_r \quad (2.4)$$

Given so, we can define the total radiated power as an integration of the power intensity over all the angles.

$$P_{rad} = \int_0^{2\pi} \int_0^\pi U(\theta, \phi) d\Omega, \quad (2.5)$$

where  $d\Omega = \sin \theta d\theta d\phi$

Then, the isotropic radiation intensity  $U_I$  is defined as the total radiated power equally distributed in all directions of a rounding sphere:

$$U_I = \frac{P_{rad}}{4\pi} \quad (2.6)$$

Finally, the *directivity*  $D(\theta, \phi)$  is defined as the radiation intensity normalized by the corresponding isotropic radiation intensity:

$$D(\theta, \phi) = \frac{U(\theta, \phi)}{U_I} \quad (2.7)$$

The directivity is the response to the question "how much more power an antenna radiates towards

a given direction in comparison to its equivalent if it was an isotropic antenna". In other words, it measures the focusing capabilities of the antenna.

### 2.6.2 Features

Figure 2.4 presents the 3D representation of a generic radiation pattern. The major lobe is also called "main lobe", it contains the maximum antenna directivity. Side lobes are all the lobes lower than the main one [11].

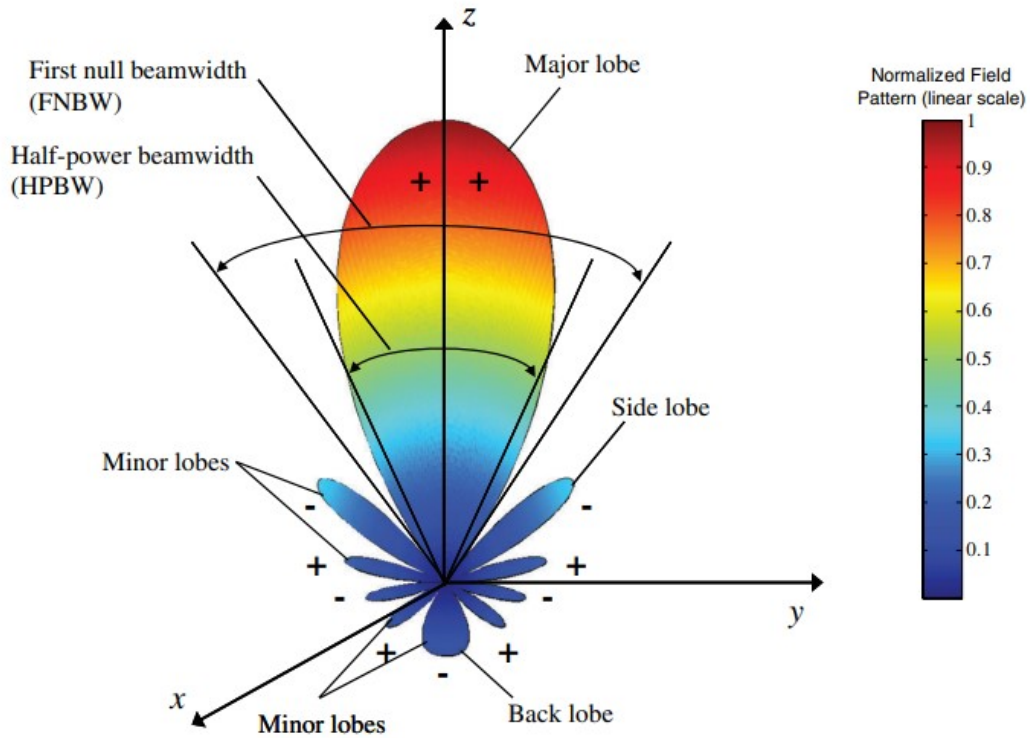


Figure 2.4 – Radiation pattern and its features. Source: Reproduced from [11].

## 2.7 APERTURE EFFICIENCY

Apertures have an efficiency factor, relating its physical area ( $A$ ) and the effective area through which flows the radiated power.

Balanis [11] defines the effective area as "the ratio of the available power at the terminals of a receiving antenna to the power flux density of a plane wave incident on the antenna from that direction, the wave being polarization-matched to the antenna".

The maximum directivity is related to the effective area of the aperture  $A_{eff}$  by [10]:

$$D_{max} = \frac{U_{max}}{U_I} = 4\pi \frac{U_{max}}{P_{rad}} = \frac{4\pi A_{eff}}{\lambda^2}, \quad (2.8)$$

where  $A_{eff} \leq A$ .

Then, the aperture efficiency  $\eta_{ap}$  is given by:

$$\eta_{ap} = \frac{A_{eff}}{A} \leq 1 \quad (2.9)$$

Alternatively, it is convenient to extract the aperture efficiency by estimating the ideal directivity  $D_0$  from the half power width ( $\theta_{3dB}$  and  $\phi_{3dB}$ ) [11], using Equation 2.10. But this approximation is only valid if the radiation pattern has only one major lobe, with side lobes with negligible intensity.

$$D_0 \simeq \frac{41253}{\theta_{3dB}\phi_{3dB}} \quad (2.10)$$

Then

$$\eta_{ap} = \frac{D_{max}}{D_0}, \quad (2.11)$$

where  $D_{max}$  is the maximum directivity of the antenna [41].

## 2.8 ISOLATION

The isolation is mentioned in this work as the parameter of transmission between two antennas of the same equipment. It is also known as mutual coupling. In other words, it is the ratio between the power received by one antenna to the power transmitted by the reference antenna.

It is used to characterize multi-channel systems (with more than one antenna). A good isolation is essential to the performance of this type of equipment, in order to avoid cross talk or interference.

The expression for the isolation is given by:

$$I_{ab} = \frac{P_a}{P_b}, \quad (2.12)$$

where  $P_a$  is the power received at the port of antenna  $a$  and  $P_b$  is the transmitted power at the input port of antenna  $b$ , given that the antenna  $b$  is the one being excited.

## 2.9 RELATIVE PERMITTIVITY

Considering a Linear, Homogeneous and Isotropic medium (LHI), the permittivity  $\epsilon$  of the medium is a constitutive relation of the electric flux density  $\vec{D}$  and the electric field  $\vec{E}$ :

$$\vec{D} = \epsilon \vec{E} \quad (2.13)$$

The *relative permittivity*  $\epsilon_r$ , also known as *dielectric constant*, of a given medium is the relation between the permittivity of the medium and the vacuum ( $\epsilon_0 = 8.854 \times 10^{-12}$  F/m). It is related to the electric susceptibility  $\chi_e$ , which measures the electric polarization properties of the material. [10].

$$\epsilon_r = \frac{\epsilon}{\epsilon_0} = 1 + \chi_e \quad (2.14)$$

Similarly, with the same LHI medium assumption, the permeability  $\mu$  relates the magnetic flux density  $\vec{B}$  and the magnetic field  $\vec{H}$  as:

$$\vec{B} = \mu \vec{H} \quad (2.15)$$

Which may be expressed as relative permeability  $\mu_r$ , relating to the vacuum permeability ( $\mu_0 = 4\pi \times 10^{-7}$  H/m), and is associated to the magnetic susceptibility  $\chi_m$  as well:

$$\mu_r = \frac{\mu}{\mu_0} = 1 + \chi_m \quad (2.16)$$

Both constitutive relations are used to define the refractive index  $n$  of the material:

$$n = \sqrt{\mu_r \epsilon_r} \quad (2.17)$$

**For non-magnetic materials**, which is the case from now on:

$$\mu = \mu_0 \text{ then, } \mu_r = 1,$$

yielding:

$$n = \sqrt{\epsilon_r}$$

### 2.9.1 Effective dielectric constant

The dielectric constant of an heterogeneous material is evaluated by the proportion between the constituent materials [42]. Microstrip lines, for example, creates an EM field through the dielectric and the air, so the *effective dielectric constant* is a relation between the relative permittivity of both mediums [40].

Therefore, the effective dielectric constant can be controlled using the correct proportions on a mixture of dielectric material and air, *i.e.* adjusting the density of the sample. There are many models describing the effective permittivity for dielectric mixtures. Those will be presented with more details on Section 4.1.3

## 2.10 LENS

According to Balanis, "lenses are primarily used to collimate incident divergent energy to prevent it from spreading in undesired directions" [11].

The functioning of a lens is based on the Fermat's principle, that states that "among all possible paths connecting the two points A and B, the geometrical optics ray path is the one that minimizes the optical path length" [10]. The optical path length is given by:

$$S_B - S_A = \int_A^B n \, dl \quad (2.18)$$

and the solution of the minimization is given by the *Ray equation*:

$$\frac{d}{dl} \left( n \frac{dr}{dl} \right) = \nabla n \quad (2.19)$$

From the ray equation it is derived the famous Snell Law, which is generalized by Equation 2.20 for the case of the ray crossing two media, depicted in Figure 2.5.

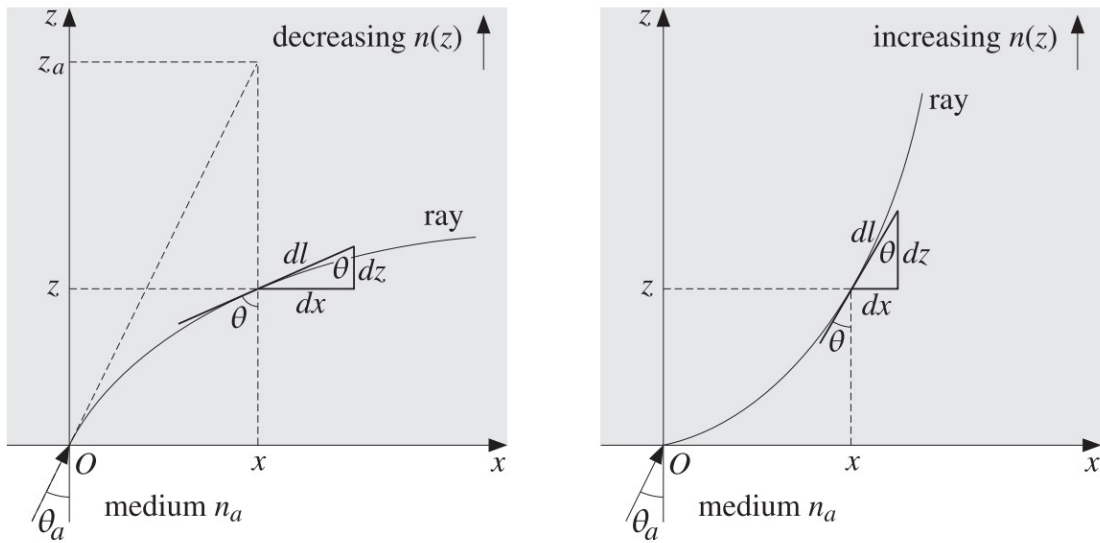


Figure 2.5 – Ray tracing of an oblique incidence on inhomogeneous medium. Source: reproduced from [10].

$$n(z) \sin \theta(z) = n_a \sin \theta_a \quad (2.20)$$

## 2.11 3D PRINTING

3D printing is an additive manufacturing technique, meaning that it deposits material to construct the part. Among the several methods, one of the most common and accessible is the FDM (Fused De-

position Modeling), which fuses a filament layer by layer. The filaments are generally polymers, like ABS (Acrylonitrile Butadiene Styrene), PLA (Polylactic Acid), PETG (Polyethylene Terephthalate + glycol), and PVA (Polyvinyl Alcohol).

Another method is the SLA (Stereolithography Apparatus), that uses laser to solidify photosensitive materials [43].

## 2.12 GRADIENT INDEX LENSES

The general idea of a GRIN (Gradient Index) lens is presented in Figure 2.6, proposed by Luneburg in [12]. Applying the ray equation, the rays can follow a curved trajectory through an inhomogeneous medium.

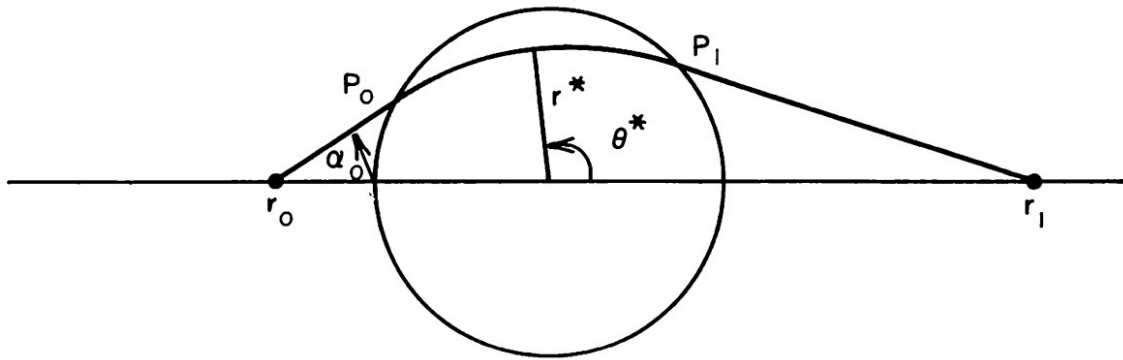


Figure 2.6 – General idea of a gradient index lens. Source: Reproduced from [12].

There exists more than one type of non-homogeneous spherical lens. Different distributions of refractive index along the lens result in different ray tracing trajectory, as depicted in Figure 2.7.



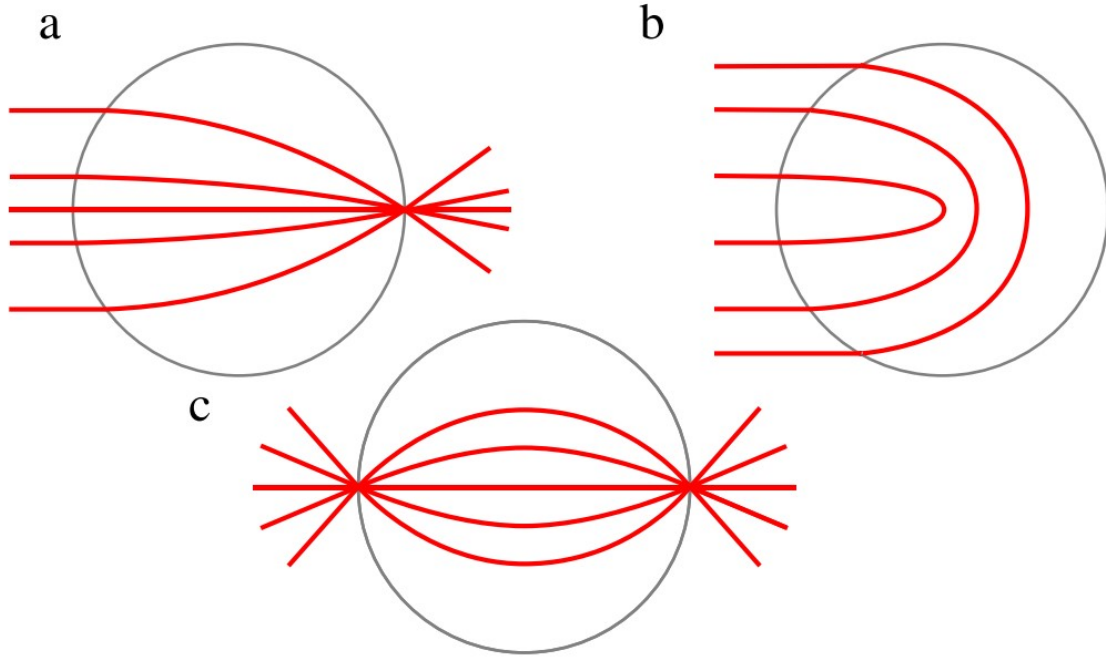


Figure 2.7 – Ray trajectory tracing for (a) Luneburg lens:  $n(r) = \sqrt{2 - (r/R)^2}$ , (b) Eaton Lens:  $n(r) = \sqrt{2R/r} - 1$ , and (c) Maxwell-Fisheye lens:  $n(r) = 2n_0/(1 + r^2/R^2)$ , where  $n_0$  is the refractive index at the center of the lens. Source: Reproduced from [13].

A typical Luneburg lens is a spherical structure with gradient distribution of refractive index described by the expression in Equation 2.21 [12]. Figure 2.8 presents the construction variables of the lens. The outside medium is the air, with  $\epsilon_r = 1$

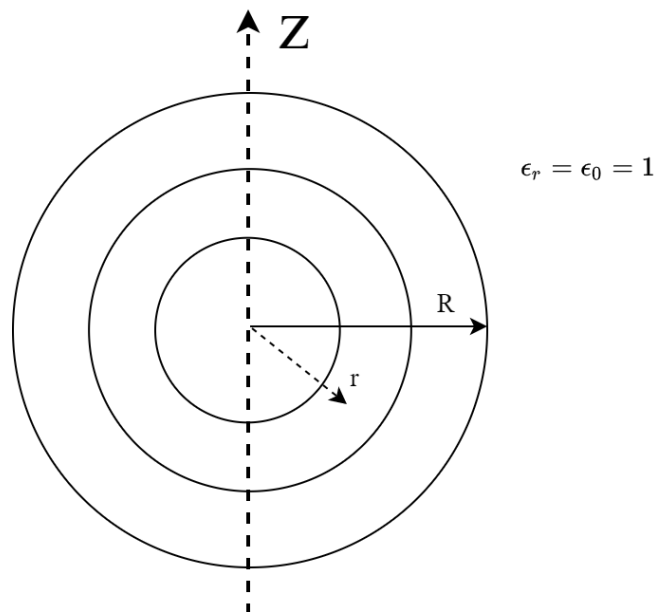


Figure 2.8 – Parameters of construction for the spherical lens.

$$n(r) = \sqrt{\epsilon_r(r)} = \sqrt{2 - \left(\frac{r}{R}\right)^2} \quad (2.21)$$

In Equation 2.21 it is considered a non-magnetic material;  $r$  is the radial position of the observer, and  $R$  is the sphere total radius.

The Luneburg lens is used to focus the energy of an incoming plane wave on a single point at the opposite side of its surface (in terms of signal reception) or to focus radiation pattern of an antenna (placed on the surface of the lens) on narrow directions (in terms of signal transmission), *i.e.* it is a reciprocal device.

A practical Luneburg lens can be constructed with discrete shells of different refractive indices [26], respecting the relations in equation 2.21, thus having a stratified medium. In this case, the values of relative permittivity for each discrete layer can be found by Equation 2.22.

$$\epsilon_r(p) = 2 - \left(\frac{2p-1}{2N}\right)^2, \quad p = 1, 2, \dots, N \quad (2.22)$$

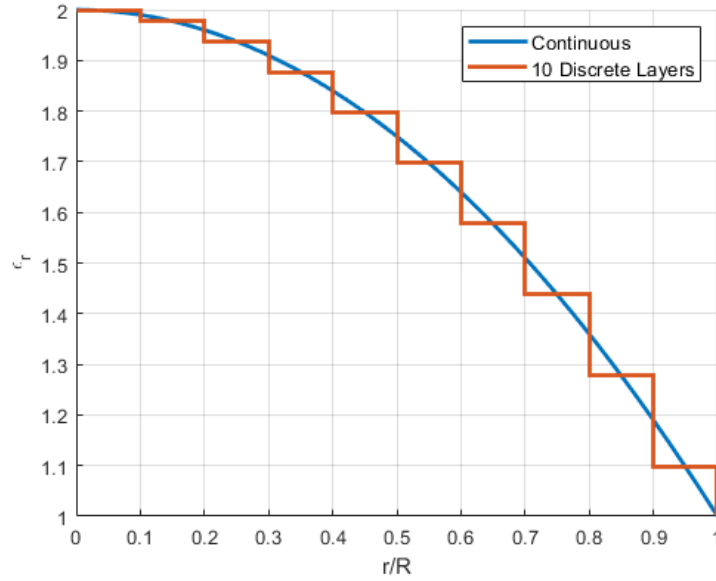


Figure 2.9 –  $\epsilon_r$  distribution along the lens structure, according to Equations 2.21 and 2.22. The stratified lens is represented with 10 layers.

A typical variation is the *cylindrical Luneburg lens* [44]. It follows the same distribution of Equation 2.21, but with the structure in Figure 2.8 representing the cross section of a cylinder, instead of a sphere.

### 2.12.1 Magnetic inclusions

Besides the variation of the electric permittivity, the relative magnetic permeability  $\mu_r$  could be controlled, using yttrium for example. And by making it equal to  $\epsilon_r$  for all the layers, the impedance

of the medium is always equal to the intrinsic impedance of the air, according to Equations 2.23 and 2.24.

$$\eta(r) = \eta_0 \sqrt{\frac{\mu_r(r)}{\epsilon_r(r)}} \quad (2.23)$$

$$\mu_r(r) = \epsilon_r(r) \Rightarrow \forall r \eta(r) = \eta_0, \text{ and } n(r) = \epsilon_r(r) \quad (2.24)$$

This creates an impedance matching between the lens structure and the medium, resulting on the elimination of reflections of the wave, increasing directivity and reducing side-lobe level.

Furthermore, as seen in Equation 2.24, the refraction index becomes equal to the electric permittivity. Applying this to Equation 2.21, the core of the lens is managed to have dielectric constant equal to  $\sqrt{2}$ , which implies a lower density of dielectric material, consequently reducing the weight of the overall structure. Figures 2.10 and 2.11 show the directivity plots from simulations of such lens.

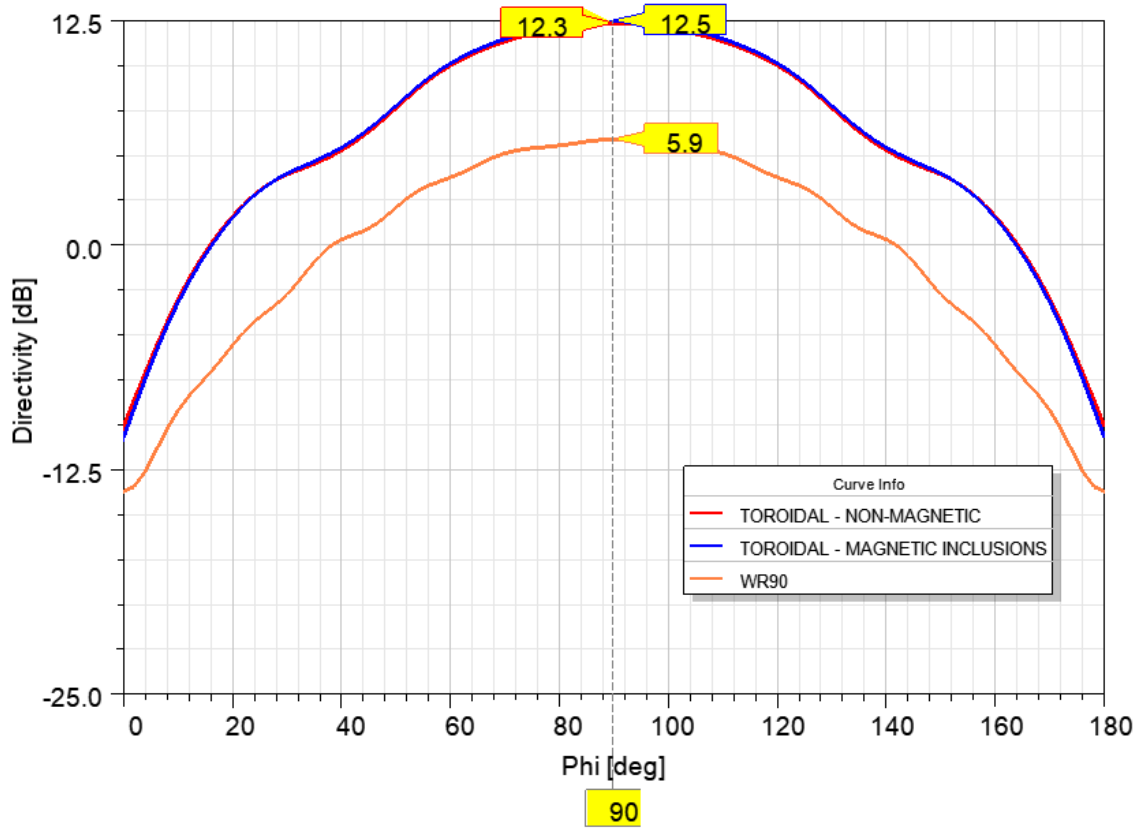


Figure 2.10 – Simulation of the directivity on the electric (E) plane for the toroidal lens with inclusions of magnetic material with  $\mu_r(r) = \epsilon_r(r)$ ,  $\forall r$ , comparing with the simulations of the lens with non-magnetic material.

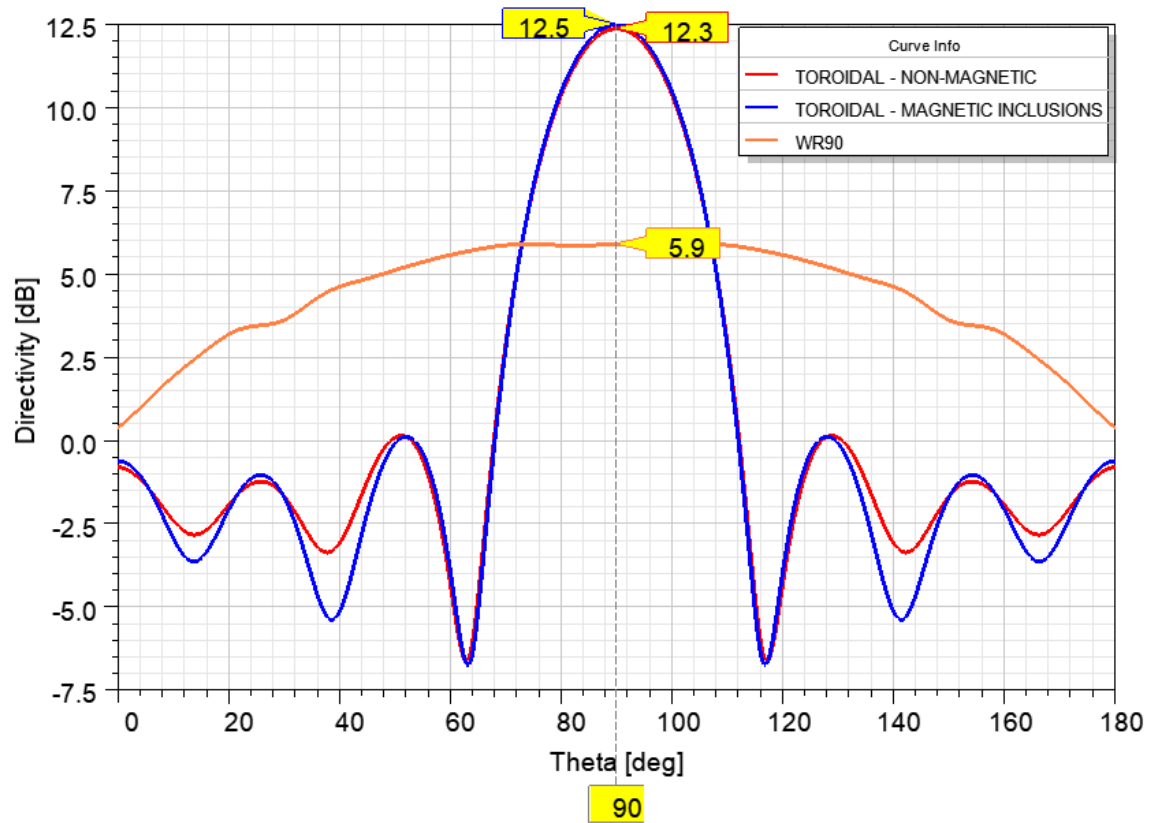


Figure 2.11 – Simulation of the directivity on the electric (E) plane for the toroidal lens with inclusions of magnetic material with  $\mu_r(r) = \epsilon_r(r), \forall r$ , comparing with the simulations of the lens with non-magnetic material.

# 3 SIMULATIONS

This chapter presents the parametrization of the lens, and its modeling into the full-wave simulation software ANSYS Electronics - HFSS (High Frequency Simulation Software) [45].

## 3.1 MODELING THE TOROIDAL LENS

The torus is modeled with two variables:  $R_1$ , the minor radius, and  $R_2$ , the major radius, depicted in Figure 3.1. The circle described by the radius  $R_1$  and extruded around the  $z$  axis resembles the rotation of a circle forming a sphere (in that case  $R_2$  would be zero). This approach enables the use of the toroidal shape to emulate the sphere geometry through the vertical cross section plane. The toroidal lens can also be interpreted as a "bent" cylindrical lens.

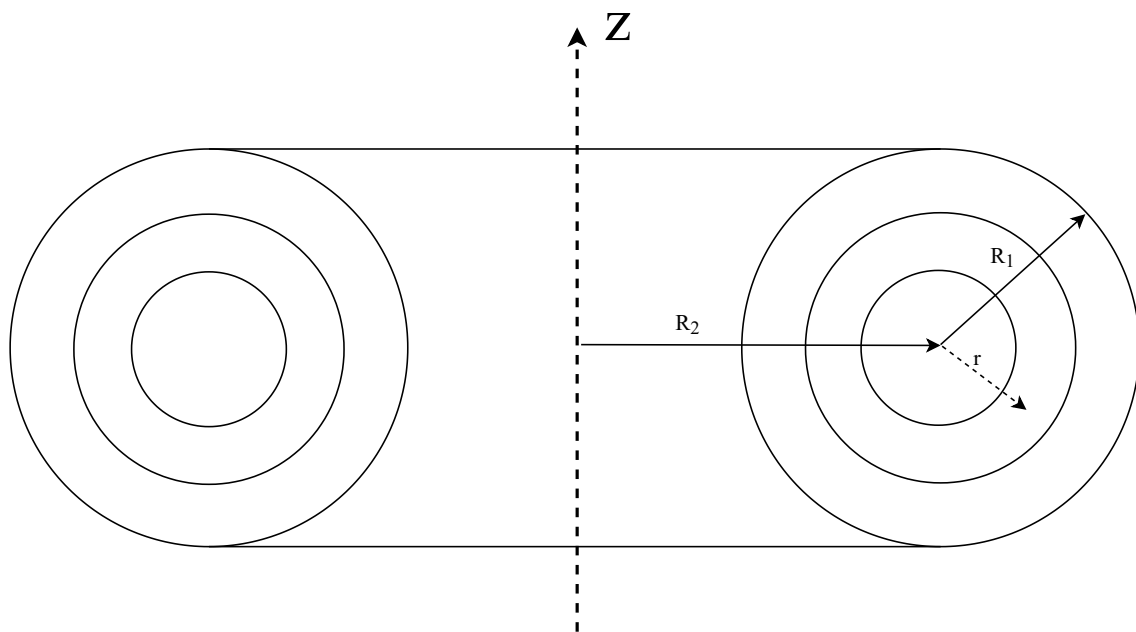


Figure 3.1 – Geometry of the torus.  $R_1$  is the minor radius, and  $R_2$  is the major radius.  $r$  is the variable that enables the analysis of the position inside and outside the solid.

The stratification is done through toroidal shells. Then the Luneburg distribution in Equation 2.22 is applied to the layers depending on the position  $r$ .

Considering the mentioned geometry similarities to the spherical and cylindrical cases, in terms of the cross section on the vertical plane, the main question that arises for the toroidal lens is: what will happen along the azimuth angle, *i.e.* the horizontal plane?

The model was simulated using FEM (Finite Element Method). In a brief explanation, FEM discretizes the structure in small cells by meshing the model. Then, the field equations are evaluated

over those subdomains, and the overall behavior is extracted by evaluating the interaction between all the subdomains [46].

To define the mesh, HFSS computes the associated variation of the solution, called "Delta S", between the neighbor elements. If the variation is above the parameter previously set, it automatically refines the mesh at the corresponding regions, in an adaptive process.

In models with high EM (electromagnetic) power density, such as high quality factor filters and resonators, the mesh refinement can generate an high number of elements to properly analyze the EM behavior. For the case of the toroidal lens design, the only portion of the design with high EM power density is near the antenna, but still the computational effort related to this issue is irrelevant.

The major issue for computational effort faced during the simulations was the analysis of high volume lenses (*e.g.* total diameter above  $10\lambda_0$ ). This difficulty arises due to the exponential/polynomial increase of the mesh elements as the volume increases.

## 3.2 SYMMETRY PLANES

To reduce the computational effort, the model was split at the XY and YZ planes. Then it was applied the symmetry boundary conditions. When this feature is used, HFSS post processor mirrors the far-field solution according to the symmetry conditions [47], yielding a reduction of the processing time for symmetrical structures.

The defined plane works as PEC (Perfect Electrical Conductor) for the E-symmetry and as PMC (Perfect Magnetic Conductor) for the H-symmetry. Therefore, the symmetry type is defined according to the orientation of the electric and magnetic field vectors  $\vec{E}$  and  $\vec{H}$ , based on the image theory. On a PEC plane, the tangential electric fields vanish, remaining only the perpendicular component [11]. The same relation is valid for the PMC and the magnetic field, as depicted in Figure 3.2.

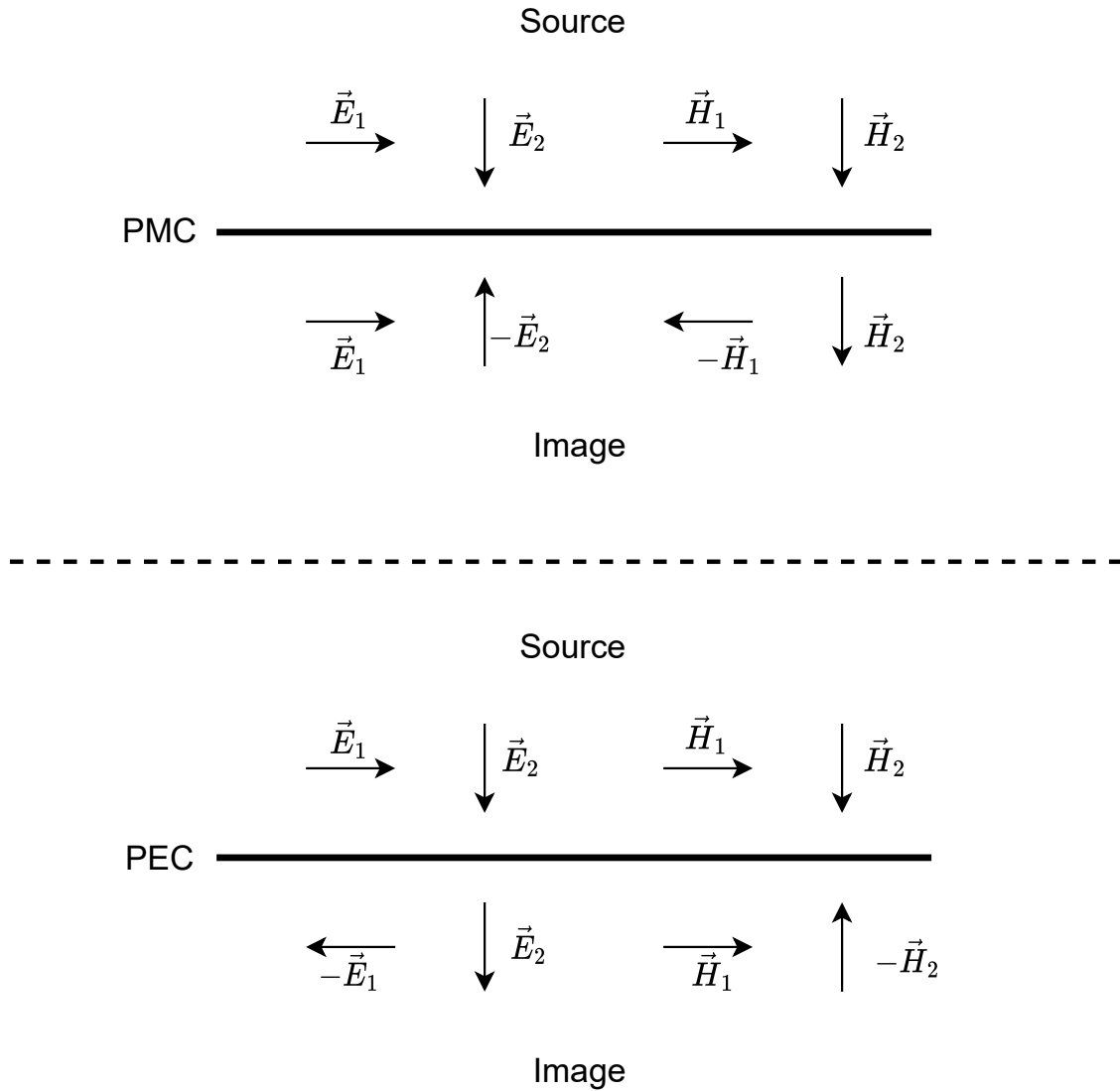


Figure 3.2 – Image theory. On a PEC plane, the tangential components of the electric field vanish due to compensations on the opposite directions, remaining only the perpendicular component. The same relation is valid for the PMC plane and the magnetic field.

On the model used in this work, the symmetry planes are defined at the center, passing through the source (antenna). Given the field vectors on an open-ended waveguide antenna (see Figure 4.5), the XY plane on Figure 3.4 is defined as E-symmetry, because it is perpendicular to  $\vec{E}$  at the source. Similarly, the YZ plane is defined as H-symmetry, given the perpendicularity  $\vec{H}$ . The electric and magnetic planes for the analyzed structure are depicted in Figure 3.3.

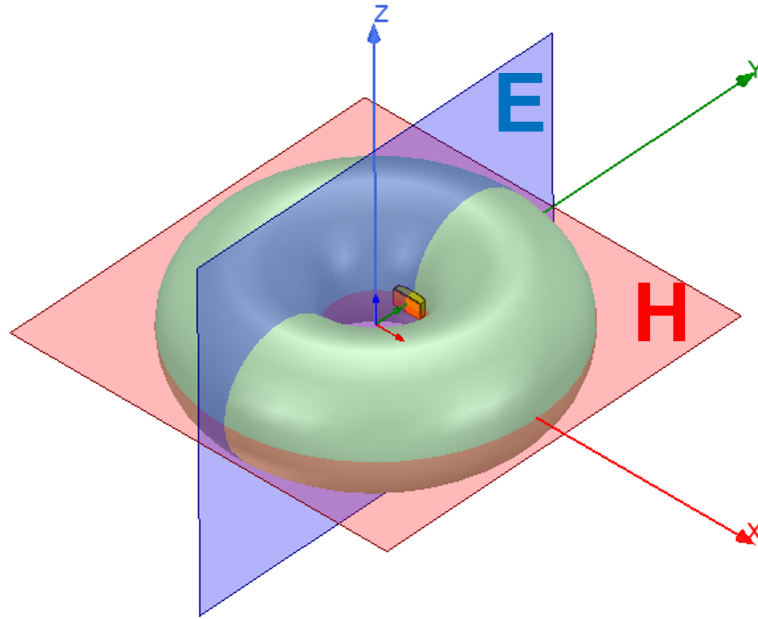


Figure 3.3 – Illustration of the E (electric) and H (magnetic) planes for the analyzed structure.

### 3.3 FEM SIMULATIONS

The simulated model is a 10 layer torus with Luneburg distribution, using the dielectric constants defined using Equation 2.22, with the distribution depicted in Figure 2.9. The lenses were simulated using shells with uniform thicknesses and homogeneous infill, as shown in Figure 3.5. The ideal value of dielectric constant was assigned to each layer according Table 3.1.

Layer	1	2	3	4	5	6	7	8	9	10
$\epsilon_r$ (2.21)	2.00	1.98	1.94	1.88	1.80	1.70	1.58	1.44	1.28	1.10
$r_{uniform}$ <sup>1</sup>	0.10	0.20	0.30	0.40	0.50	0.60	0.70	0.80	0.90	1.00

Table 3.1 –  $\epsilon_r$  distribution for the 10 layer torus. Layer 1 is the core, and layer 10 contains the external boundary. The radius comprehends the outer boundary of each layer, therefore the inner boundary for layer  $n$  is the radius informed on layer  $n - 1$ .

The excitation is done by an open waveguide antenna WR90 [14] positioned at the torus surface and pointed outwards, as depicted in Figure 3.4. The choice of the WR90 waveguide is to match the measurement setup, justified in Section 4.4.

<sup>1</sup>Normalized radius  $r/R_1$



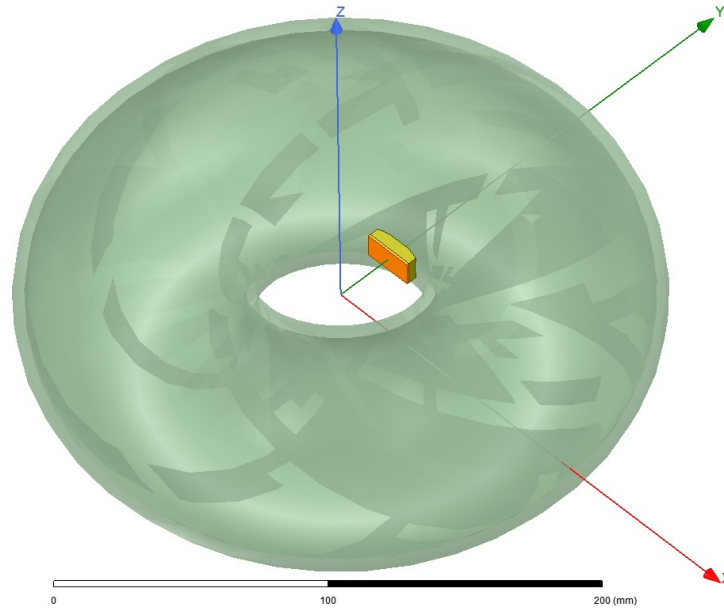


Figure 3.4 – Model of the simulated toroidal lens. The excitation is done by an open waveguide antenna WR90 [14] positioned at the torus surface and pointed outwards, to the  $\hat{y}$  direction.

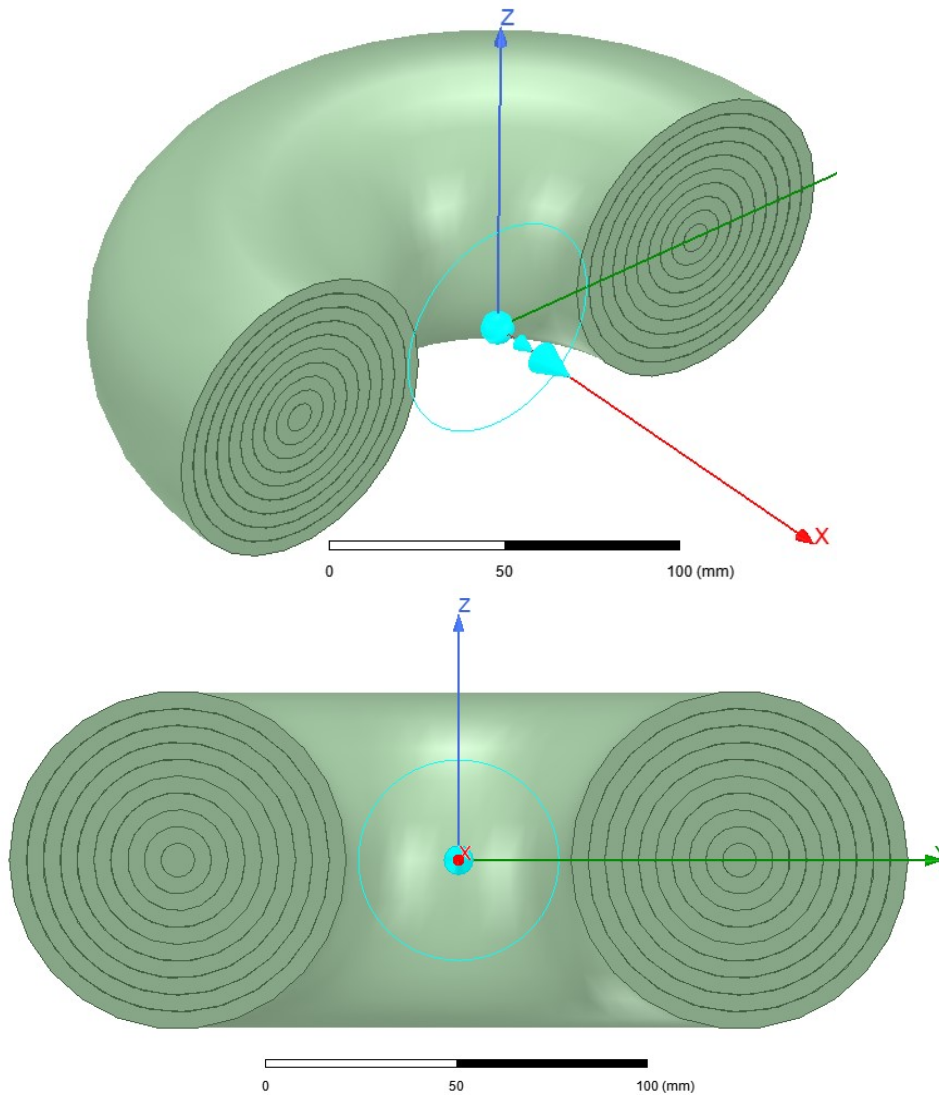


Figure 3.5 – Section view of the 10 layers toroidal lens. The thickness of the shells are uniform, with bounding radius according to Table 4.1.

The special feature to be analyzed about the toroidal lens is its behavior on the horizontal plane considering the torus curvature, which, in the setup of the simulation described in this work, can be evaluated by the directivity on the H-plane. The results are then compared to the cylindrical case, which consists of an extension of a section of the toroid for  $R_2 \rightarrow \infty$ .

Besides the evaluation of the pattern on the horizontal plane, it is interesting to analyze effects of the curvature for antenna positions pointing through different elevation angles, as shown in Figure 3.6, because the path seen on the H-plane is not the same for all the angles.

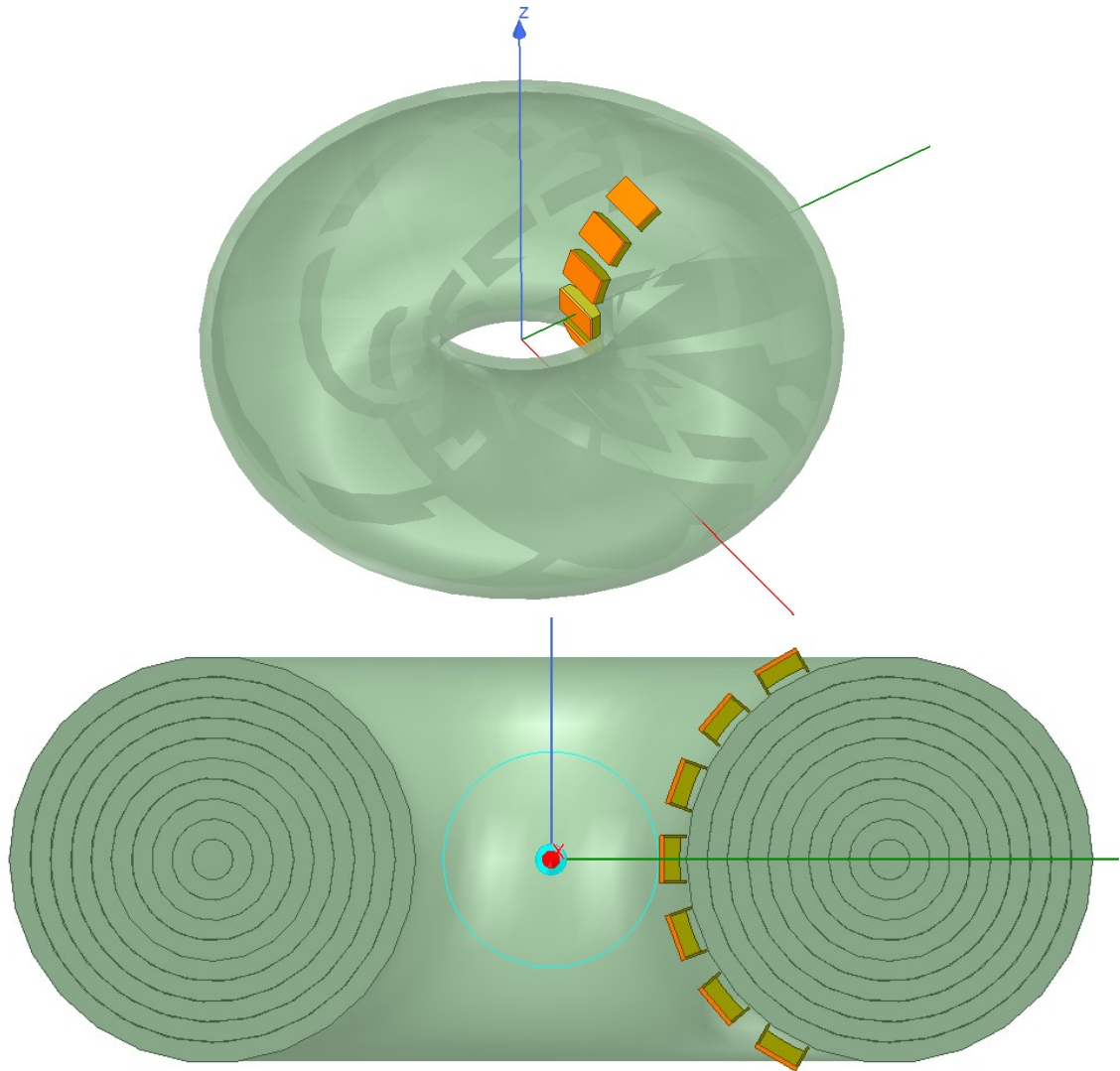


Figure 3.6 – Variation in antenna position along elevation angle. The path seen on the H-plane is not the same for all the angles.

Finally, the idea of a multi-channel lens-antenna setup covering multiple sectors around the origin is depicted in figure 3.7. Considering this, it is necessary to evaluate the isolation between antennas placed along the surface of the torus.

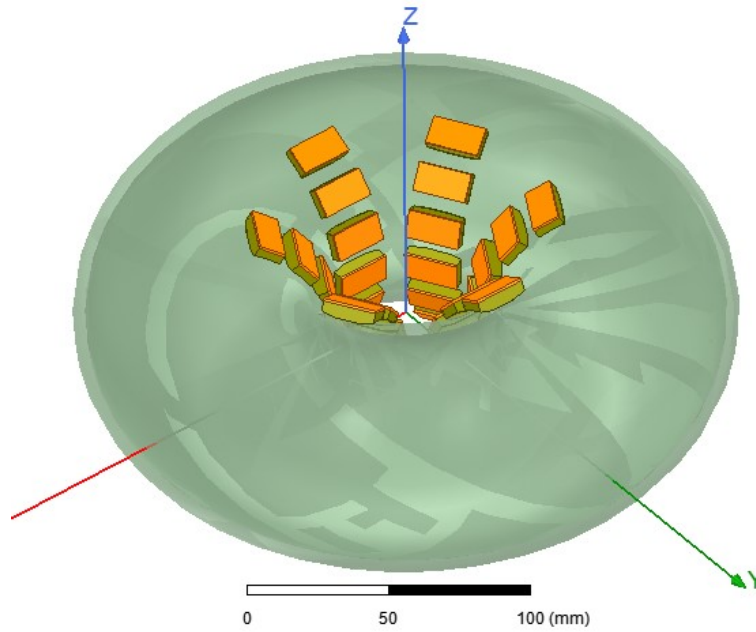


Figure 3.7 – Populated torus. This figure depicts the multi-channel setup, with multiple waveguides covering the space around the lens.

Regarding the size of the lens, it was evaluated the effect of variations on lens parameters  $R_1$  and  $R_2$ , for the same  $\epsilon_r$  and  $r$  distribution (see Table 3.1). When the dimension of the lens is not specified, it is used  $R_1 = 32.50 \text{ mm} = 1.08\lambda_0$  and  $R_2 = 57.50 \text{ mm} = 1.91\lambda_0$ , where  $\lambda_0 = 0.03 \text{ m}$  for the frequency of  $f = 10 \text{ GHz}$ .

On the simulation setup, the maximum Delta S was set to 0.02. When this target is achieved, it is said that the solution is *convergent*. But in some cases, a mesh refinement performed after the first convergent case extrapolates the target, indicating that the solution might not be accurate. Therefore, it was configured a minimum of 3 consecutive convergent steps, assuring a reliable simulation.

### 3.4 SIMULATION RESULTS

Performing the simulations from the setup described in the previous section, the following results were obtained.

Figure 3.8 presents the 3D plot of the directivity for the toroidal lens.

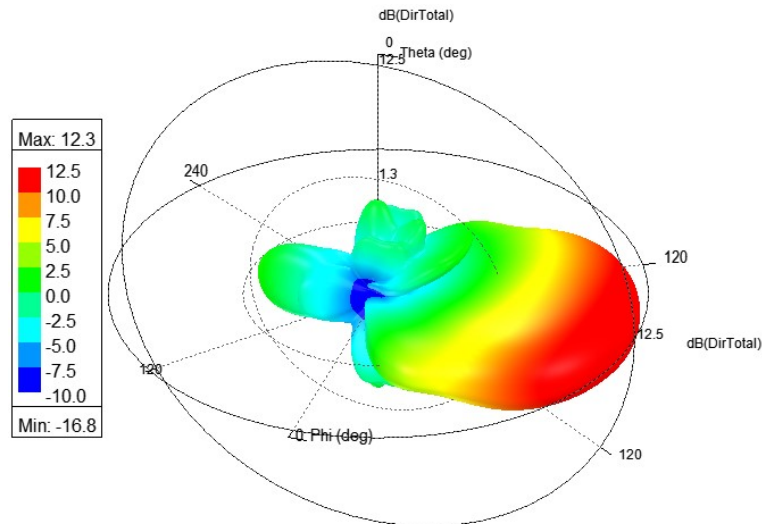


Figure 3.8 – 3D plot of directivity for the toroidal lens with concentric circles profile.

Figures 3.9 and 3.10 show comparisons of the total directivity for E and H plane, respectively, presenting simulation results from the toroidal, cylindrical, and spherical cases, all with cross section radius of  $R_1 = 32.5$  mm. For the toroidal case:  $R_2 = 57.5$  mm. For the cylindrical lens, the extrusion length is  $10\lambda$  (300 mm).

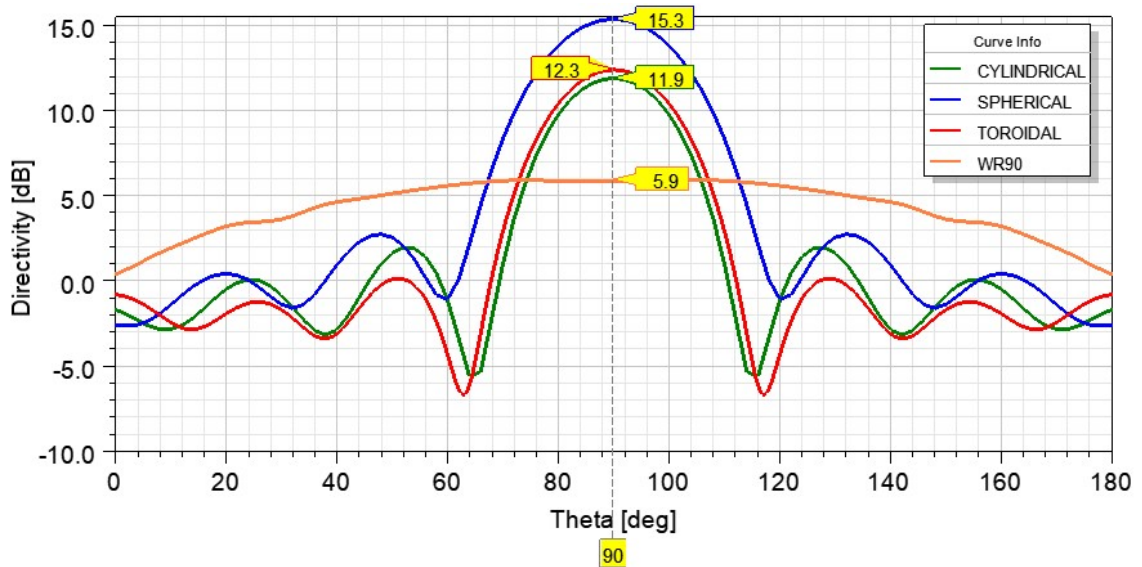


Figure 3.9 – Total directivity on the E-plane for the toroidal, cylindrical, and spherical cases.

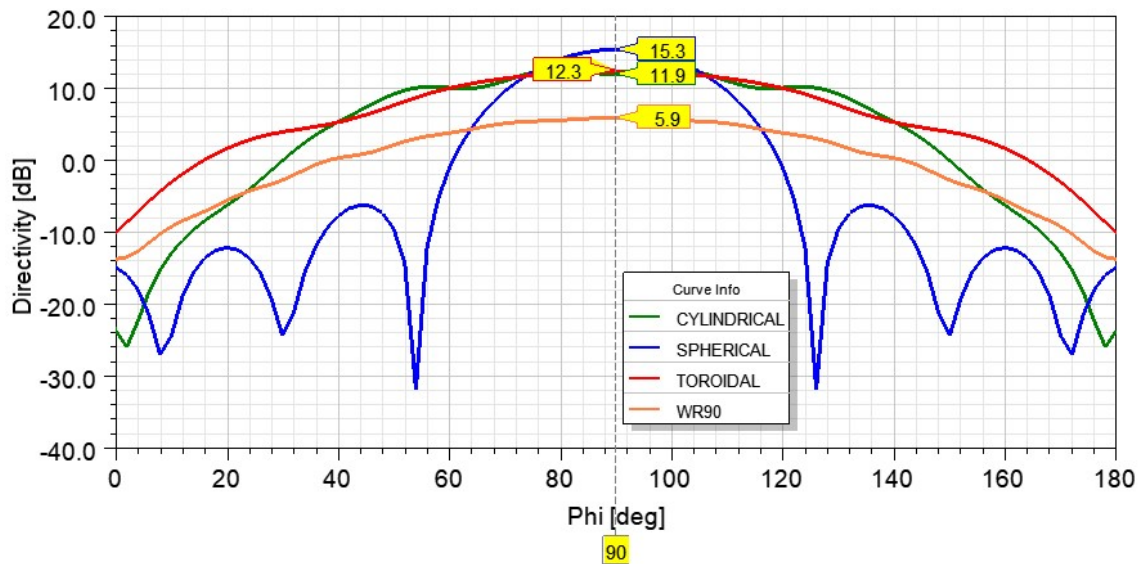


Figure 3.10 – Total directivity on the H-plane for the toroidal, cylindrical, and spherical cases.

It can be observed in Figure 3.10 a reduced ripple on H-plane for the toroidal lens in comparison with the cylindrical.

Next, it is presented the influence of variation of  $R_1$  and  $R_2$ . The linear plots were also imported to enable quantitative comparisons where the curves in decibels (dB) have values close to each other.

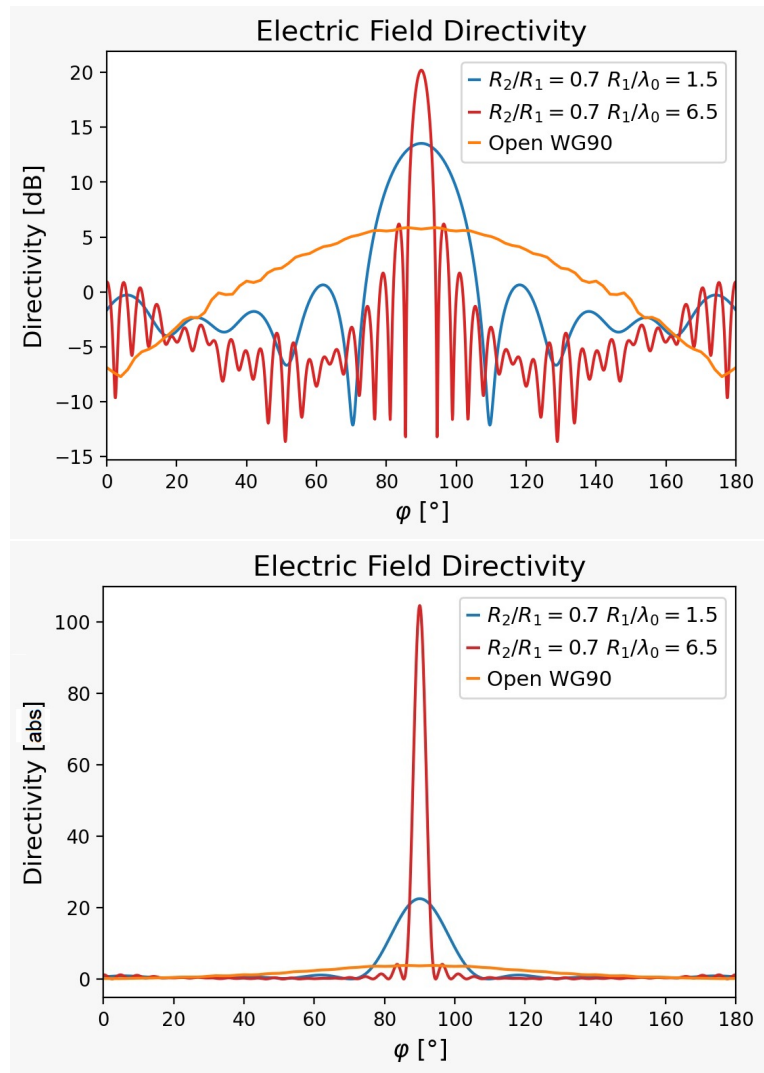


Figure 3.11 – Comparison of directivity in E-plane for values of  $R_1$ . The directivity increases for higher radius.

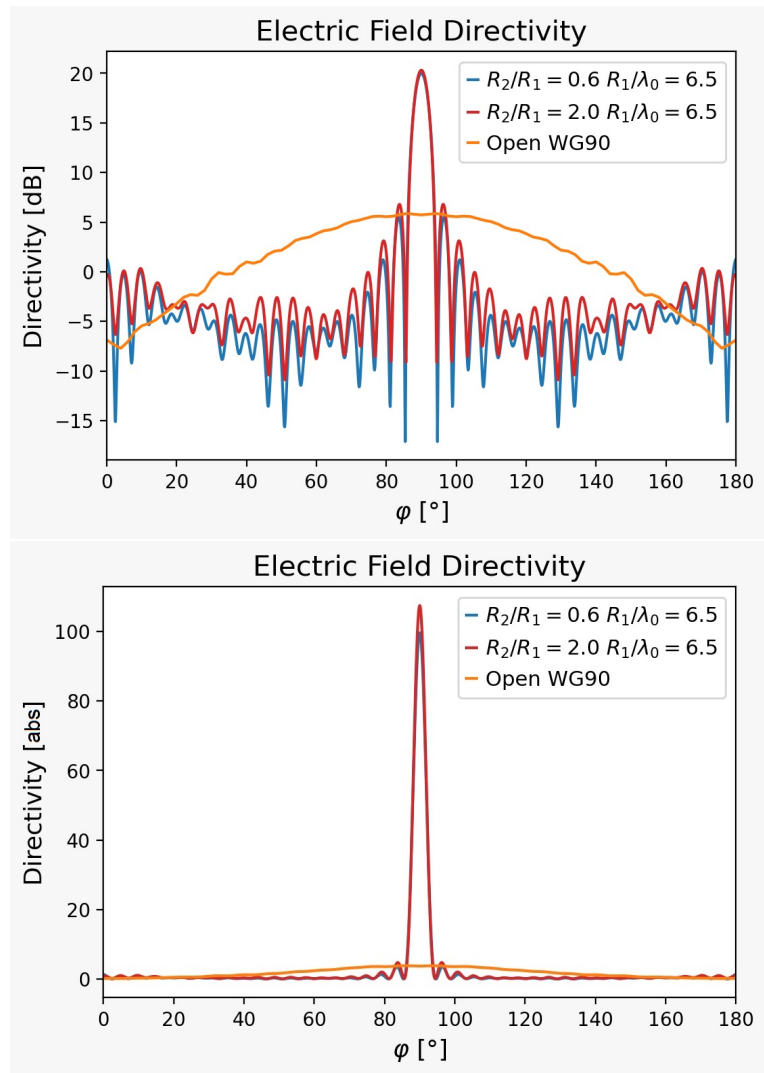


Figure 3.12 – Comparison of directivity in E-plane for values of  $R_2$ . The directivity increases for higher radius.

Now, it is evaluated the impact of the lens on the H-plane directivity.



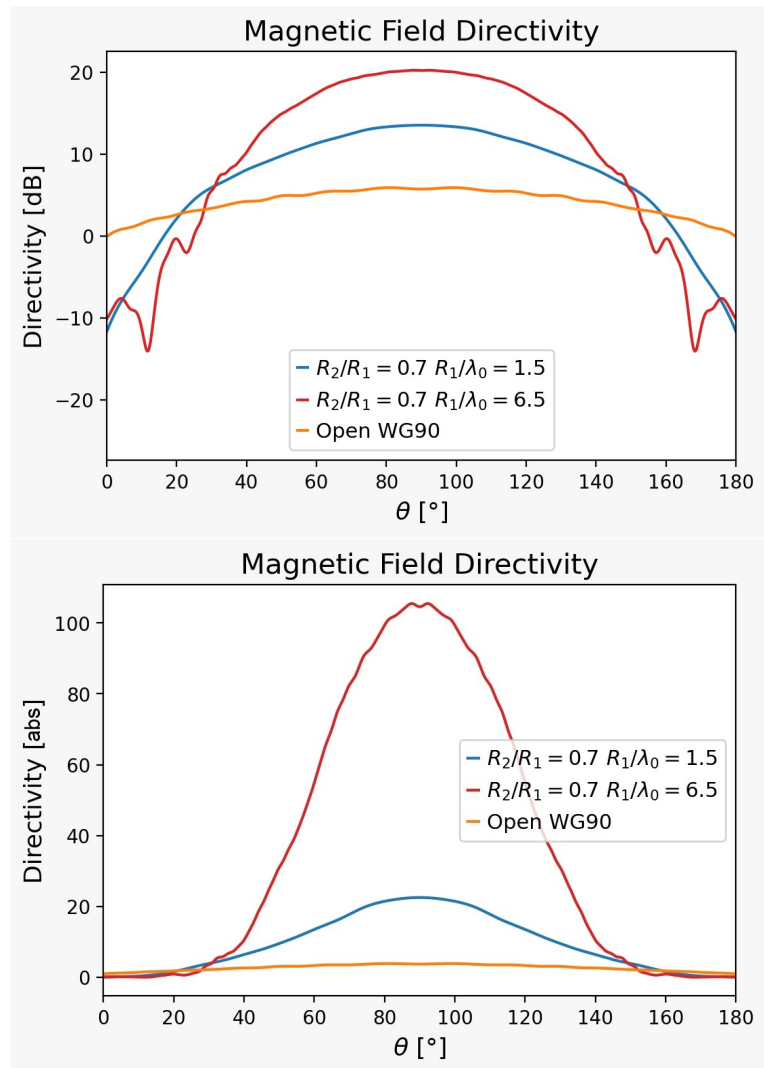


Figure 3.13 – Comparison of directivity in H-plane for values of  $R_1$ . The directivity increases for higher radius.

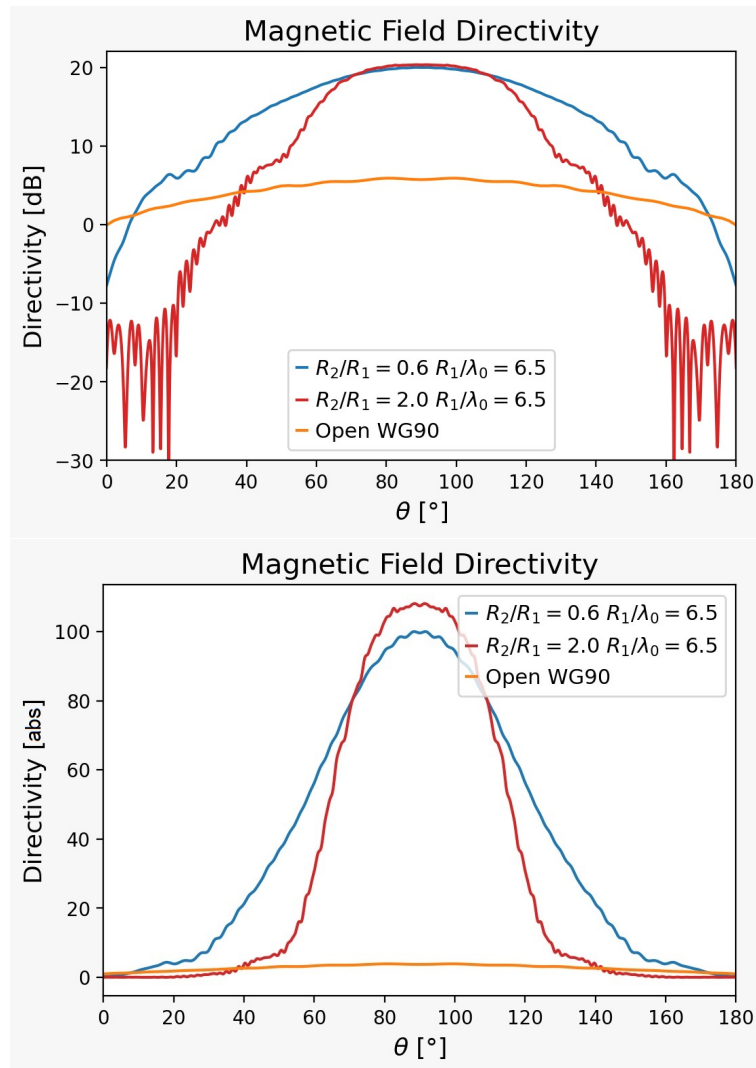


Figure 3.14 – Comparison of directivity in H-plane for values of  $R_2/R_1$ . The directivity increases for higher radius.

The effects of variation in elevation angle are shown in Figure 3.16. The variation in directivity does not cross 1.5% in relation to the  $0^\circ$  elevation, but it is observed a pattern of decline in directivity for angles close to  $45^\circ$ , and an increase as the elevation angle approximates to  $90^\circ$ . Figure 3.15 depicts the elevation angle for reference.

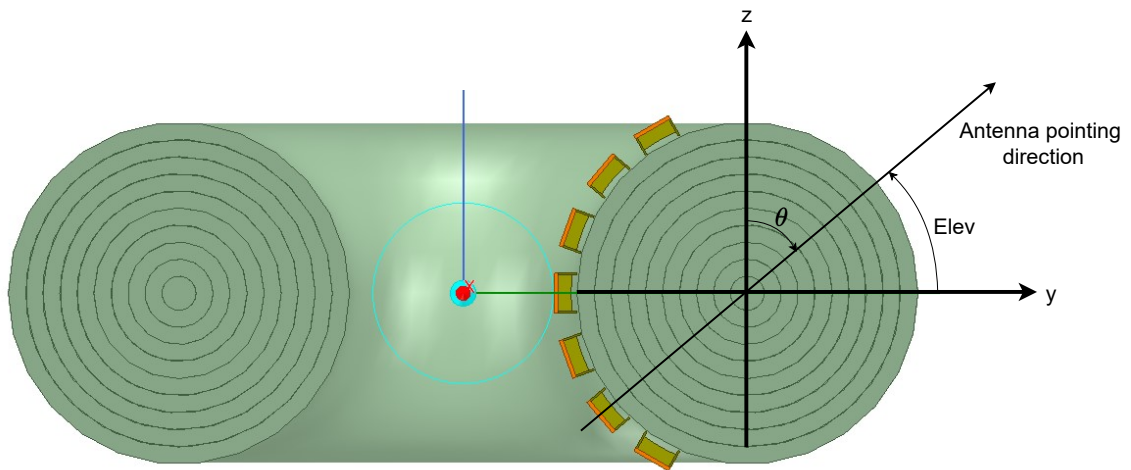


Figure 3.15 – Description of the elevation angle.

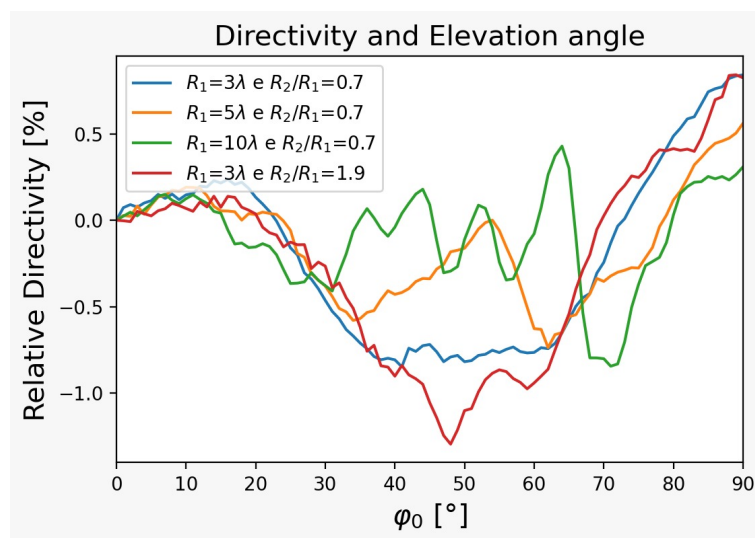


Figure 3.16 – Effects on directivity when the elevation angle of the antenna bore sight is changed. The variation in directivity does not cross 1.5% in relation to the 0° elevation, but it is observed a pattern of decrease in directivity for angles close to 45°, and an increase as the elevation angle approximates to 90°.

Figures 3.17 and 3.18 show the beams for different elevation angles of antenna positioning, for the lens with  $R_1 = 32.5$  mm and  $R_2 = 57.5$  mm.

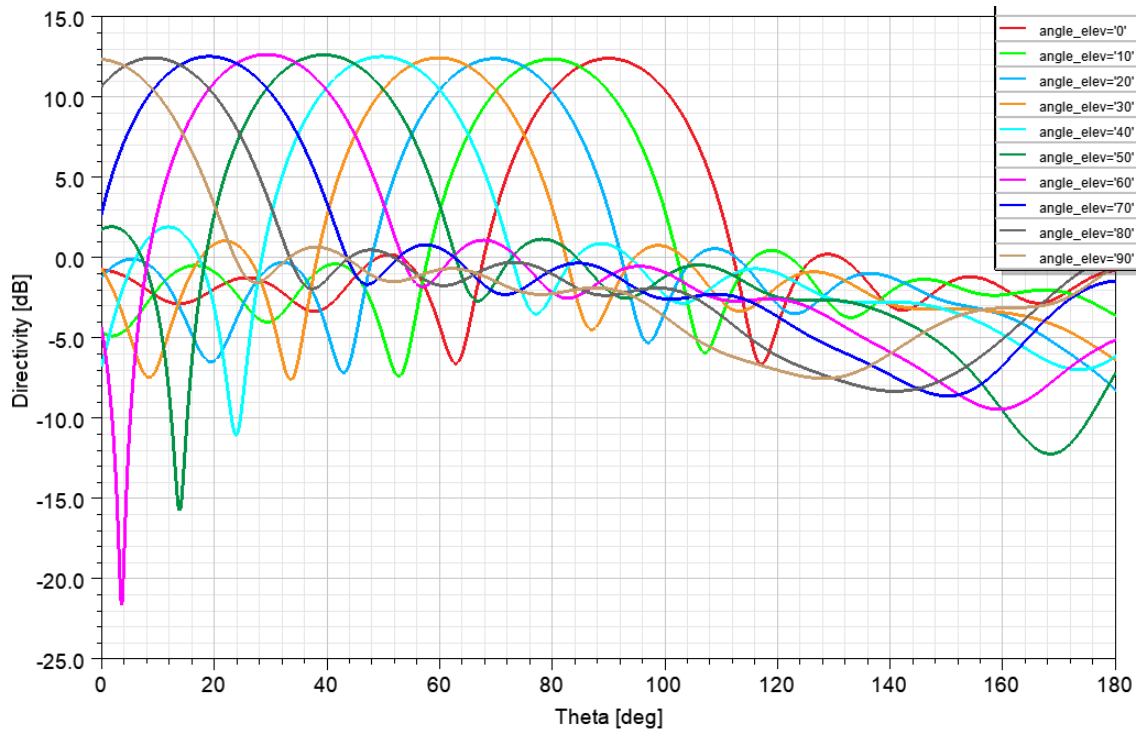


Figure 3.17 – Electric (E) plane of beams for WR90 positioned at different elevation angles.

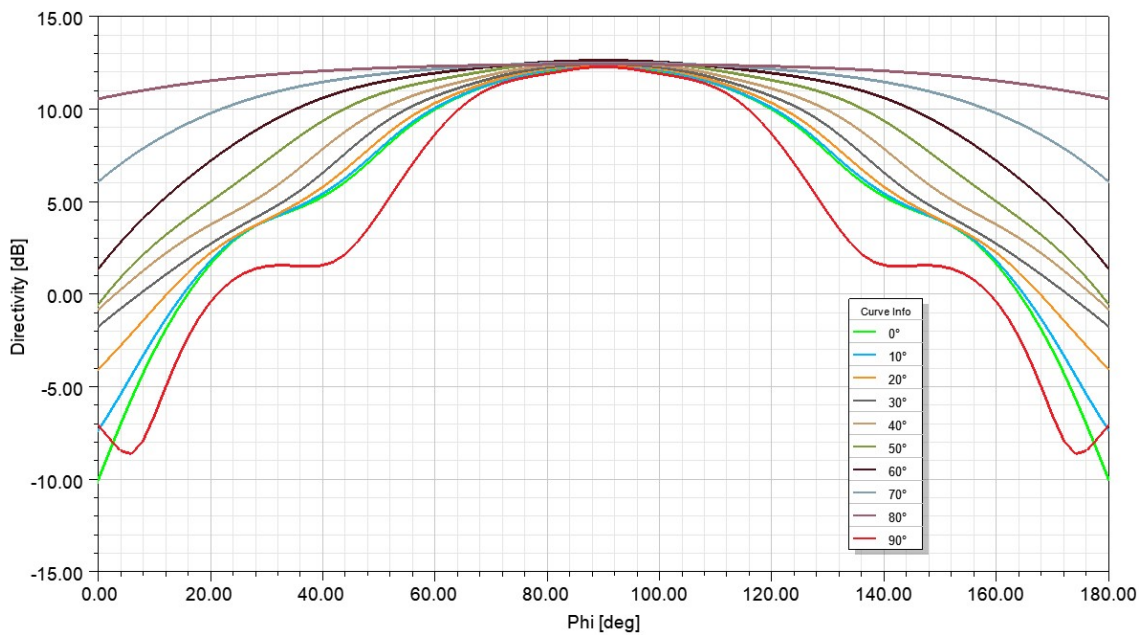


Figure 3.18 – Magnetic (H) plane of beams for WR90 positioned at different elevation angles.

The set of Figures below presents a map of the behavior of the lens for different combinations of  $R_1$  and  $R_2$ . In general, the raise of  $R_2$  tends to modify the characteristics more evidently for the H-plan, due to the variation of the geometry on the optical path, as depicted in Figure 3.19. This variation is more evident for lenses with larger  $R_1$ .

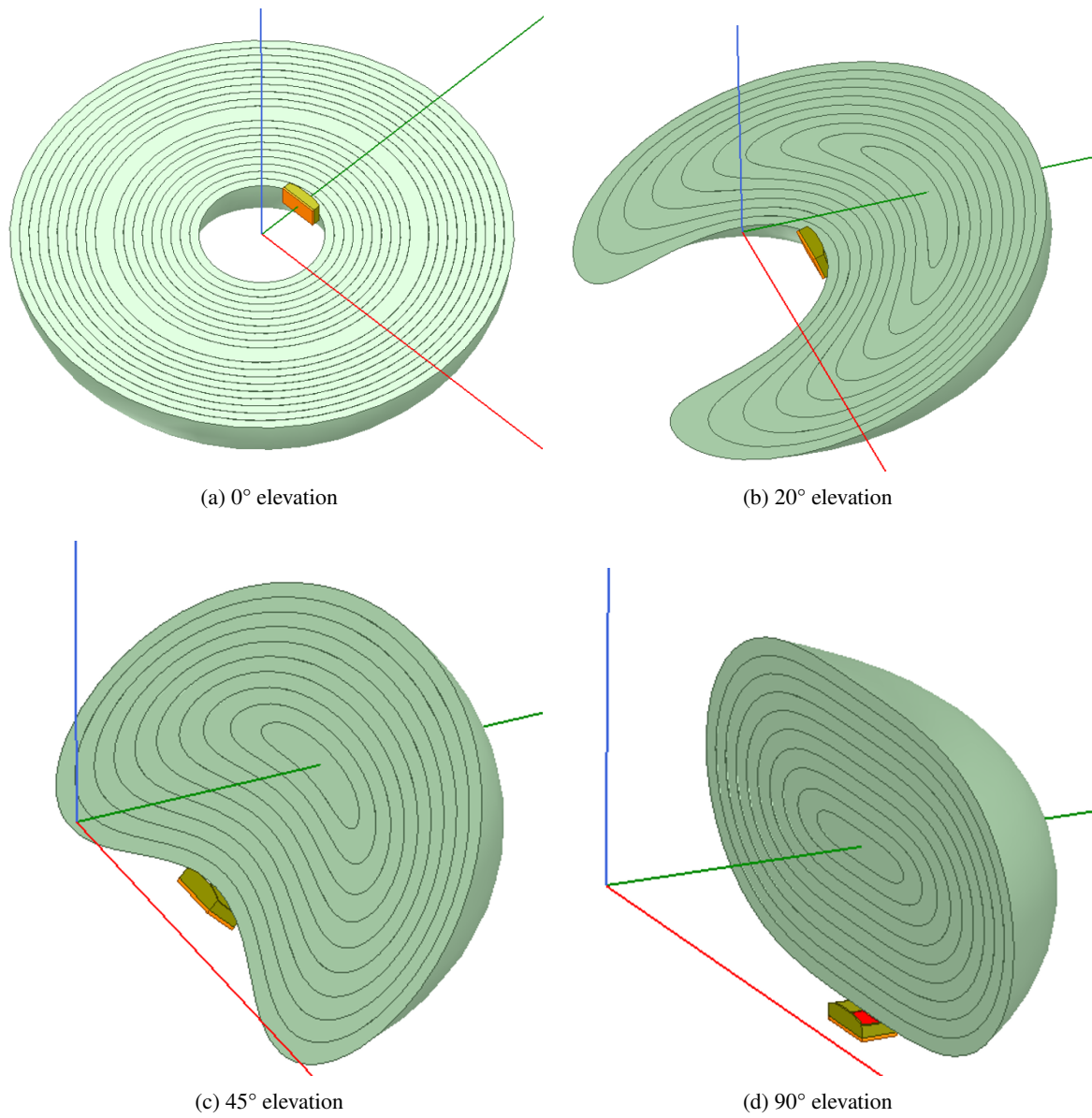


Figure 3.19 – Section view of the magnetic (H) plane for different elevation angles. The geometry seen by the optical path on the H plane varies due to the elevation angle of the antenna.

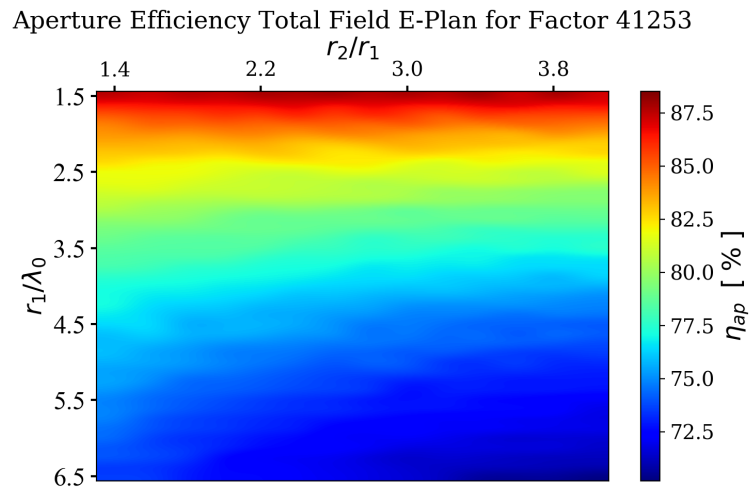


Figure 3.20 – Map of the aperture efficiency for different parameter combinations, based on Equation 2.11.

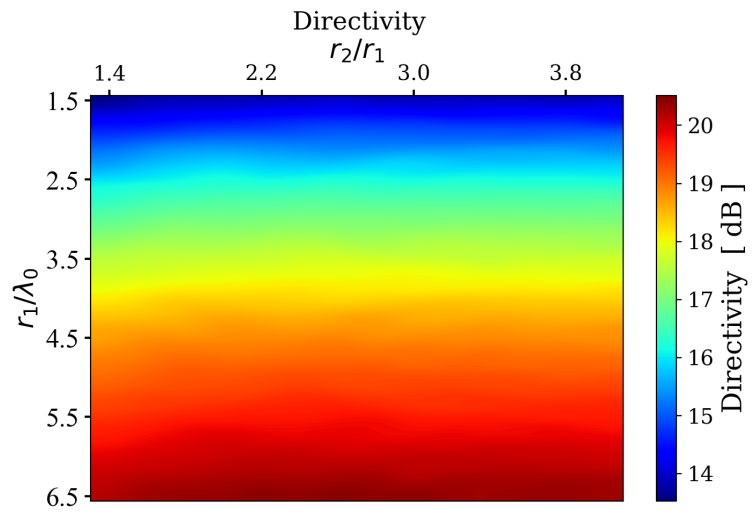


Figure 3.21 – Map of the max directivity for different parameter combinations.

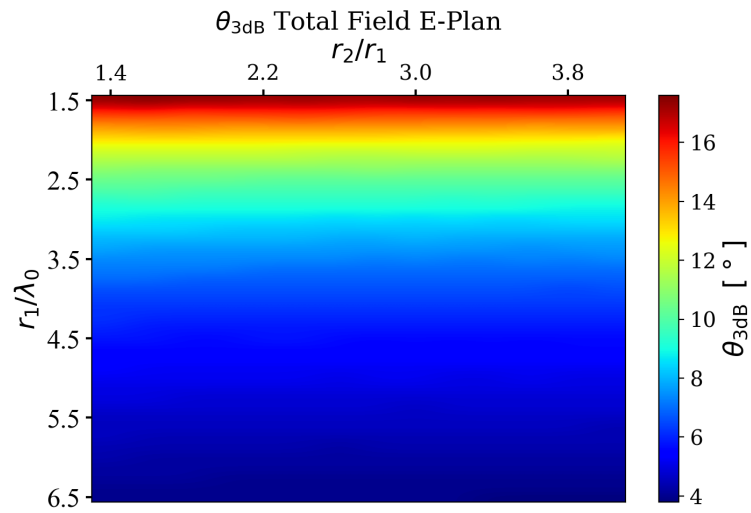


Figure 3.22 – Map of the 3 dB aperture on E-plane for different parameter combinations.

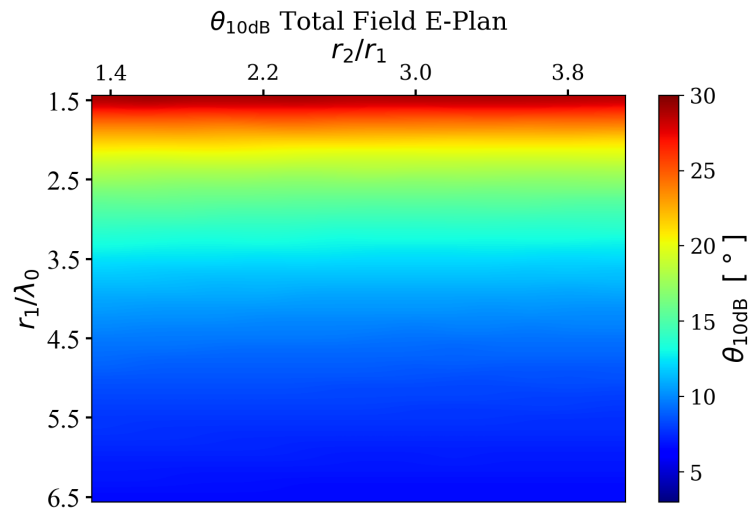


Figure 3.23 – Map of the 10 dB aperture on E-plane for different parameter combinations.

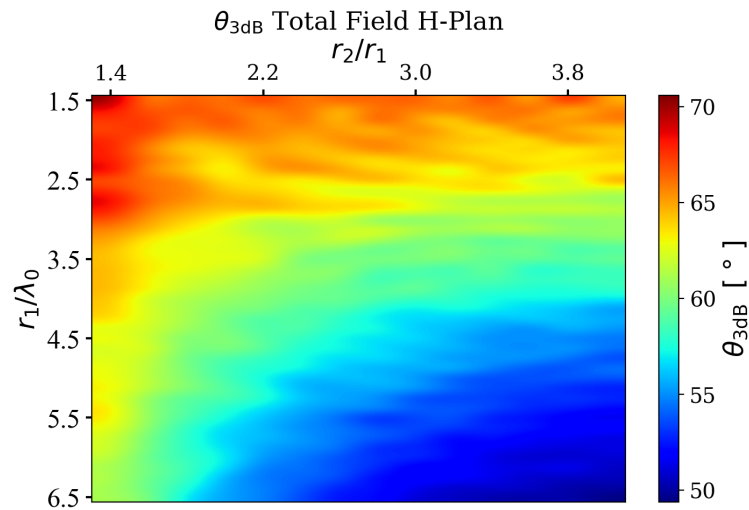


Figure 3.24 – Map of the 3 dB aperture on H-plane for different parameter combinations.

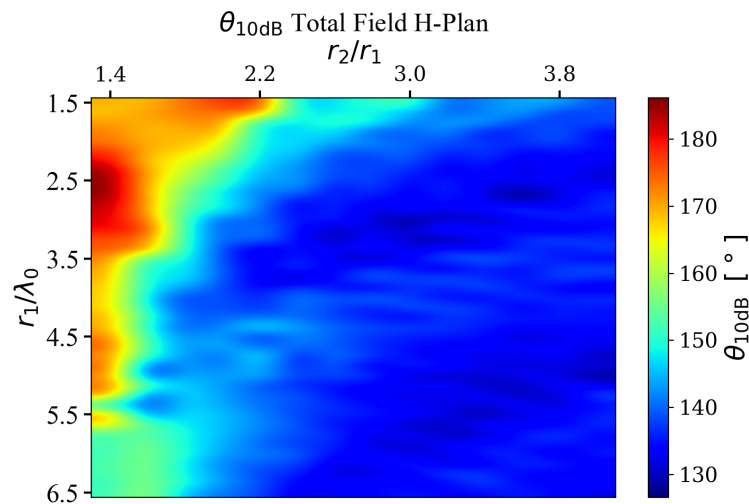


Figure 3.25 – Map of the 10 dB aperture on H-plane for different parameter combinations.

The isolation is evaluated for the positions varying the elevation and azimuth angles. The results are presented in Tables 3.2 and 3.3, respectively.

Antenna elevation angle	20°	30°	40°	45°	50°	60°
0°	-12.4 dB	-14.7 dB	-17.7 dB	-18.5 dB	-18.9 dB	-19.5 dB

Table 3.2 – Isolation results for two WR90 aligned in azimuth, for different elevation angles.

Antennas azimuth angle	60°	70°	80°	90°
0°	-37.2 dB	-42.0 dB	-43.4 dB	-42.4 dB

Table 3.3 – Isolation results for two WR90 aligned in elevation (0°), for different azimuth angles.

A reference limit for isolation adopted by some authors is -15 dB [48]. This value is also used



on commercial applications, as the specification for WLAN (Wireless Local Network) system from CYPRESS, in [49].

Therefore, the isolation results obtained are satisfactory for elevation angle difference above 30°, and for all azimuth angles evaluated. Here it is important to notice that the minimum possible angle between antennas is limited by the shape of the device.

The isolation is strongly dependent on the antenna type. Moreover, different techniques for mutual coupling reduction can be employed depending on the chosen antenna element, as reviewed by [50].

### 3.5 CHARACTERIZATION OF FIGURES OF MERIT

To characterize the half power beam width on both magnetic and electric plane, and the total directivity as a function of  $R_1$  and  $R_2$ , it was used the regression method.

Tests were performed using various types of functions, that were later inserted on an optimization routine written in Python to find the coefficients.

Then, the error associated with the function was calculated in relation to the values collected from the simulated samples. To do so, two error metrics were used: *MAE* (*Mean Absolute Error*) and *MSE* (*Mean Squared Error*) represented in Equations 3.1 and 3.2.

$$MAE = \frac{\sum_{i=1}^n |Y_i - X_i|}{n} \quad (3.1)$$

$$MSE = \frac{1}{n} \sum_{i=1}^n (Y_i - X_i)^2 \quad (3.2)$$

Where:

- $n$ : number of samples;
- $Y_i$ : value of the sample;
- $X_i$ : predicted value;

#### 3.5.1 Characterization of $\theta_{3\text{dB}}$ on the Magnetic Plane

Observing Figure 3.24 it is possible to see an exponential relation between  $\theta_{3\text{dB}}$  and  $R_2/R_1$ . After testing several functions, Equation 3.3 was found to be appropriate to represent this behavior.

$$\theta_{3\text{dB, H}} [^\circ] = b_0 - b_1 \exp \left[ \frac{b_2}{b_3 + b_4(R_2/R_1) + b_5(R_2/R_1)^2} - \frac{b_2}{b_6 + b_7(R_1/\lambda_0) + b_8(R_1/\lambda_0)^2} \right] \quad (3.3)$$

The function implemented by Equation 3.3 was optimized, yielding the coefficients in Table 3.4.

Coefficient	Value
$b_0$	69.303
$b_1$	32.862
$b_2$	33.512
$b_3$	15.935
$b_4$	-17.299
$b_5$	-11.693
$b_6$	13.922
$b_7$	-1.286
$b_8$	1.963

Table 3.4 – Values found for the coefficients in Equation 3.3.

Therefore, based on Equations 3.1 and 3.2, the errors associated to Equation 3.3 are listed in Table 3.5.

Metric	Error	Value
MAE	Absolute	0.667
MSE	Square	0.781

Table 3.5 – Errors related to the samples of 3 dB beam width on the magnetic plane referent to the modeling function in Equation 3.3.

The visualization and comparison between the results sampled directly from the FEM simulation and the results from the model are shown in Figure 3.26.

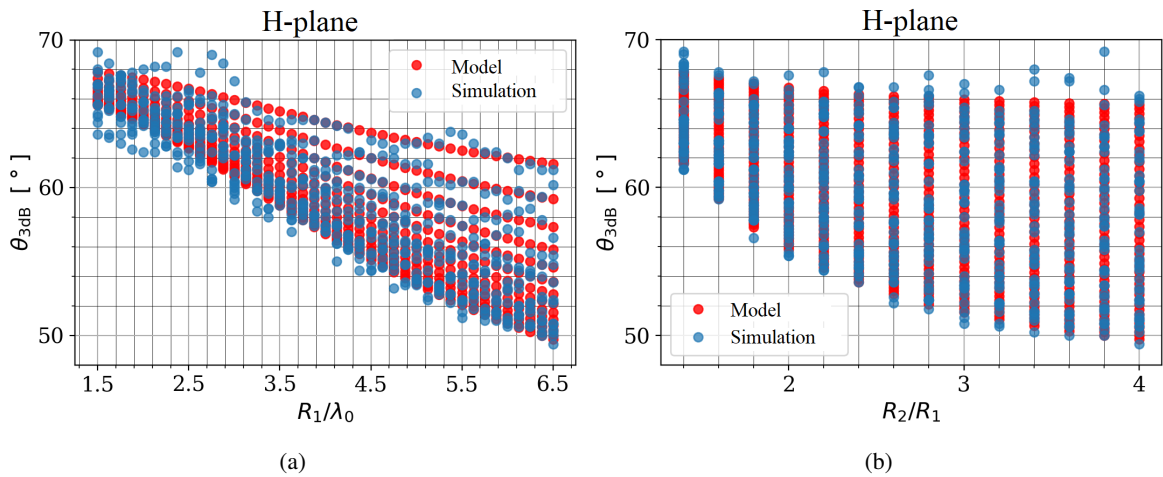


Figure 3.26 – Comparison between FEM simulation and model results for the half-power beam width in the magnetic plane.

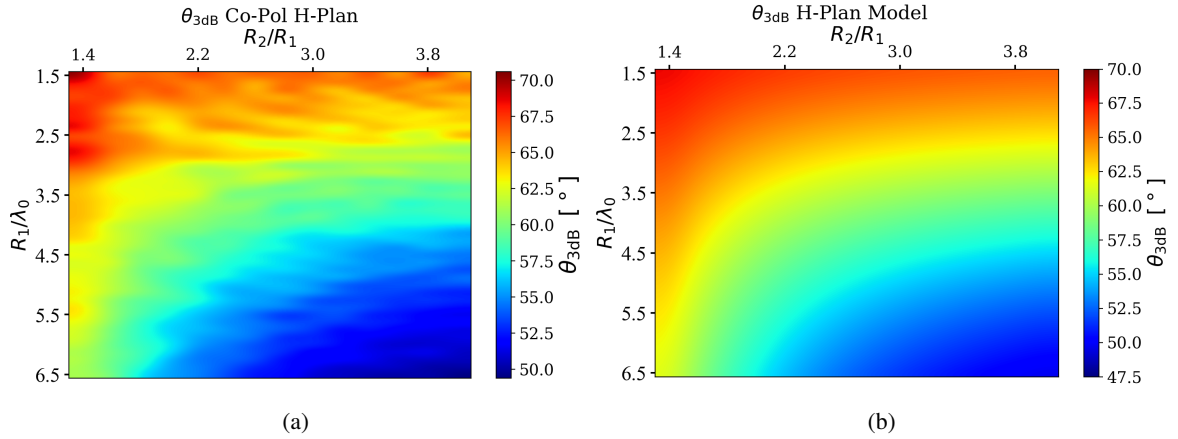


Figure 3.27 – Maps of the FEM simulation and model results for the half-power beam width in the magnetic plane.

From Figures 3.26 and 3.27 it was found that the behavior of the function matches the behavior of the measured samples, despite some distortions in some simulation samples.

### 3.5.2 Characterization of $\theta_{3\text{dB}}$ on the Electric Plane

The same technique was applied for the electric plane. Analyzing Figure 3.22, it was identified an inversely proportional behavior of the beam width in relation to the  $R_1/\lambda_0$ , hence Equation 3.4 is more suitable to represent this property, among the tested functions.

$$\theta_{3\text{dB}, E} [^\circ] = -b_0 + b_1 \lambda_0 / R_1 \quad (3.4)$$

The values of the coefficients found by optimization are listed in Table 3.6

Coefficient	Value
$b_0$	0.100
$b_1$	26.035

Table 3.6 – Values found for the coefficients of Equation 3.4.

The errors linked to the function were extracted from the Equations 3.1 and 3.2 and the heat map illustration was also performed, and are shown in Table 3.7.

Metric	Error	Value
MAE	Absolute	0.065
MSE	Square	0.007

Table 3.7 – Errors related to the 3 dB beam width simulation in the electrical plane referring to the model function in Equation 3.4.

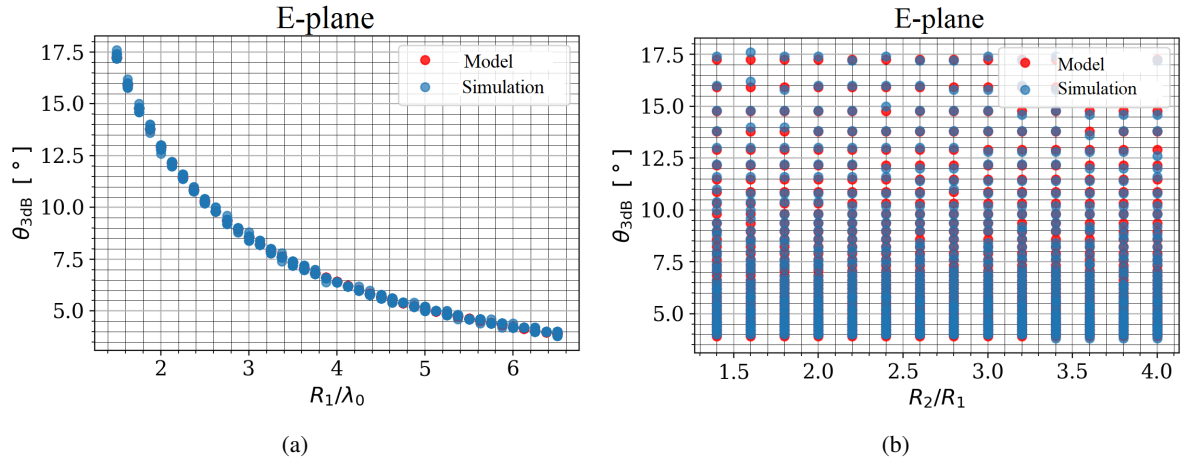


Figure 3.28 – Comparison between FEM simulation and model results for the half-power beam width in the electric plane.

During the analysis of the Figures 3.28a it can be seen that the behavior of the model function is in accordance with what was found in the simulations, without significant disturbances. As can be seen in Figure 3.28b the variation caused by the variable  $R_2/R_1$  is very small so that it can be neglected during the analysis of the property's modeling.

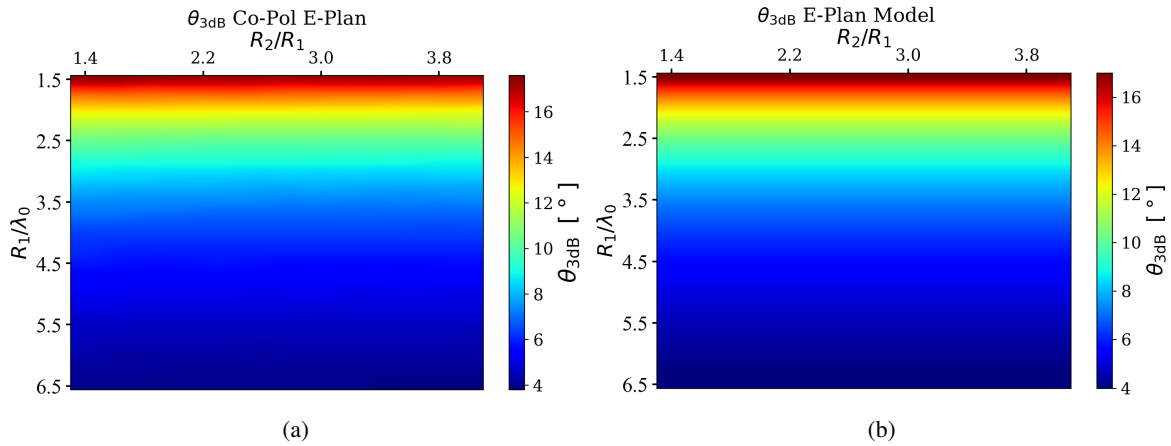


Figure 3.29 – Maps of the FEM simulation and model results for the half-power beam width in the electric plane.

Analyzing the heat maps based on Figure 3.29, it can be observed that the model does not present considerable changes in relation to the heat map of the simulations.

### 3.5.3 Directivity Characterization

Analyzing Figure 3.21 it was observed that the directivity relationship with the variable  $R_1/\lambda_0$  was directly proportional, however it was it grew more sharply for smaller values, meaning that it behaves exponentially. So, among the functions tested, Equation 3.5 was found to be the one appropriated this property.

$$D [\text{dB}] = b_0 + b_1 e^{(-b_2 \lambda_0)/R_1} \quad (3.5)$$

After optimizations of Equation 3.5, the values of the coefficients listed in Table 3.8 were found.

Coefficient	Value
$b_0$	12.098
$b_1$	12.849
$b_2$	2.895

Table 3.8 – Value found for the coefficients of Equation 3.5.

Through the Equation 3.5 the errors related between the modeled sample and the simulations were calculated, being cataloged in the Table 3.9.

Metric	Error	Value
MAE	Absolute	0.068
MSE	Square	0.008

Table 3.9 – Errors related to the total directivity referring to the function in Equation 3.5.

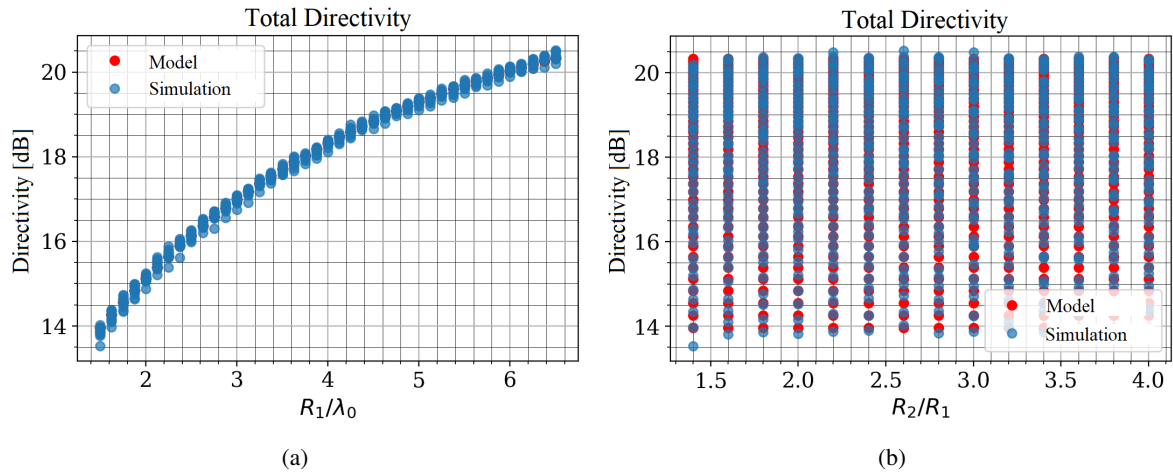


Figure 3.30 – Comparison between FEM simulation and model results for the total directivity.

From Figure 3.30a it can be verified that the model results behaved according to the the FEM simulations, confirming that the model function chosen is appropriated. And from Figure 3.30b it can be seen that the variation of  $R_2/R_1$  really does not significantly influence the behavior of the total directivity of the lens.

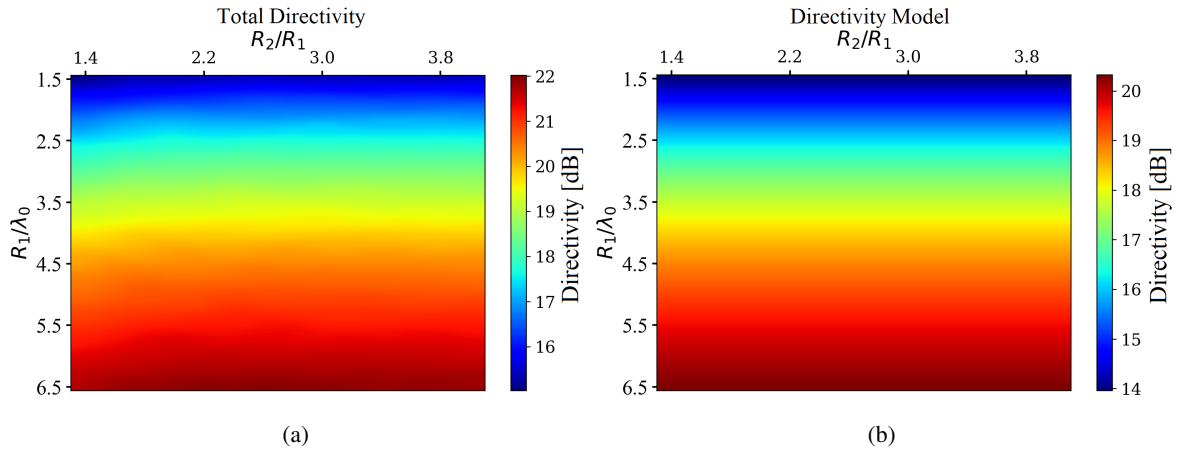


Figure 3.31 – Maps of the FEM simulation and model results for the half-power beam width in the electric plane.

From Figure 3.31 it can be seen that the behavior of the function used to model the behavior of the total directivity presented results very similar to those from the FEM simulations.

### 3.6 TOROIDAL LENS DESCRIBED IN TOROIDAL COORDINATES

The lens described in toroidal coordinates, as mentioned in Section 1.4, is also feasible. The cross section of the lens with with such geometry is depicted in Figure 3.32.

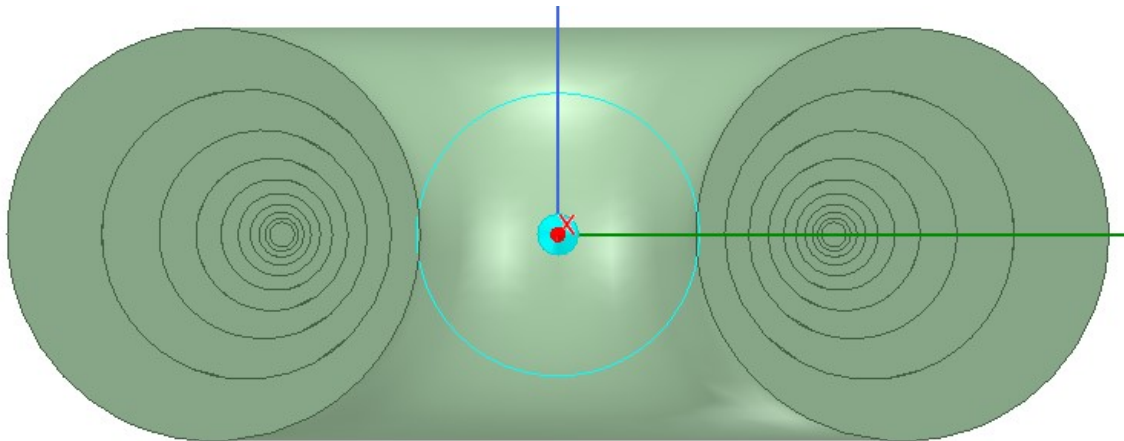


Figure 3.32 – Cross section of the toroidal lens described in toroidal coordinates. Due to the coordinate system properties, the circular profiles that form the torus are not concentric.

As mentioned in previous sections, the theory described in Appendix A is not complete yet, but simulations of the structure shows that it is possible to achieve a radiation pattern with shape similar to the one from the lens with concentric circles profile from Figure 3.5, as shown in Figures 3.33 to 3.35.

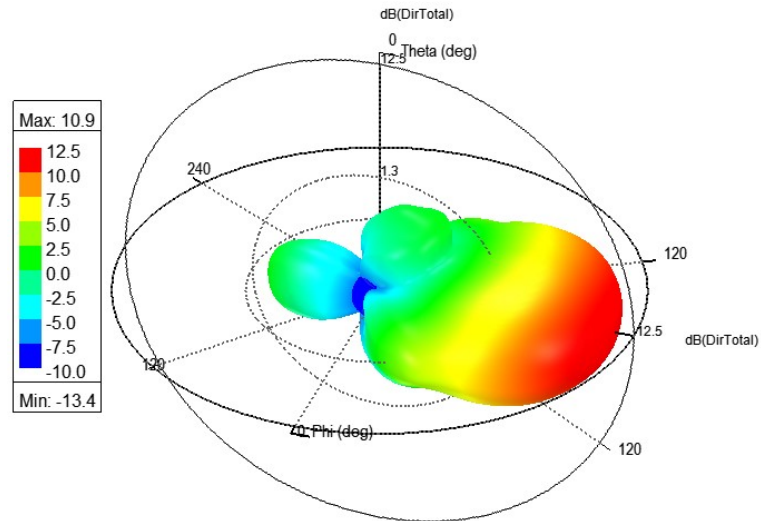


Figure 3.33 – 3D plot of directivity for the toroidal lens described in toroidal coordinates.

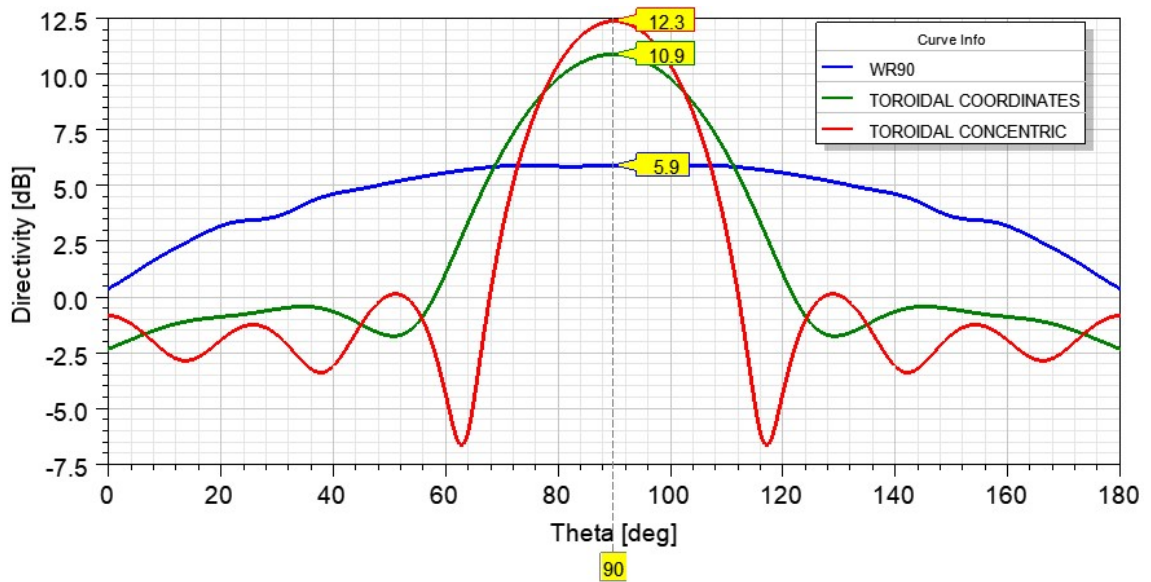


Figure 3.34 – Total directivity on the E-plane for the toroidal lenses with concentric circles and in toroidal coordinates.

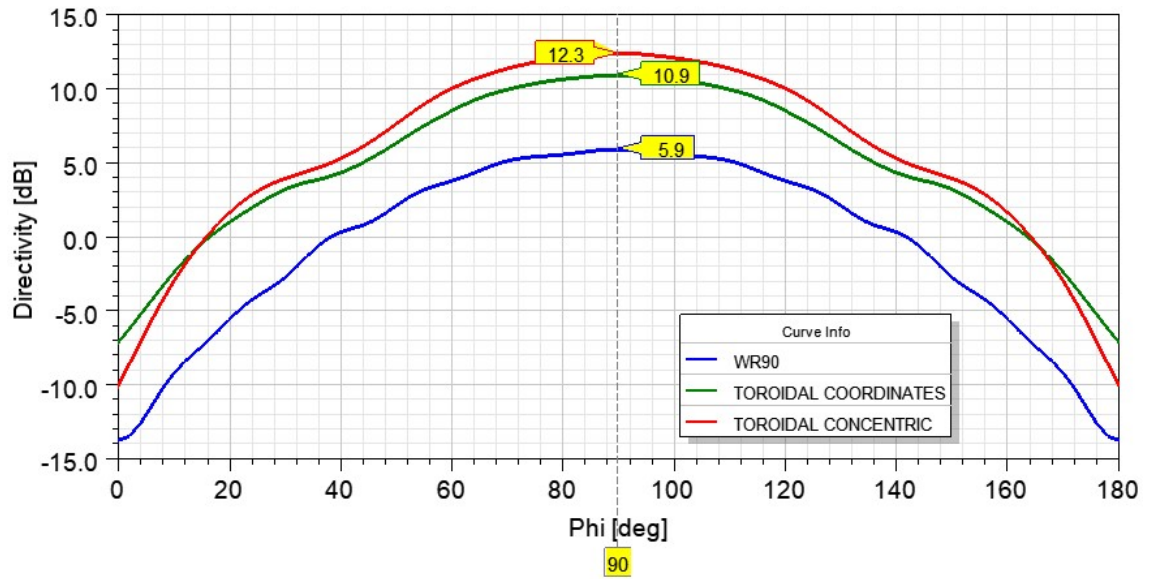


Figure 3.35 – Total directivity on the H-plane for the toroidal lenses with concentric circles and in toroidal coordinates

The external sizes of the simulated lens in Figure 3.32 are the same as the one in Figure 3.5. The lens also have 10 layers, and each layer with the same  $\epsilon_r$  indicated in Table 4.1. The difference lies on the center of the circular profile determined by  $R_2$ , and the non-uniform layer thicknesses. This implies a distribution of  $\epsilon_r$  different from the one in Equation 2.22. Hence, the performance of the lens in terms of total directivity is lowered, according to the comparisons in Figures 3.34 and 3.35.

Nevertheless the simulation results corroborate to the proposal of study on the analytical solutions for the toroidal lens using toroidal coordinates, presented in Appendix A.



# 4

## MATERIALS AND METHODS

---

This chapter presents the physical issues involved on the realization of the lens prototype.

The 3D printer used is a modified version of Stratasys SST 1200es, which is described in [43]. It is based on FDM (Fused Deposition Modeling) technology, which consists on additive building of the part by fusion and deposition of the printing material.

The nozzle used has 0.25 mm of diameter. This imposes some limitations depending on the method for modeling the lens, which is explained in further sections.

### 4.1 MATERIAL CHARACTERIZATION

Some commercial 3D printing filaments manufacturers generally do not specify electromagnetic properties of the materials, such as permittivity, so it was necessary to perform the characterization of this feature to have accurate values inside the lens. This is done following the steps detailed in this section.

The material used was a natural color ABS (Acrylonitrile butadiene styrene) from *3D Fila* [51], its nominal density informed by the manufacturer is  $1.06 \text{ g/cm}^3$ . The natural color material was chosen to avoid influence of pigmentation differences to the analysis.

There were printed sample blocks, varying the infill ratio, with dimensions:

$$a = 22.90 \text{ mm}, b = 10.11 \text{ mm}, \text{ and } L = 7.50 \text{ mm (see Figure 4.1).}$$

The specified dimensions are to fit the WR90 TRL calibration kit, presented later. Some of the printed samples are shown in Figure 4.4. Each sample was weighted on a scale with 0.1 mg precision to evaluate the real infill ratio.

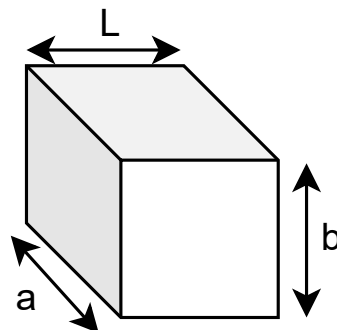


Figure 4.1 – Sample block dimensions. The sample fits the WR90 TRL calibration kit in order to extract the dielectric constant of the material. For this work, it was used:  $a = 22.90 \text{ mm}$ ,  $b = 10.11 \text{ mm}$ , and  $L = 7.50 \text{ mm}$ .

### 4.1.1 Data acquisition

The samples were measured using the WR90 waveguide TRL (Transmission-Reflection-Line) calibration kit of Figure 4.3, using the line component as sample-holder.

The acquisition process is described in Figure 4.2 [52], [53]. First, the VNA is calibrated using the *full-2-port* mode to shift the reference plane of the all the measurements to the tip of the SMA cable [54]. The TRL calibration is actually done afterwards using an algorithm, with calculations using the S-parameters data from the Transmission, Reflection (Open), and Line measurements. When the TRL calibration is performed, the reference plane of the scattering parameters from the MUT (material under test) measurements are shifted to the faces of the sample.

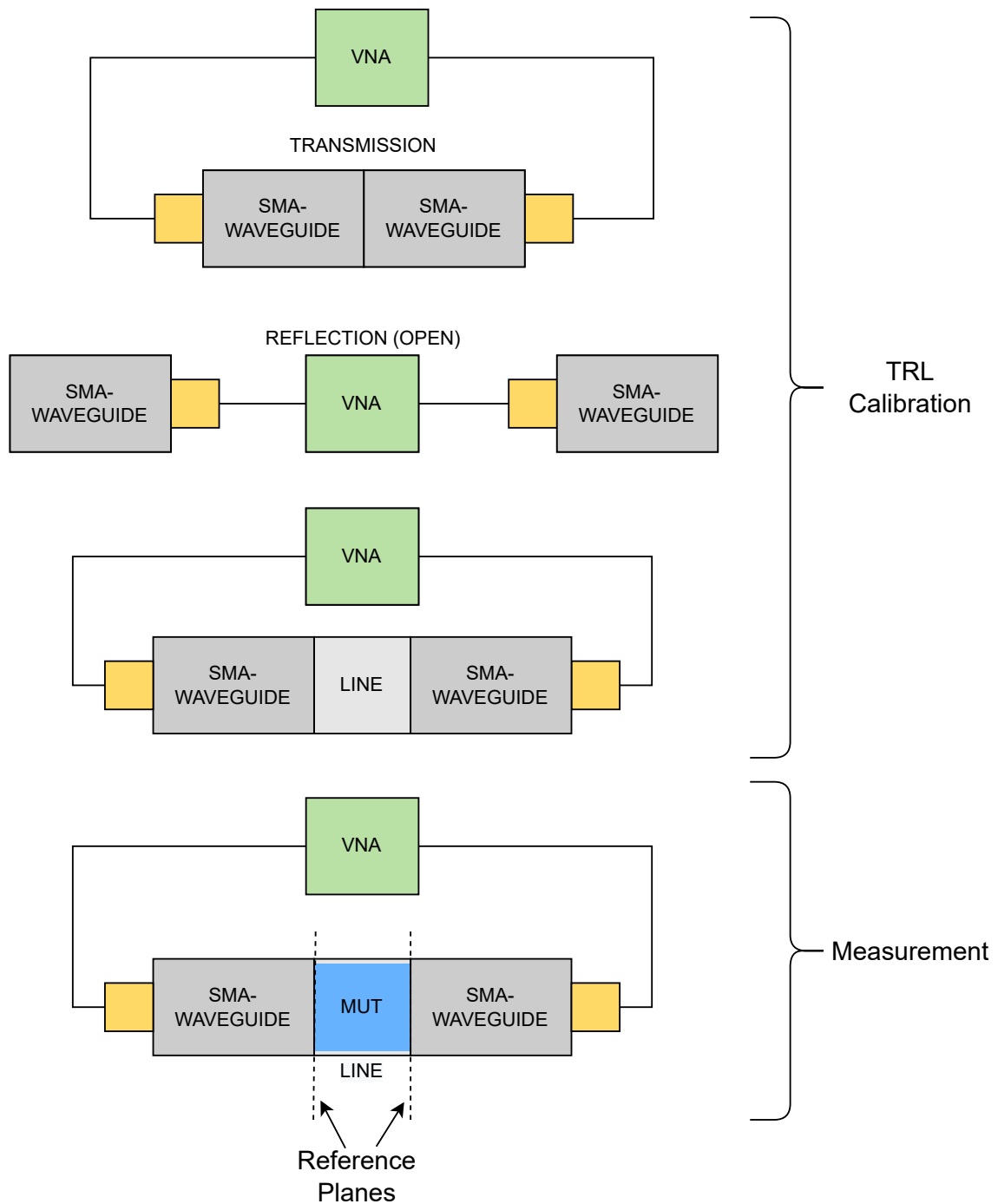


Figure 4.2 – TRL (Transmission-Reflection-Line) calibration and measurements. First, the Transmission data is captured by measuring the S-parameters of the two SMA-waveguide transitions connected to each other. Then, the measurement is done with the two transitions Open, and finally the transitions are connected with a  $\lambda_0/4$  length line. Later, the material under test (MUT) is inserted in the line for the material measurement. When the data is computed, the reference plane of scattering parameters are shifted to the faces of the sample by applying the TRL calibration algorithm. Then it is possible to use the NRW algorithm to retrieve the dielectric constant of the material.

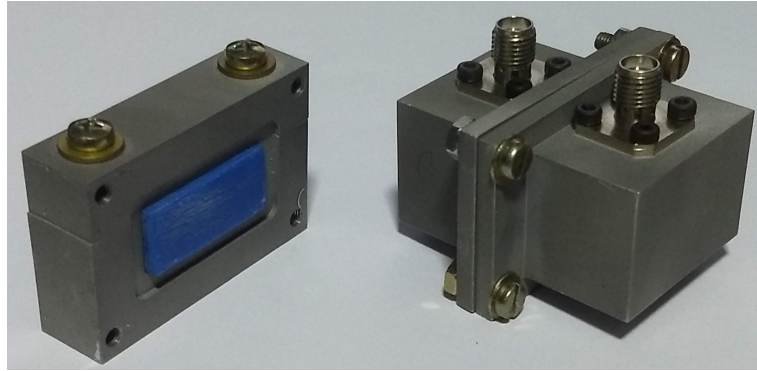


Figure 4.3 – TRL waveguide calibration kit. It consists of two SMA-WR90 waveguide transitions (right) and a line element (left). The "Line" measurement is performed with the line element empty. The same line element is used to hold the sample being measured (MUT - material under test). In this picture, the MUT is the blue block inside the waveguide line on the left.

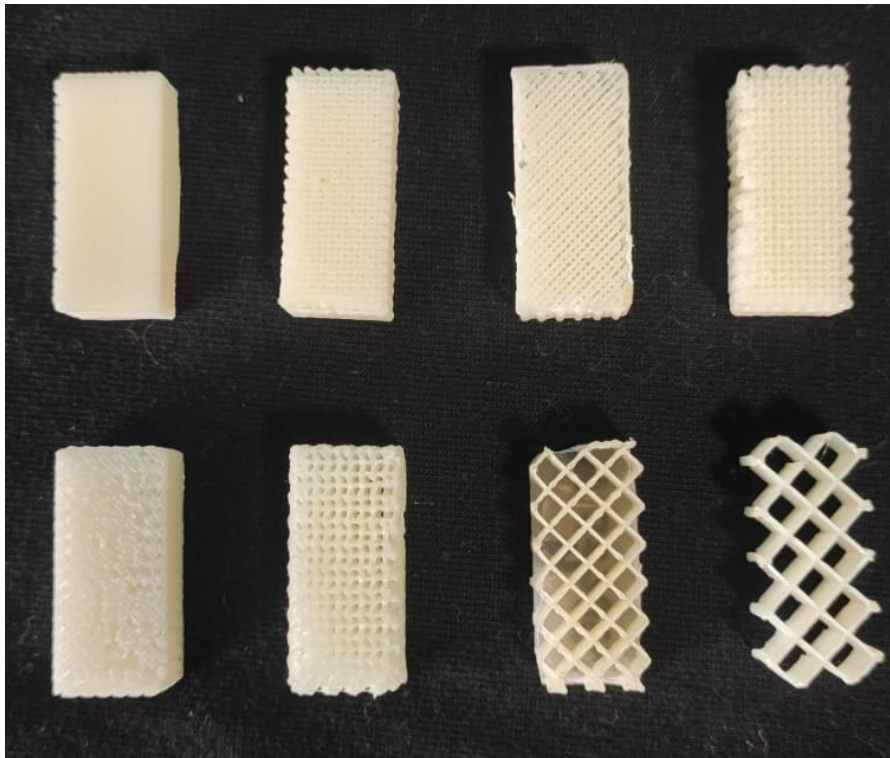


Figure 4.4 – Some of the samples used for material characterization. The material is in natural color, in order to avoid influence of pigmentation differences to the analysis.

#### 4.1.2 NRW retrieval method

After the measurements and calibration, the dielectric constant is retrieved using Nicholson-Ross-Weir (NRW) method, using equations 4.2 to 4.10 [55] [56] [52].

The input parameters to the algorithm are:

- $L$ : Length of the Line (hence the length of the MUT);

- $\lambda_0$ : Wavelength of signal used for measurement;
- $\lambda_c$ : Cutoff wavelength of the waveguide;
- $S_{11}$ ,  $S_{21}$ : S-parameters of the MUT (material under test) measurements with the reference planes at its faces, as in Figure 4.2.

The cutoff wavelength is determined by the waveguide dimensions, and varies for each mode being excited. For the rectangular waveguide with side  $a$  and height  $b$ , the cutoff wavelength for the  $TE_{nm}$  (Transverse Electric) mode is [10]:

$$\lambda_{c_{mn}} = \frac{1}{\sqrt{\left(\frac{n}{2a}\right)^2 + \left(\frac{m}{2b}\right)^2}} \quad (4.1)$$

The  $TE_{10}$  is the dominant mode used for the characterization in this work, so the cutoff wavelength is  $\lambda_{c_{10}} = 45.80$  mm. Its electric fields vectors are depicted in Figure 4.5.

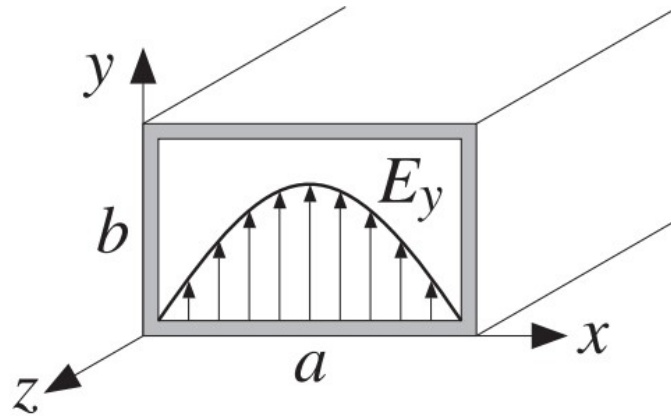


Figure 4.5 – Electric field vectors of the  $TE_{10}$  mode. Source: Reproduced from Orfanidis [10]

Then, it follows the set of equations to find the electric permittivity of the MUT:

$$S_{11} = \frac{\Gamma(1 - T^2)}{1 - \Gamma^2 T^2} \quad (4.2)$$

$$S_{21} = \frac{T(1 - \Gamma^2)}{1 - \Gamma^2 T^2} \quad (4.3)$$

$$\Gamma = X \pm \sqrt{X^2 - 1} \quad (4.4)$$

$$X = \frac{S_{11}^2 - S_{21}^2 + 1}{2S_{11}} \quad (4.5)$$

$$T = \frac{S_{11} + S_{21} - \Gamma}{1 - (S_{11} + S_{21})\Gamma} \quad (4.6)$$

$$\lambda_g = \frac{1}{\sqrt{\frac{1}{\lambda_0^2} - \frac{1}{\lambda_c^2}}} \quad (4.7)$$

$$\frac{1}{\Lambda^2} = - \left( \frac{1}{2\pi L} \ln \left( \frac{1}{T} \right) \right)^2 ; \quad (4.8)$$

$$\mu_r = \lambda_g \frac{1 + \Gamma}{\Lambda(1 - \Gamma)} \quad (4.9)$$

$$\epsilon_r = \frac{\lambda_0^2}{\mu_r} \left( \frac{1}{\lambda_c^2} + \frac{1}{\Lambda^2} \right) \quad (4.10)$$

### 4.1.3 Model fitting

There were measured different samples of the material, varying its infill ratio to get the model for effective dielectric constant depending on this parameter. The measurements of dielectric constant were fit by the power-law model [57], described by the equation:

$$\epsilon_{r_{eff}}^\beta = v_r \epsilon_i^\beta + (1 - v_r) \epsilon_m^\beta, \quad (4.11)$$

where  $\epsilon_i$  is the dielectric constant of the infill material (to be discovered),  $\epsilon_m$  is the dielectric constant of the medium (air),  $v_r$  is the volume ratio of occupied by the infill, and  $\beta$  is a parameter depending on molecular properties of the material.

There exist other models to describe the dielectric constant in relation to the density, such as Maxwell-Garnett (MG), described by Equation 4.12:

$$\epsilon_{r_{eff}} = \epsilon_m \frac{2v_r(\epsilon_i - \epsilon_m) + \epsilon_i + 2\epsilon_m}{2\epsilon_m + \epsilon_i - v_r(\epsilon_i - \epsilon_m)}. \quad (4.12)$$

Or the Lichtenecker's equation, used in [58]:

$$\text{Log}(\epsilon_{r_{eff}}) = \text{Log}(\epsilon_m) + v_r \text{Log}(\epsilon_i/\epsilon_m) \quad (4.13)$$

Figure 4.6 shows the fitting to the models. Similarly to the work presented in [57], the MG model did not produce an accurate fit. The Lichtenecker's equation could have been used, but a better fit by

the minimum mean square error was found for the Power Law, so that model was adopted.

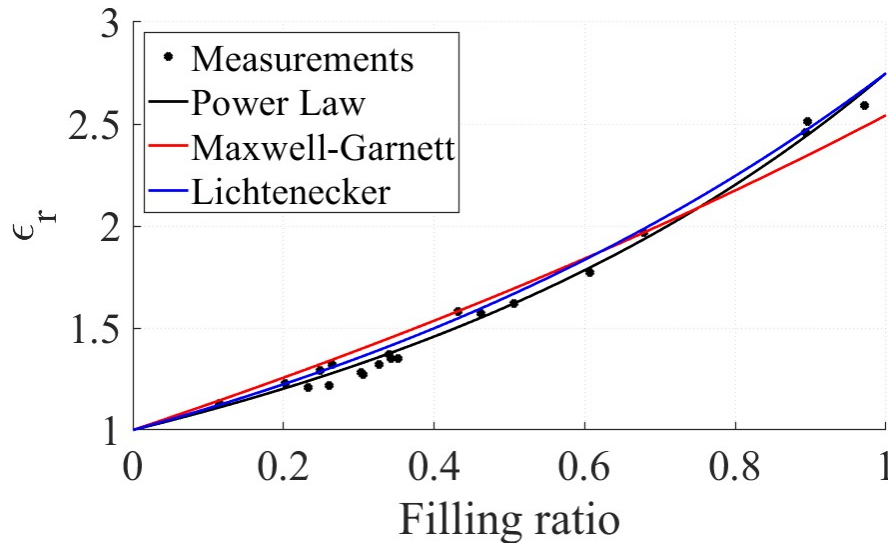


Figure 4.6 – Effective dielectric constant modeling. Several samples were measured, varying its infill ratio to get the model for effective dielectric constant depending on this parameter. The MG model did not produce an accurate fit. The Lichtenecker’s equation could have been used, but a better fit by the minimum mean square error was found for the Power Law, so that model was adopted.

Some authors use the linear approximation of the Power Law model, where  $\beta = 1$ . But by the measurements taken, it was found the best fit with  $\beta = -0.2279$ , and the ABS dielectric constant was found to be  $\epsilon_i = 2.75$ .

As a tool, rearranging Equation 4.11, one may find the necessary filling ratio to achieve the desired dielectric constant by Equation 4.14:

$$v_r = \frac{\epsilon_{r_{eff}}^\beta - \epsilon_m^\beta}{\epsilon_i^\beta - \epsilon_m^\beta} \quad (4.14)$$

#### 4.1.4 Alternative materials

Other materials could have been studied to construct the lens. Due to expression in Equation 2.21, the core of the torus must have  $\epsilon_r = 2$ , therefore using a material with that nominal value of dielectric constant would imply a 100% filling ratio at the core, hence, it would increase the dynamic range of the infill ratio for the layers.

According to the literature, the pure Polypropylene (PP) has a nominal dielectric constant around 2.1 [59] [60], and some manufacturers report 2.2 [61]. The Braskem company produces a PP filament for FDM that could be used for this purpose [62], but since the datasheet does not provide information about electromagnetic properties, or its exact composition, it would still be necessary to perform the characterization, even because after the material is fused, the properties can be slightly changed due to thermal degradation of the additives that might be on the filament composition.

## 4.2 UNIT CELL

The material can be printed using several infill geometries. The shape of the unit cell may cause variations in the wave scattering, depending on the polarization and incidence direction. A study on the influence of the shape of unity cell on the propagation features is presented in [63].

Figure 4.7 depicts 4 styles of unit cells, that would be replicated along the printed structure. The variation of the parameters of the holes provides the variations in the infill ratio, and consequently in the dielectric constant.

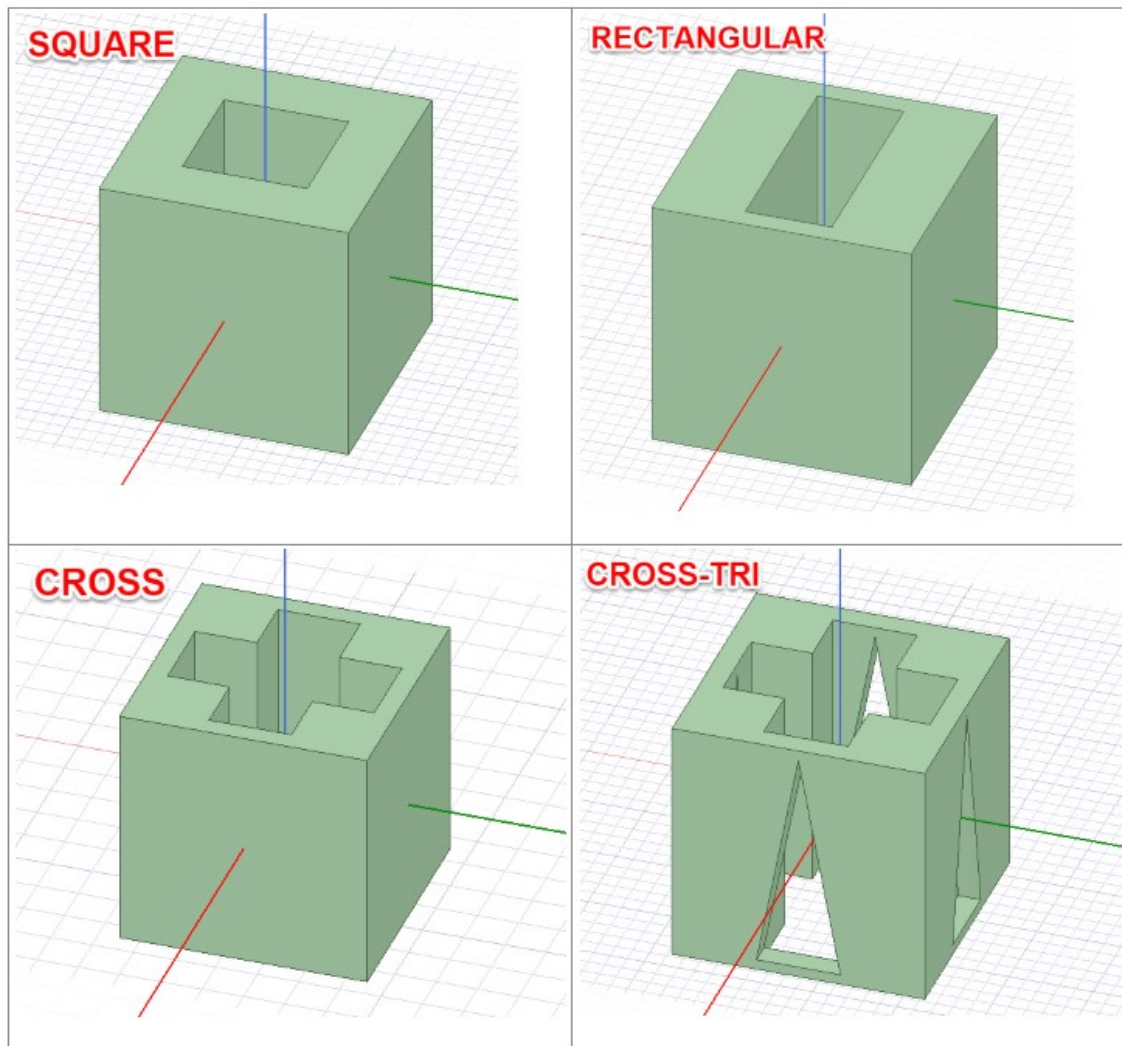


Figure 4.7 – Different styles of unit cell based on fixed length. With this strategy, the infill ratio is controlled by the size of the holes, which is limited by the minimum wall thickness and discretized by the nozzle diameter.

It is desirable that the unit cell length be as small as possible in comparison to the wavelength (generally at the order of  $\lambda/10$  is a conservative approach), this way the cell itself can be used as lumped element, *i.e.* there will be no significant changes on the phase of the fields along the cell [40]. Besides the electromagnetic behavior, it is evaluated the feasibility of 3D printing process for these hole types, with a nozzle with 0.25 mm of diameter.



For the rectangular holes depicted in Figure 4.8, the length of the unit cell is fixed, and the infill density is related to the thickness of the walls according to Equation 4.15. With this strategy, the infill density is discretized by the diameter of the nozzle, and it is not always possible to reach the desirable dielectric constant with the necessary accuracy. Indeed, as it is depicted by Figure 4.9, with the parameters used in this work, it would not be possible to print a lens with 10 different layers with any of the four models presented in Figure 4.7.

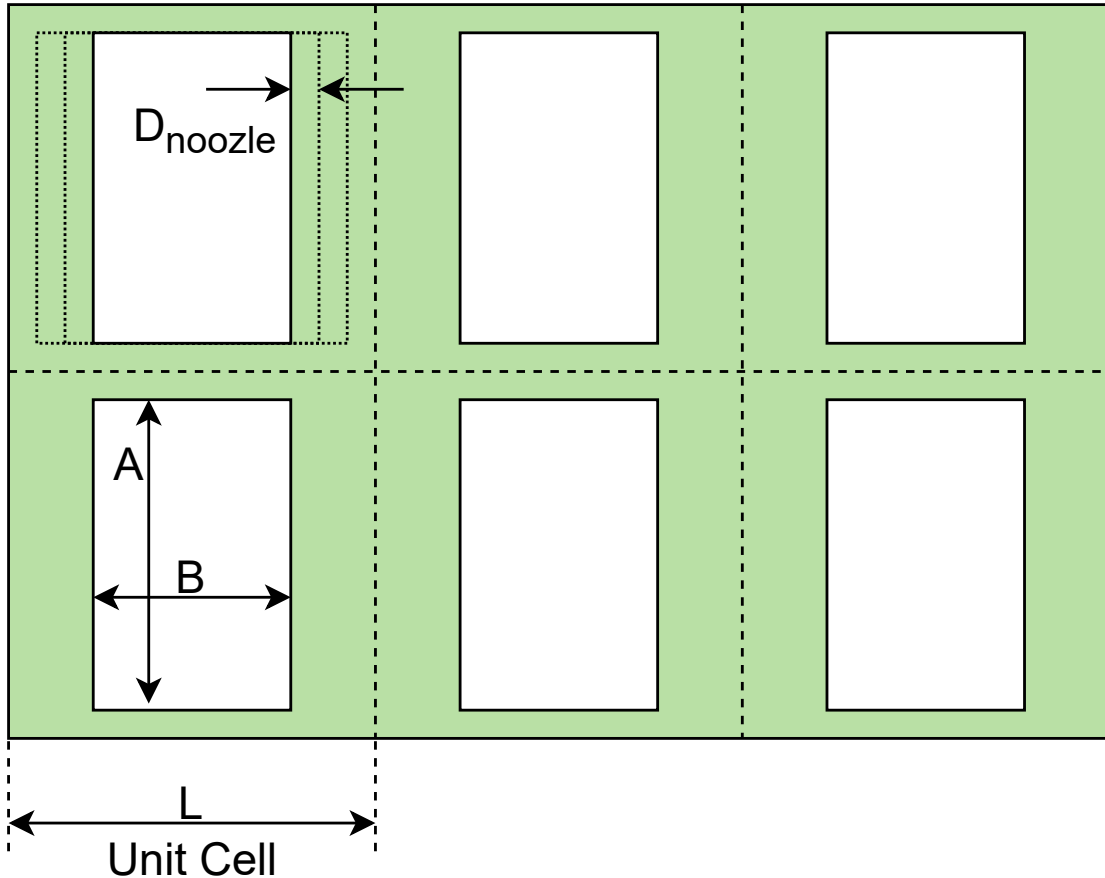


Figure 4.8 – Rectangular unit cell parameters. The length of the unity cell is fixed, and the infill density is related to the hole size according to Equation 4.15.

$$v_{f_{RECT}} = 1 - \frac{AB}{L^2}, \quad (4.15)$$

where

$$A = mD_{nozzle}$$

and

$$B = nD_{nozzle},$$

with  $m, n$  positive integers.

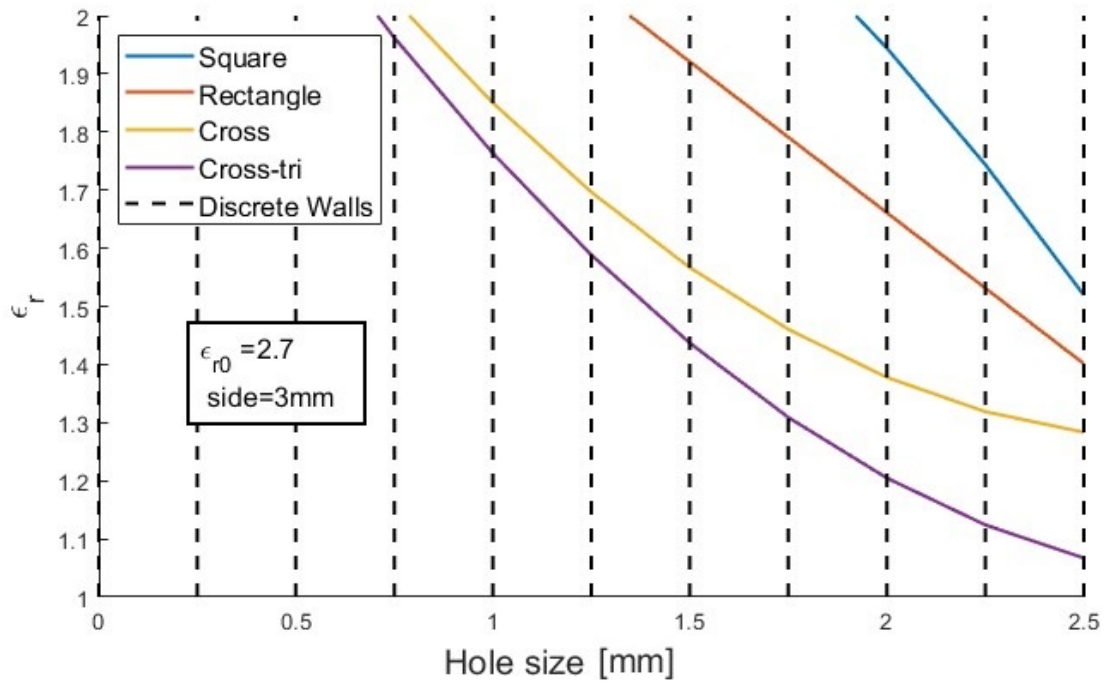


Figure 4.9 – Unit cells with discrete walls. The fixed cell size, combined with the limited nozzle diameter (0.25 mm) creates discrete values for the dielectric constant.

A different approach applies a variable cell size, such as in the *woodpile* presented in Figure 4.10. With this strategy, the possible densities are continuous, because  $L$  can assume any value inside  $w \leq L \leq \lambda/10$ . Indeed,  $w$  can be fixed to  $w = D_{nozzle}$ , letting the density be controlled only by  $L$ , as in Equation 4.16.

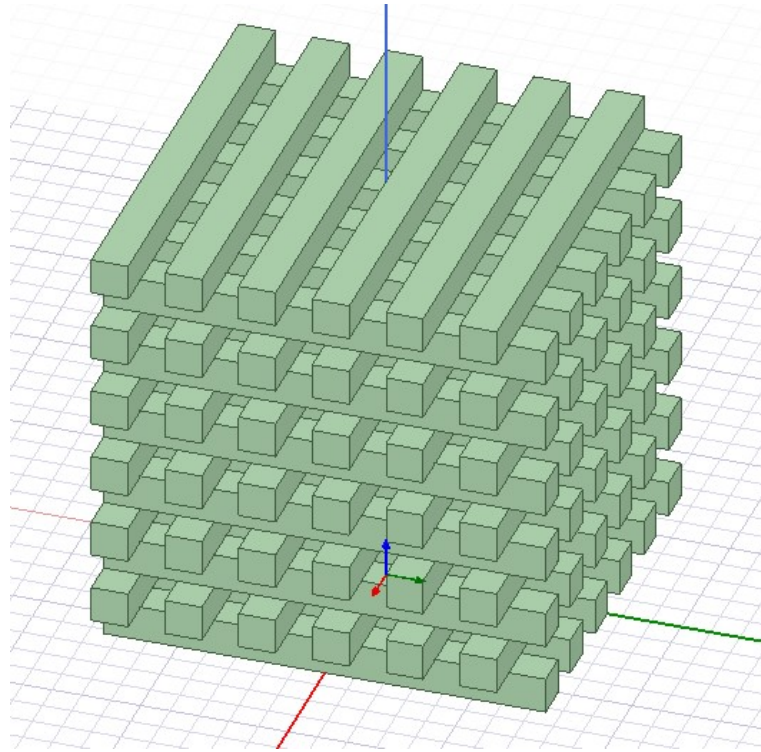


Figure 4.10 – Woodpile structure. This is also called "grid" in 3D printing softwares. It consists of aligned and stacked rods.

In this configuration, the unit cell is modeled as the delimited region in Figure 4.11, providing an one dimensional infill ratio model.

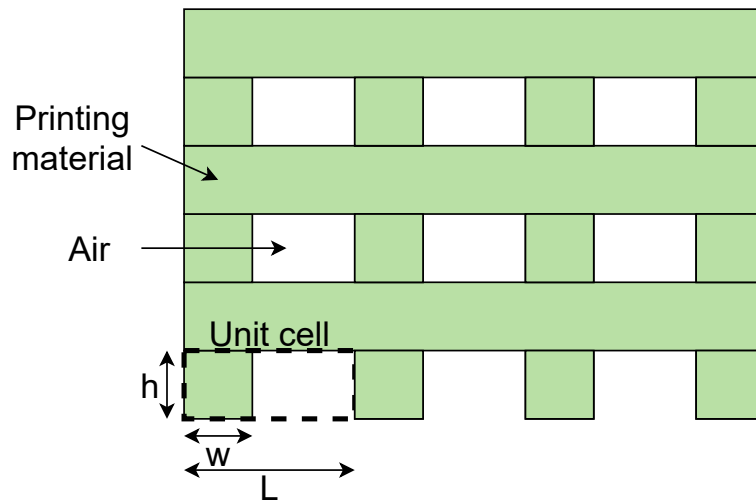


Figure 4.11 – Front view of the woodpile unit cell and its parameters. With this strategy the possible densities are continuous, because  $L$  can assume any value above the diameter of the nozzle.

$$v_{f_{WP}} = \frac{w}{L} \quad (4.16)$$

For the parameters used in this work, the woodpile approach is way more convenient than a fixed length cell, because any value of dielectric constant can be achieved, and the larger cell size needed

to construct the lens (2.45 mm) is smaller than  $\lambda_0/10$  (3.00 mm), as shown in Figure 4.12.

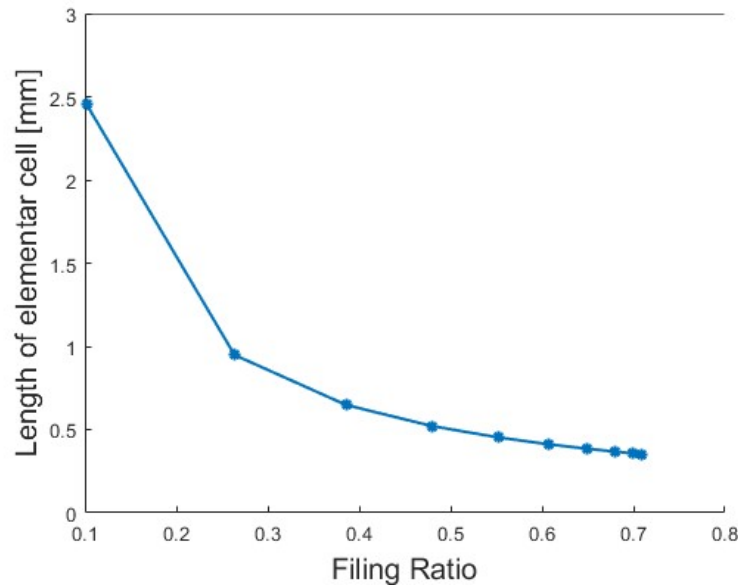


Figure 4.12 – Woodpile unit cell lengths needed for the construction of the 10 layers of the lens, using the ABS with  $\epsilon_r = 2.75$ . The larger cell size needed (2.45 mm) is smaller than  $\lambda_0/10$  (3.00 mm), which represents a structure that will not cause considerable distortions to the wave.

In [64] it is found that the effective dielectric constant for woodpile structure is non-dispersive (frequency independent) for  $L < 0.49\lambda_0$ . Using this condition only, the maximum frequency to which the model would fit would be 59.91 GHz. Using the conservative approach ( $L < \lambda_0/10$ ), the maximum frequency admitted would be 12.27 GHz. For the maximum frequency of the Ku communication band (14.5 GHz), the maximum cell size would be  $\lambda_0/8.43$ , which is in reasonable balance between the acceptable and the most conservative limits.

#### 4.2.1 Material deposition

Equations 4.16 and 4.15 approximate the deposited filament by rectangular rods, but during the material deposition, the nozzle depicted in Figure 4.13 is not able to fill the whole volume of the rectangular profile. Indeed the printed profile is approximated by an ellipsoid, as shown in Figure 4.14.

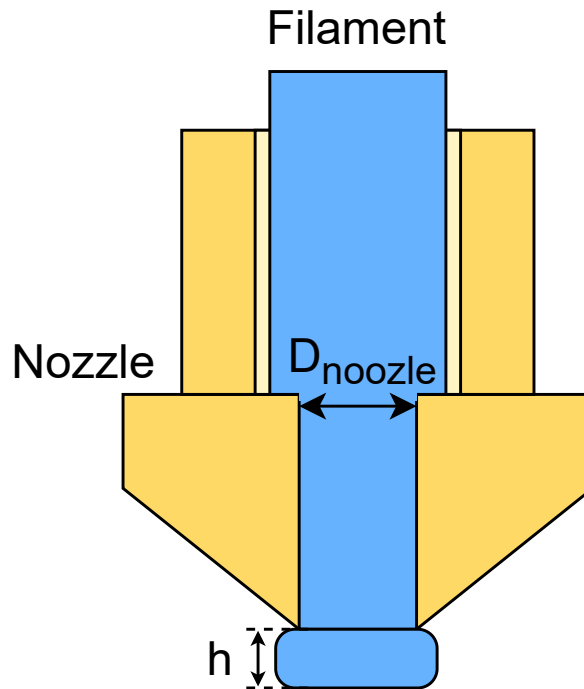


Figure 4.13 – Representation of the nozzle extruding the filament. The deposited material is flattened against the base to be properly merged with the previous layer (immediately below). This creates a trace slightly larger than the nozzle diameter, but that is further compensated by the pressure of the next trace on the immediate side, as presented in Figure 4.14.

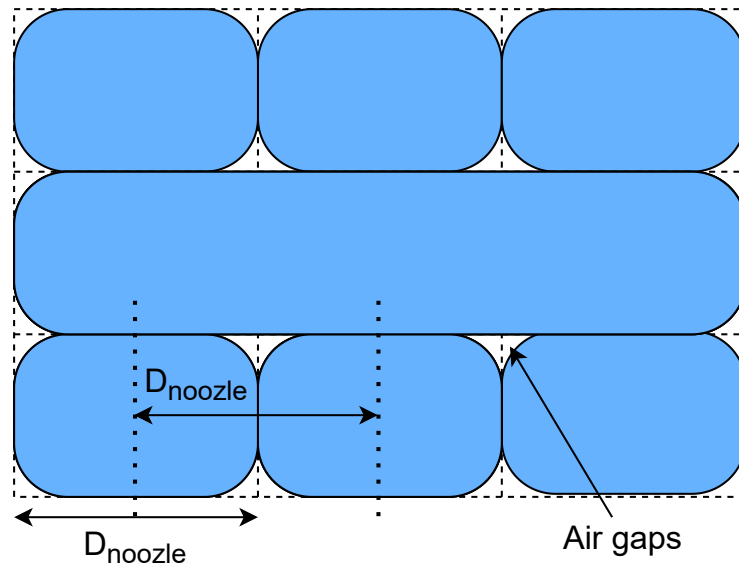


Figure 4.14 – Printed layers for a 100% nominal infill ratio. The nozzle is not able to fill the whole volume of the rectangular profile. Indeed the printed profile is approximated by an ellipsoid. Therefore, the real density obtained is slightly lower than nominal because of the air filling the gaps between elliptic rods.

Zhang [15] performed some studies about this issue and some electrical characteristics depending on the parameters of construction. The microscopy from a sample used in his work is reproduced in

Figure 4.15.

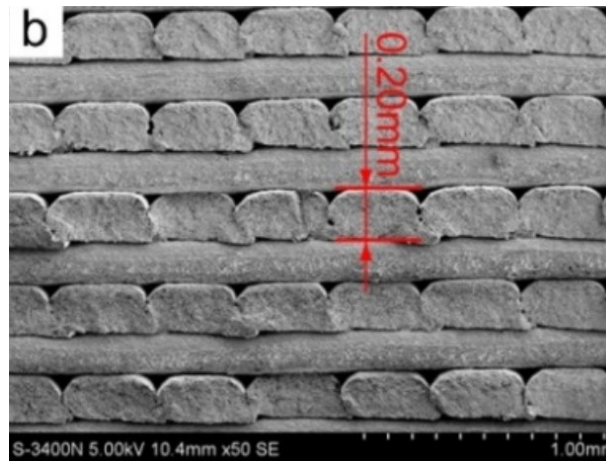


Figure 4.15 – Microscopy of a 3D-printed sample. Source: Reproduced from Zhang’s article [15]. It is possible to see the gaps between the traces and the flattening of the material, mentioned in Figure 4.13.

Therefore, the real density obtained is slightly less than nominal because of the air filling the gaps between elliptic rods. Several measurements were performed, and the density correction factor from nominal is found to be 88.59%. The graph of those measurements is shown in Figure 4.16. The proportion value encountered in this work is close to the one found by Zhang in [15] (89.1%).

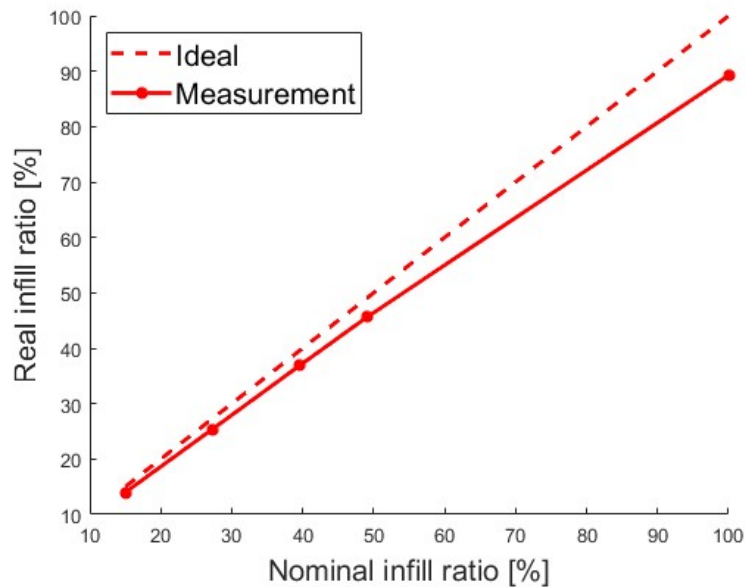


Figure 4.16 – Infill differences for the woodpile printing pattern, using ABS. The density achieved for printed materials is 88.59% of the nominal density predicted.

$$v_{f_{WP,r}} = 0.8859 v_{f_{WP,n}} = 0.8859 \frac{w}{L} \quad (4.17)$$

### 4.2.2 Parabolic holes – a potentially alternative method

When applying the hole pattern described in Figures 1.7 and 1.8 on spherical structures, the parabolic profile is rotated around its own axis to create the hole, creating a circular profile that can be done with FDM 3D printing without major problems. But speaking about a toroidal lens, the parabolic profile need to be rotated around the central axis, creating suspended horizontal slabs, as shown in Figure 4.18, and those structures would fall during the material deposition.

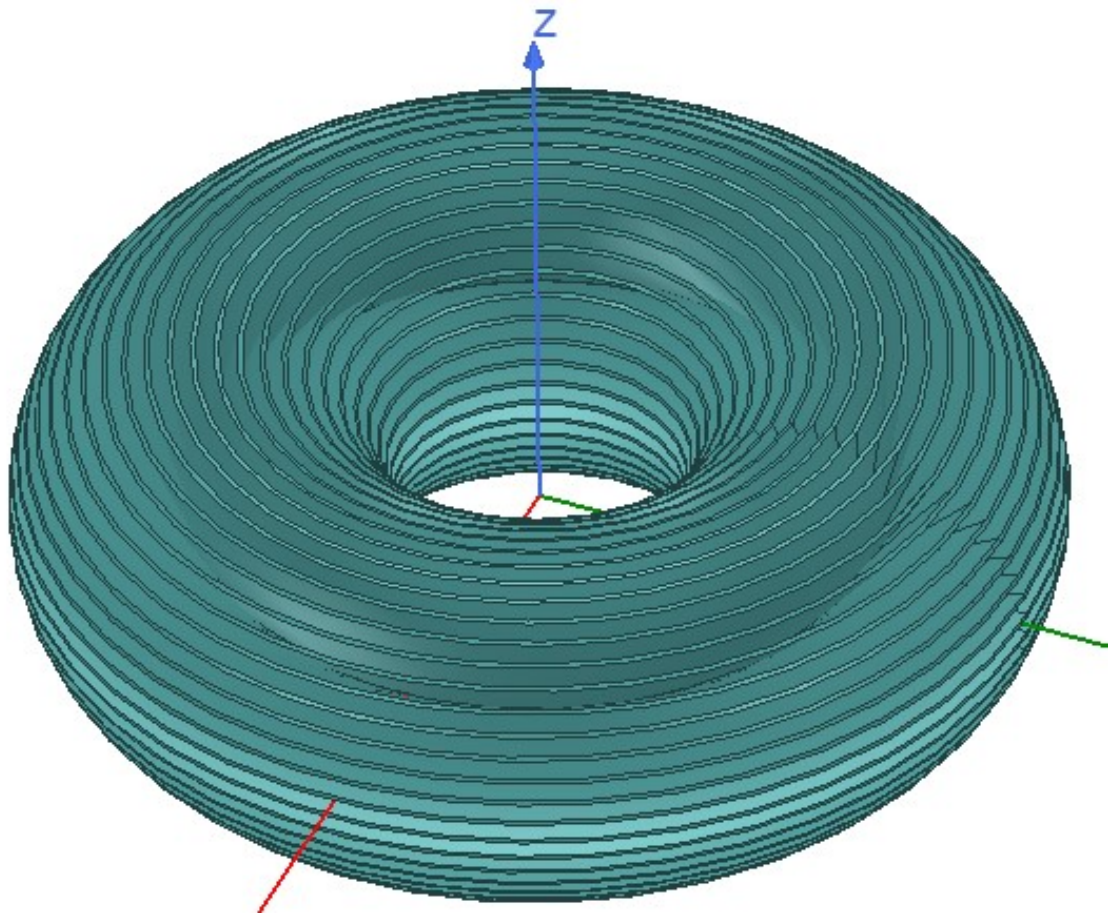


Figure 4.17 – Toroidal lens with continuous gradient of refractive index.

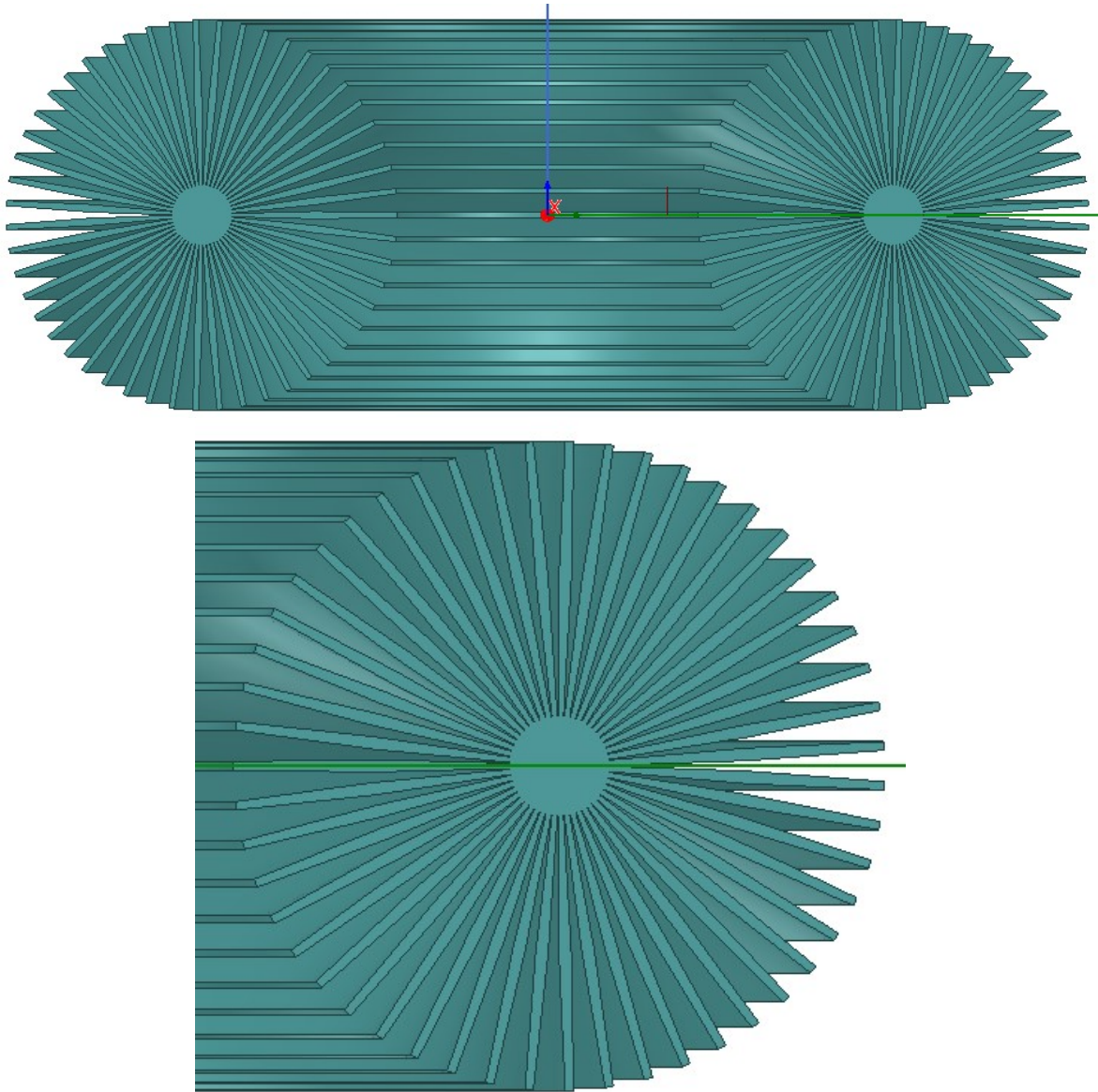


Figure 4.18 – Cross section of the toroidal lens with parabolic profile cuts. The rotation of the profile around the central axis implies on suspended slabs that cannot be printed without a support. The FDM 3D printing with soluble material could be a solution to this problem [16].

Therefore, to use this pattern, the lens must be printed using a technique that permits such suspended structures. The FDM 3D printing with soluble material could be a solution to this problem [16].

### 4.3 LENS PROTOTYPE

This section presents the methods for printing the lens prototype. It covers the validation of the process itself, the choose of lens parameters, the feeding antenna, and the test setup.



### 4.3.1 Validation of the 3D-Printed structure

Before printing the whole lens, it was performed a validation of the manufacturing technique by printing a five layer slice in the same orientation of the prototype. The part on the printer is shown in Figure 4.19.

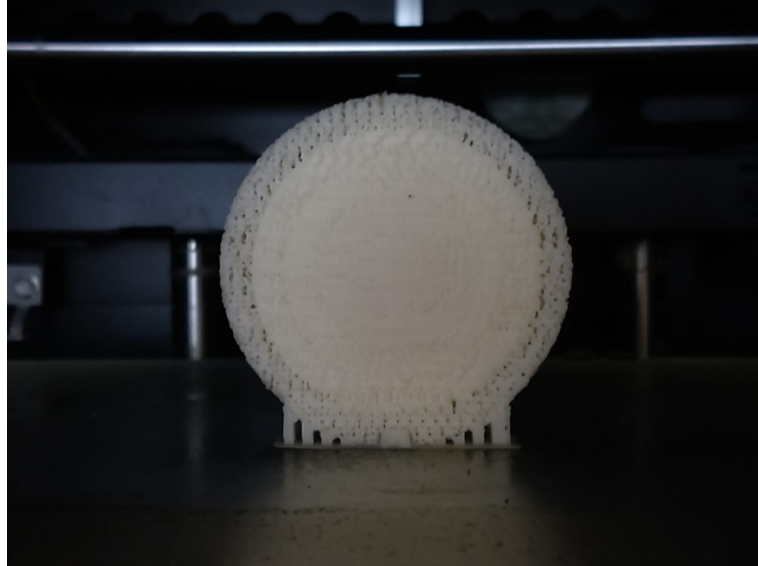


Figure 4.19 – Printed slice of a five layer torus. It was used a support for angles higher than  $40^\circ$ . This was done as a validation of the manufacturing technique.

It is possible to see in Figure 4.20 that the layer separation was maintained, and the circular shape of the slice did not suffer distortion. Also, the variation of infill ratio can be verified by visual inspection.

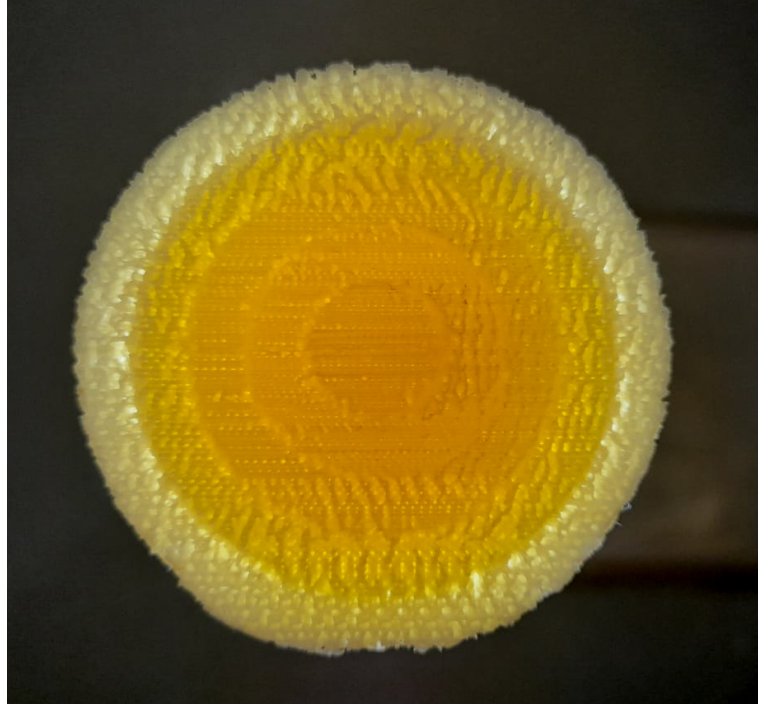


Figure 4.20 – Slice of a stratified torus with 5 layers. It is possible to see that the layer separation was maintained, and the circular shape of the slice did not suffer distortion. Also, the variation of infill ratio can be verified by visual inspection of the sample against the light.

One defect that could impact the lens performance is the air gap between the shells. Ideally, it would be 0%. It is shown in studies [26] that those gaps can deteriorate the directivity of the lens. This study shows a decrease of 25 dB in directivity when the shells have 3% of air gap. However, this issue is eliminated when an additive construction method – such as 3D printing – is employed, because it is not necessary to assembly multiple parts with possible surface irregularities. All the deposited material will inevitably be merged with the rest of the structure.

### 4.3.2 Lens

The printed prototype is a 10 layer torus with Luneburg distribution, using the dielectric constants presented in Table 4.1.

Layer	1	2	3	4	5	6	7	8	9	10
$\epsilon_r$	2.00	1.98	1.94	1.88	1.80	1.70	1.58	1.44	1.28	1.10
$r_{\text{uniform}}^1$	0.10	0.20	0.30	0.40	0.50	0.60	0.70	0.80	0.90	1.00
Filling ratio [%] <sup>2</sup>	70.86	69.91	67.97	64.96	60.77	55.19	47.93	38.56	26.37	10.19
Adjusted filling ratio [%] <sup>3</sup>	80.00	78.92	76.72	73.33	68.59	62.29	54.11	43.53	29.77	11.50

Table 4.1 –  $\epsilon_r$  distribution for 10 layer centered torus. Layer 1 is the core, and layer 10 contains the external boundary.

The parameters of construction are:  $R_1 = 35.5$  mm and  $R_2 = 57.5$  mm. These were chosen based on the maximum dimension possible to print the torus in the horizontal orientation and the space required to place an open-ended WR90 waveguide antenna.

The 3D model for the prototype was processed by the software Ultimaker Cura v4.7.1 [65]. It transforms the 3D model into G-code [66] command lines to be interpreted by the 3D printer. The parameters set to build the model are presented in Table 4.2.

Infill pattern	Grid <sup>4</sup>
Base temperature	100° C
Noozle temperature	240° C
Layer height	0.10 mm
Extrusion thickness	0.25 mm
Angle for support generation	40°
Printing speed	60 mm/s

Table 4.2 – Parameters for the 3D printer used for manufacture the lens.

The time needed to print the whole lens with the specified parameters is around 4 days. Considering some issues out of the research’s control that may occur, such as a blackout, nozzle clogging, system failure, or machine overheating, there would be some serious risks to the time scheduling of the research with the approach of printing the toroid in its totality at once.

Thus, it was decided to print a half lens, considering only the 180° aperture for radiation. Since a directional antenna is being used, this will not produce a significant impact on the results. The printed lens is shown in Figure 4.21. An auxiliary section was attached to the lens, with the objective to create an interface for the assembling of the test setup, as will be explained with more details in Section 4.5.

In Figure 4.22 it is possible to see some imperfections of the printing, like some small stains on the right side and some residual plastic attached to the lens. But the size of those imperfections is so small in comparison to the wavelength, that it does not affect the overall performance of the lens, as verified by the measurement results in Chapter 5.

<sup>1</sup>Normalized radius  $r/R_1$ .

<sup>2</sup>Real/expected filling ratio, using power law model in Equation 4.11

<sup>3</sup>Filling ratio used on the print to compensate the density reduction, as explained in Section 4.2.1. The practical filling ratio is 88.59% of the nominal set on the printing parameters.

<sup>4</sup>Same as *woodpile*

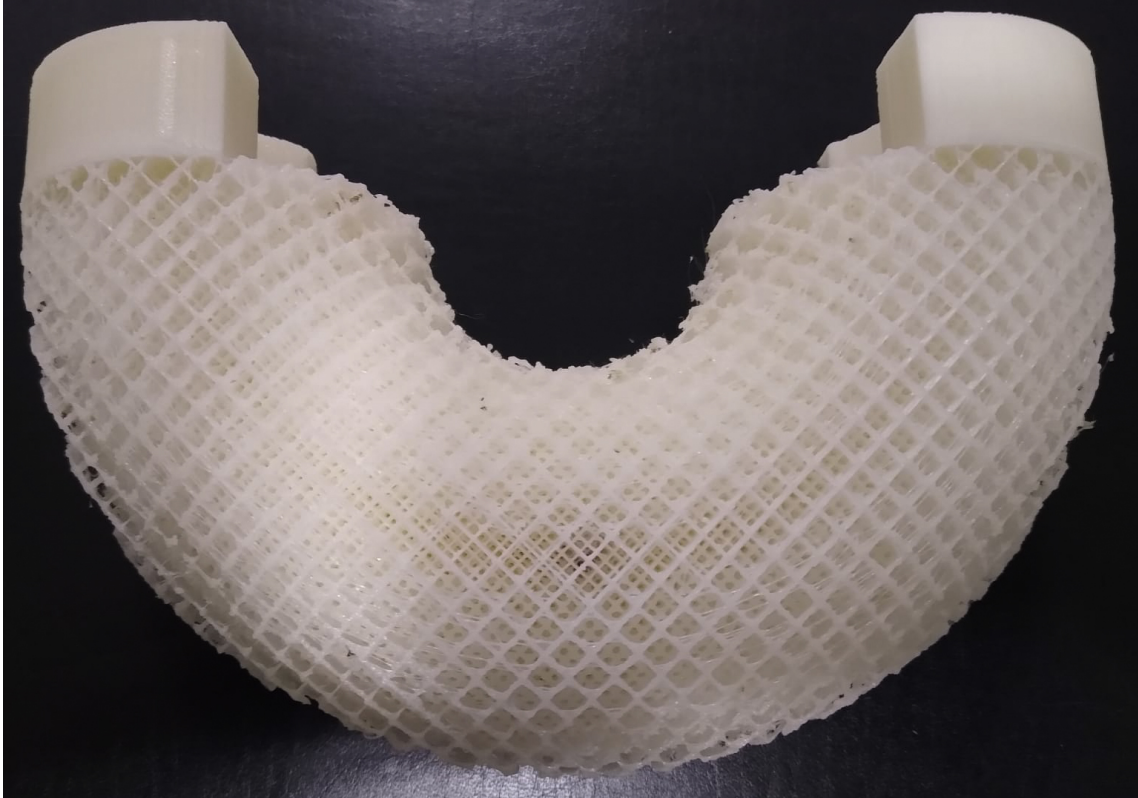


Figure 4.21 – Printed lens. The lens have  $R_1 = 35.5$  mm and  $R_2 = 57.5$  mm. It was decided to print a half lens, considering only the  $180^\circ$  aperture for radiation. Since a directional antenna is being used. It is possible to see the grid pattern on the printing, with different infill ratio on the layers below.



Figure 4.22 – Side view of the printed lens. The small stains and residual plastic attached to the lens does not affect the overall performance of the lens, as verified by the measurement results in Chapter 5.

## 4.4 ANTENNA

Due to the simplicity, ease of fabrication, robustness, and physical fitting to the structure, it was chosen an open-ended WR90 waveguide antenna to perform the far-field measurement experiments.

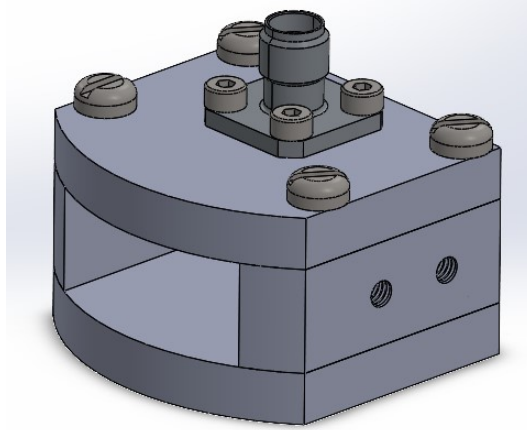


Figure 4.23 – WR90 open-ended waveguide antenna used to perform the far-field measurement experiments. The antenna has four tapered holes enable the assembly on the test fixture. In order to fit the antenna to the inner face of the torus, the front face of the waveguide was cut in a 25 mm radius.

The waveguide is fed through a straight exciter inside, which is connected to as SMA connector.

The antenna has four tapered holes, two on each side, to enable the assembling on the test fixture, which is presented further.

In order to fit the antenna to the inner face of the torus, as in Figure 4.28 and 4.30, the front face of the waveguide was cut in a 25 mm radius, resulting in a conformal antenna [30]. The drawing of the antenna is presented in Appendix B.

It was evaluated the influence of the radial cut to the performance of the antenna. There is a loss of 1 dB in the maximum directivity, as shown in Figures 4.24 and 4.25. However the overall performance still fulfill the expectations. When computing the results of the lens set, those characteristics must be considered.

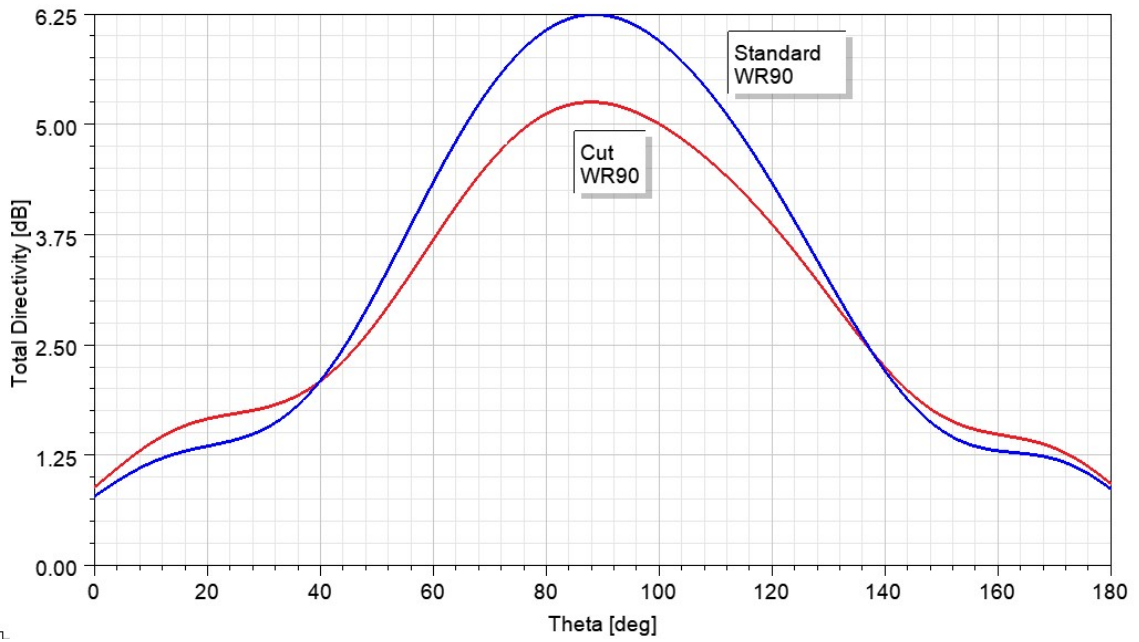


Figure 4.24 – Total directivity in the electric plane. There is a loss of 1 dB in the maximum directivity comparing to the standard waveguide.

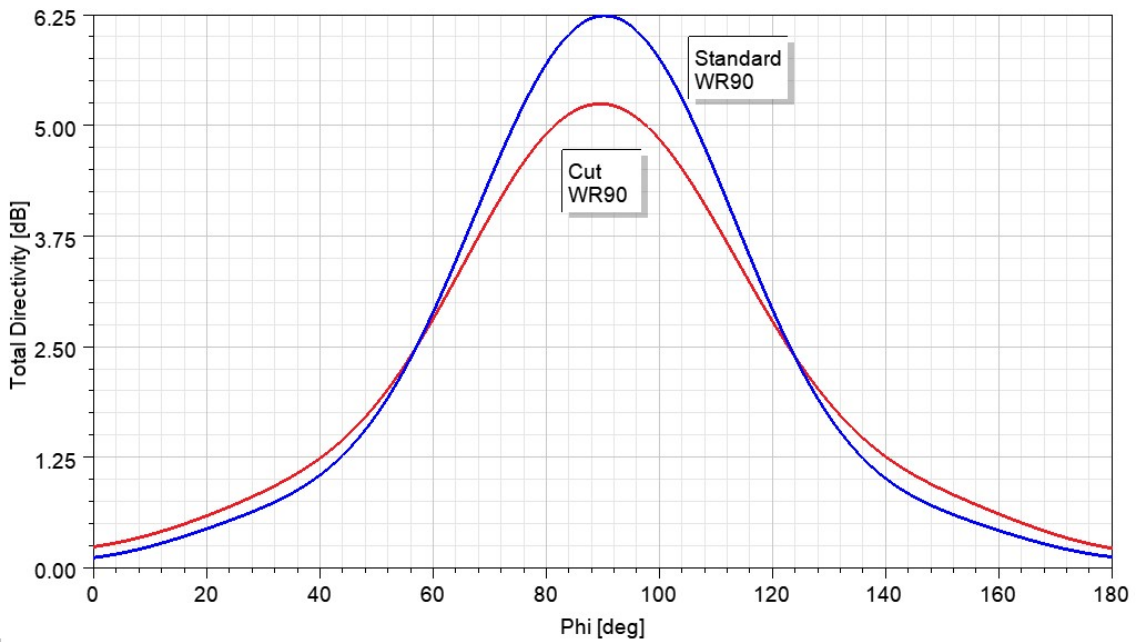


Figure 4.25 – Total directivity in the magnetic plane. There is a loss of 1 dB in the maximum directivity comparing to the standard waveguide.

The parts of the antenna were machined in aluminium, and assembled as shown in Figure 4.26.



Figure 4.26 – WR90 open-ended waveguide antenna, fabricated in aluminium.

#### 4.4.1 Potential alternatives

The cut could be avoided by shifting the focus of the lens to the outside, with a small distance from the outer boundary, as it is done in [67]. This would require an adequacy of the effective permittivity distribution across the lens structure. This feature was not implemented because the objective of this work is to prove the concept of the toroidal Luneburg lens using the standard distribution from Equation 2.21, discretized according to Equation 2.22. However, the shifting of the focus can be explored in future works. To do so, it is necessary to evaluate the relation between the focus and the curvature of the torus caused by the major radius.

Another option is to use different types of conformal antennas, such as the ones mentioned in Section 1.3.1.

## 4.5 TEST FIXTURE

It was designed a structure to assembly the antenna and the lens together, also allowing the steering of the structure during the measurements. The structure allows the positioning of an open waveguide antenna at the predefined tilt angles from  $0^\circ$  to  $90^\circ$  in steps of  $10^\circ$ .

The test fixture is 3D printed using ABS, and contains holes to fix the antenna with M3x8 screws. The base is shaped to fit the surface of the lens. It is designed to be attached to the flange of the steering mechanism, represented by the brown part for reference.

A 20 mm cylinder (shown in Figure 4.31) was attached to the lens structure in the same 3D printing process, hence it is part of the print, merged with the lens. The objective of this section of

the part is to create a threaded interface for the six M5x25 plastic screws attaching the lens to the fixture. With this strategy, the auxiliary equipment is retained outside the analyzed 180° radiating sector, and the absence of metal parts on the fixture ensures that the incident wave will not create secondary sources.

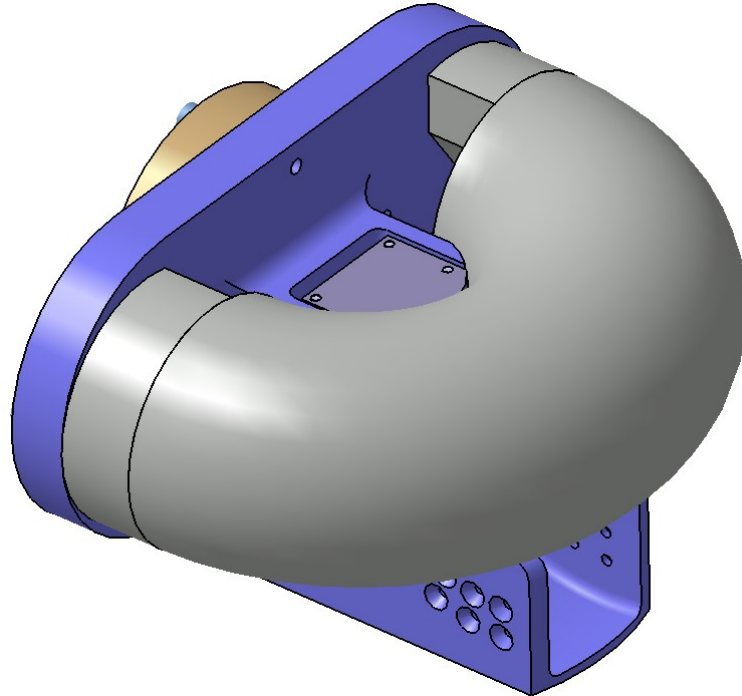


Figure 4.27 – Perspective view of the lens fixed on the test fixture. The base is shaped to fit the surface of the lens. It is designed to be attached to the flange of the steering mechanism, represented by the brown part for reference.

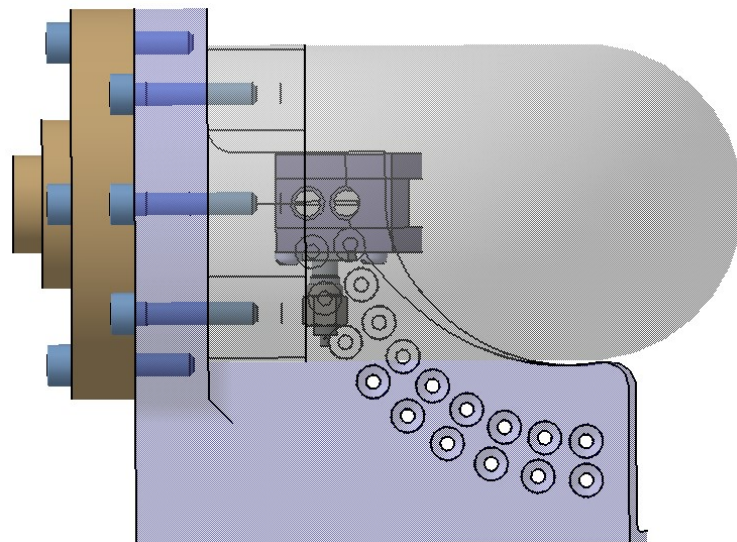


Figure 4.28 – Side view of the lens assembly. The base contains holes to fix the antenna with M3x8 screws, allowing the positioning of the antenna at the predefined tilt angles from 0° to 90° in steps of 10°. The male SMA connector is shown attached to the antenna to verify the space for the RF cable.



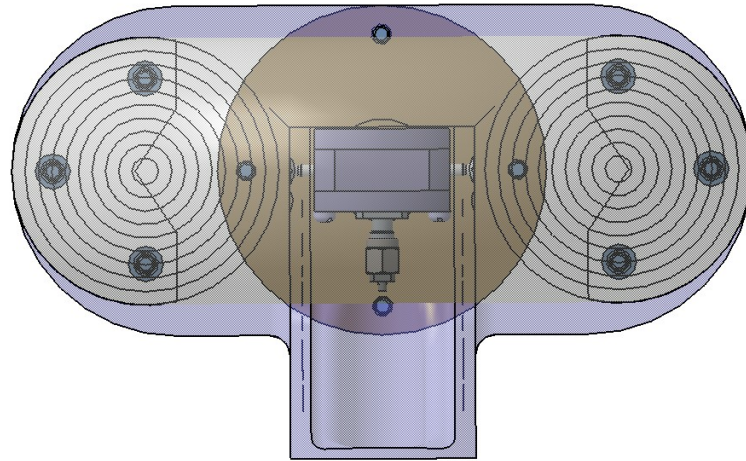


Figure 4.29 – Front view of the lens assembly.

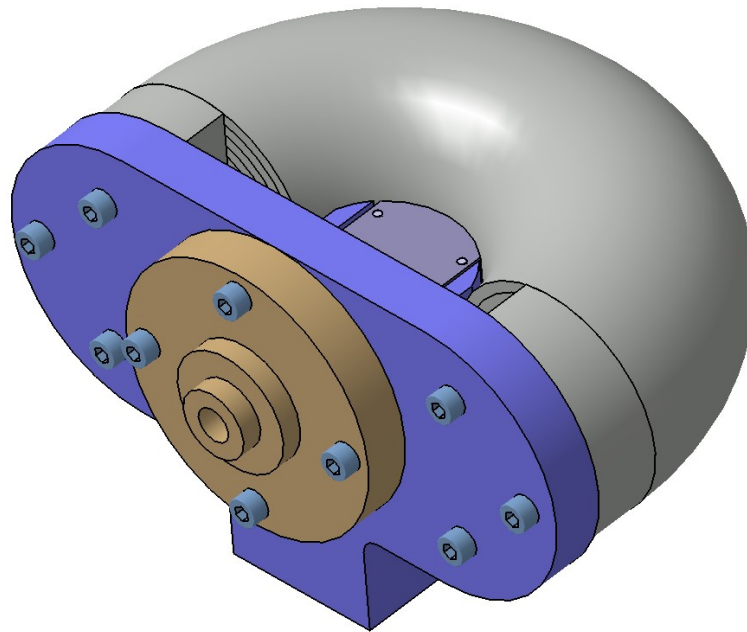


Figure 4.30 – Perspective view from the back of the test fixture. The flange is the interface with the steering equipment.

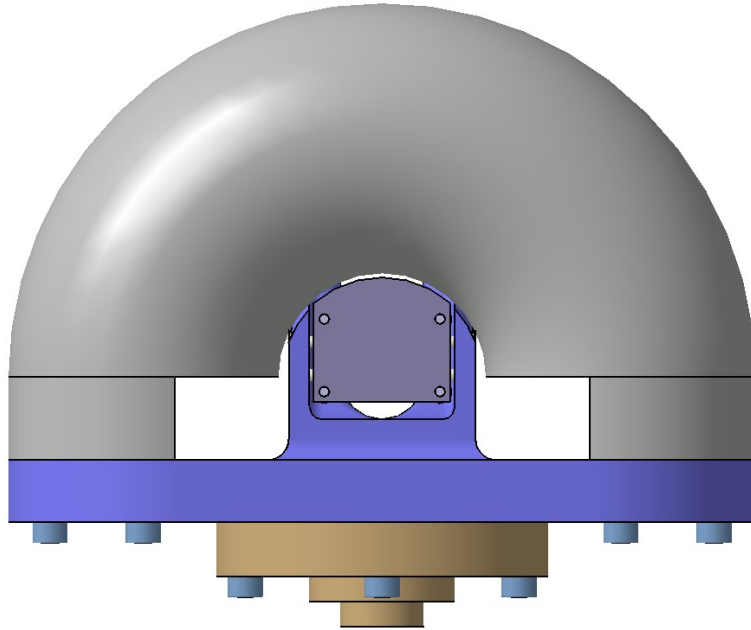


Figure 4.31 – Top view of the lens assembly. A 20 mm cylinder was attached to the lens structure in the same 3D printing process. The objective of this section of the part is to create a threaded interface for the six M5x25 plastic screws attaching the lens to the fixture. With this strategy, the 180° aperture is not affected by the auxiliary equipment.

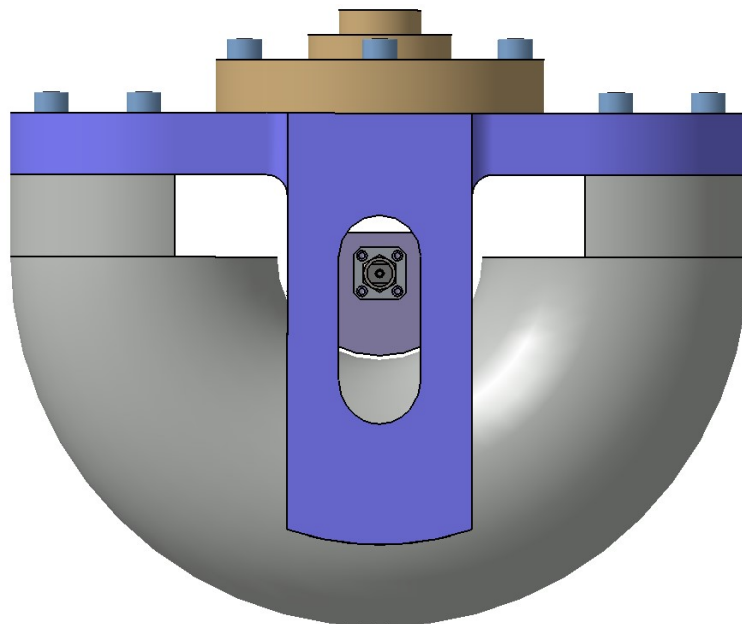


Figure 4.32 – Bottom view of the lens assembly. There is an oblong cut on the support to create a free path for the cable connection.

## 4.6 TEST SETUP

To perform the angular movements for the radiation pattern measurement, it is used a steering arm, consisting of a telescopic structure with 3 axis, already available on the Telecommunications Laboratory of the University of Brasilia. Figure 4.33 shows the equipment.



Figure 4.33 – Steering equipment. It consists of a telescopic structure with 3 axis, already available on the Telecommunications Laboratory of the University of Brasilia.

The test setup is shown in Figure 4.34, and explained in Figure 4.35. The equipment set consists of two steering mechanisms. One with the antenna under test – connected to a spectrum analyzer – , and the other with the reference antenna – connected to a signal generator.



Figure 4.34 – Photography of the far-field measurement setup.

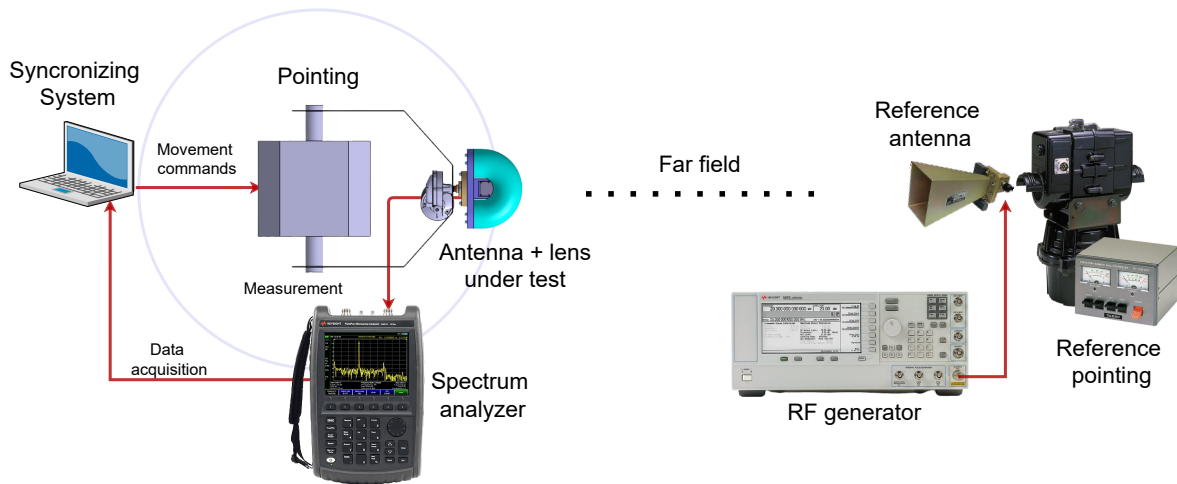


Figure 4.35 – Measurement setup. The equipment set consists of two steering mechanisms. One with the antenna under test – connected to a spectrum analyzer – , and the other with the reference antenna – connected to a signal generator. The measurement process is controlled by a python script running on the *Synchronizing System*.

A python script was written to control the steering angle of the antenna under test and for the signal acquisition from the spectrum analyzer. The same script assigns the power reception measurements to the corresponding pointing angles. Further it saves a CSV (Comma-Separated Values) file with all extracted data for post-processing.

An application was designed using PyQt5 [68]. It creates the Human-Machine Interface (HMI) presented in Figure 4.36 and triggers the functions on the main Python script to perform the measurements routine.

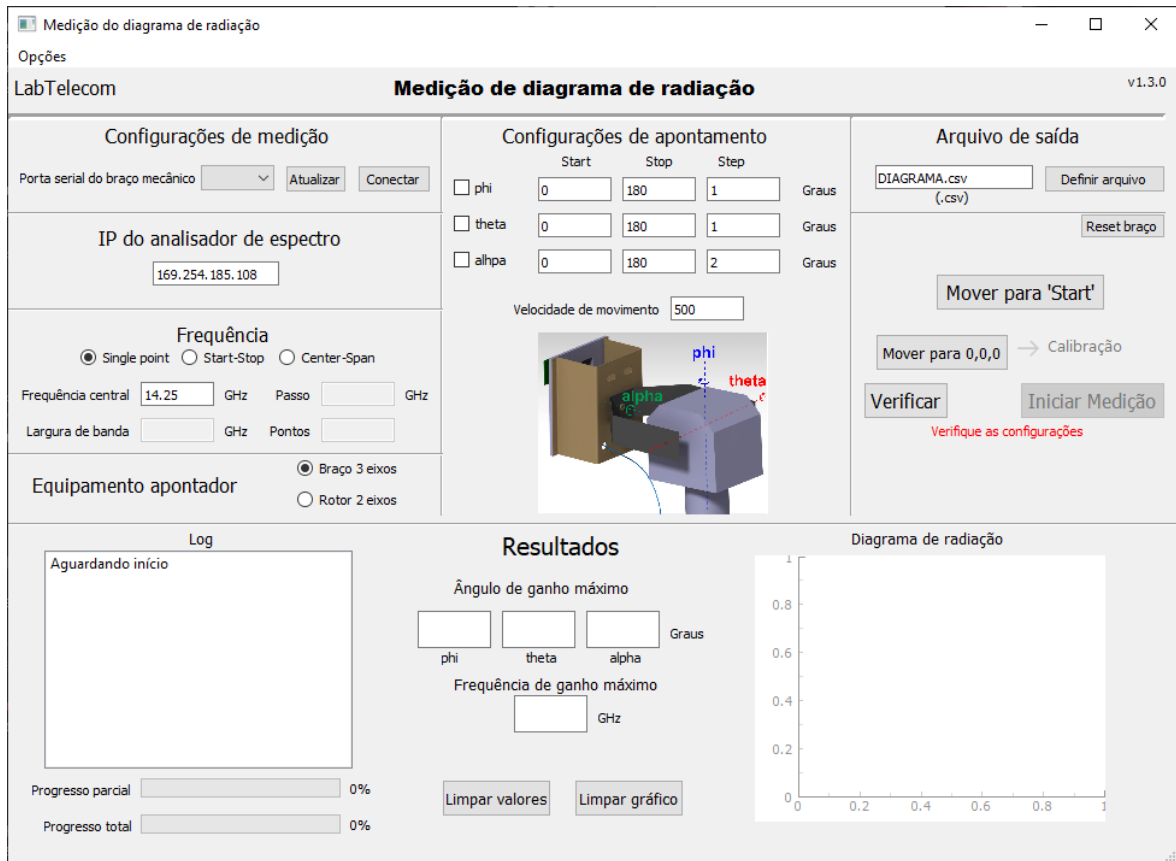


Figure 4.36 – Human-Machine Interface (HMI) of the application designed for the test automation. It provides a control panel, with configuration fields and information about the test campaign. The back-end software triggers the functions on the main Python script to perform the measurements routine.

Then, it is possible to measure the signal intensity either in transmission or reception for any given elevation and azimuth angles. This is used to construct the radiation pattern of the lens+antenna setup.

# 5 MEASUREMENTS

The following graphs present the radiation pattern plots for the printed lens, after measurements on the far-field.

The elevation angle represents the angulation of the antenna pointing direction with reference to the horizontal plane, according to Figure 5.1.

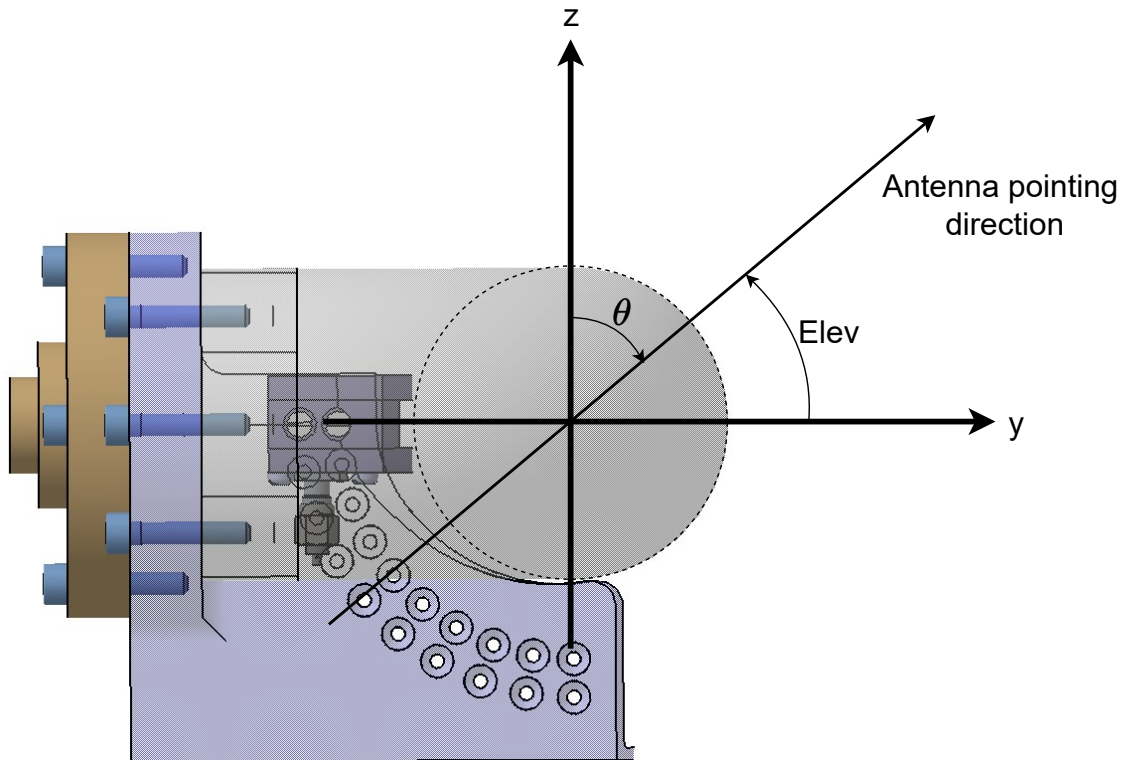


Figure 5.1 – Illustration of the elevation angle (Elev) mentioned on the measurement results. The  $\theta$  and  $\phi$  angles, and the axis are the same from Figure 2.1.

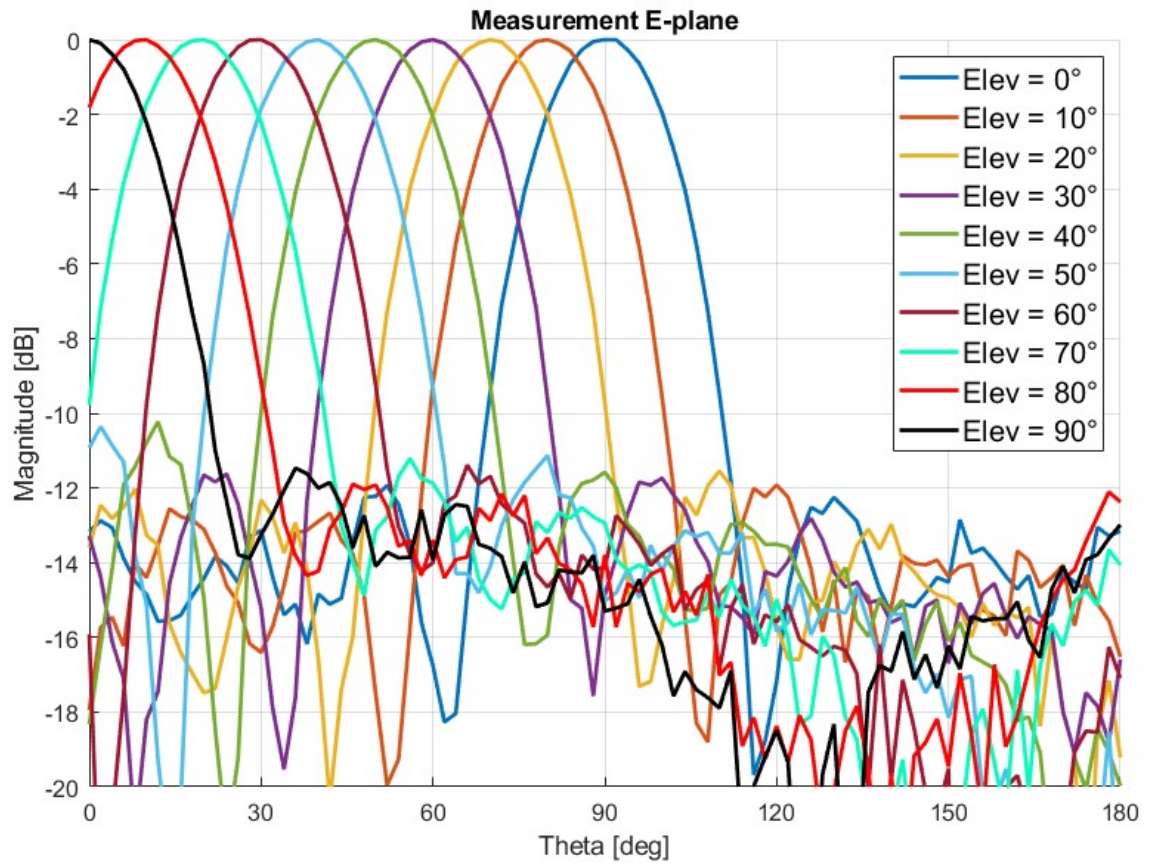


Figure 5.2 – Measurement of the radiation patter on the electric plane (E) for the lens + antenna set. "Elev" means the elevation angle in which the antenna is positioned.



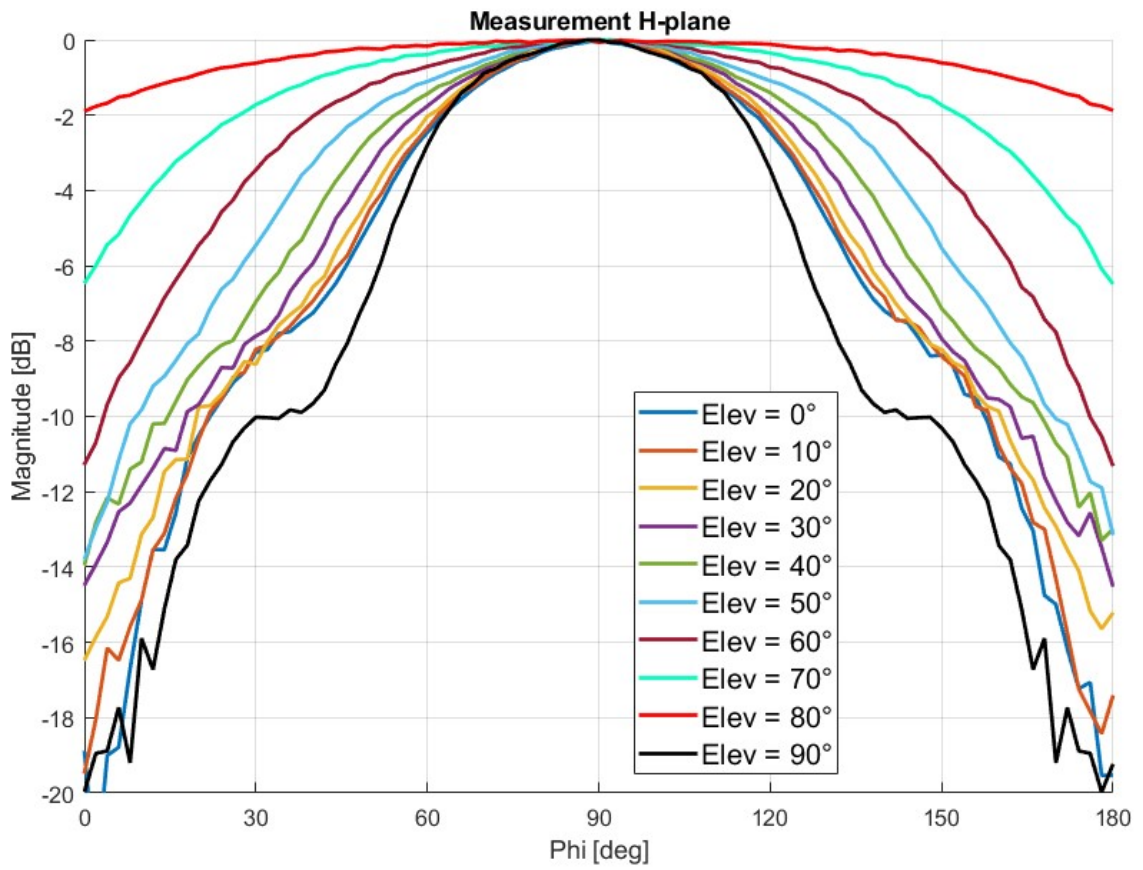
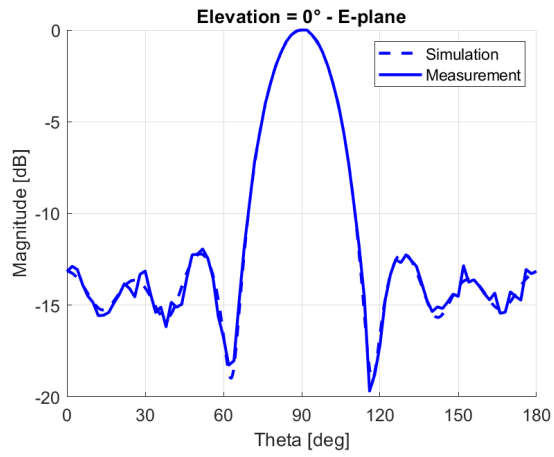
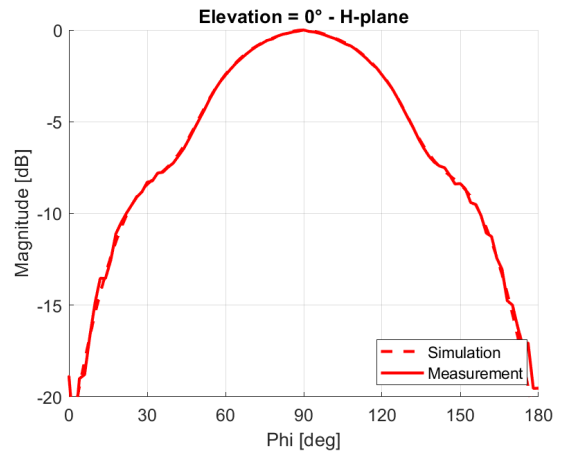


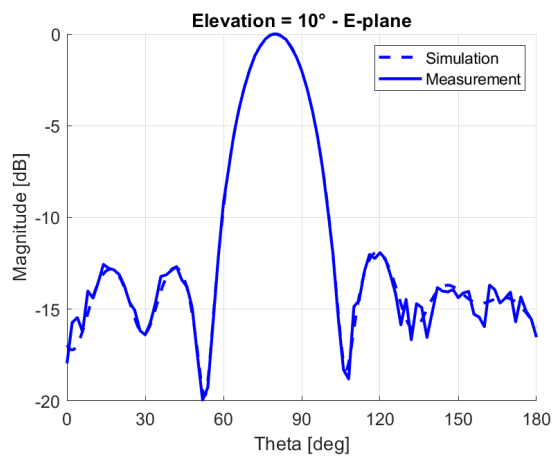
Figure 5.3 – Measurement of the radiation patten on the magnetic plane (H) for the lens + antenna set. "Elev" means the elevation angle in which the antenna is positioned.



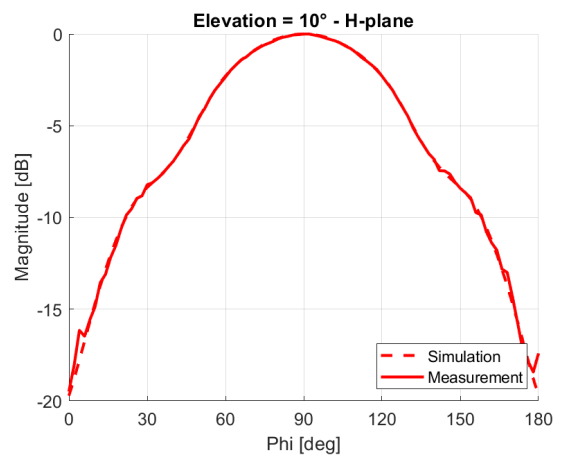
(a)



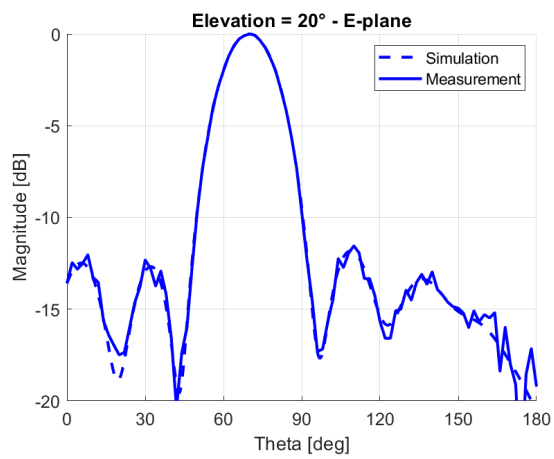
(b)



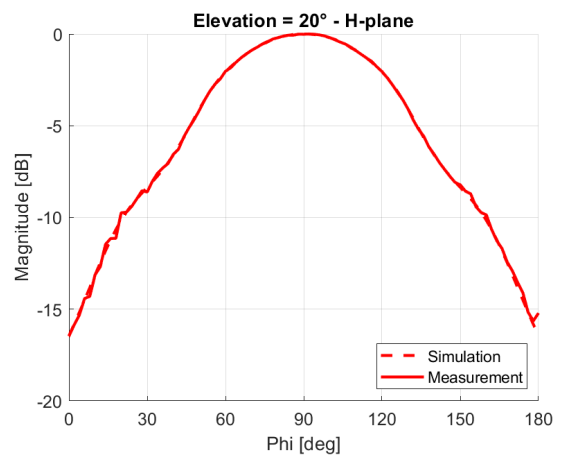
(c)



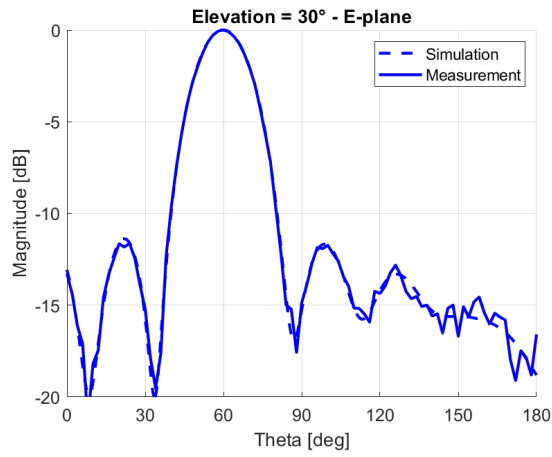
(d)



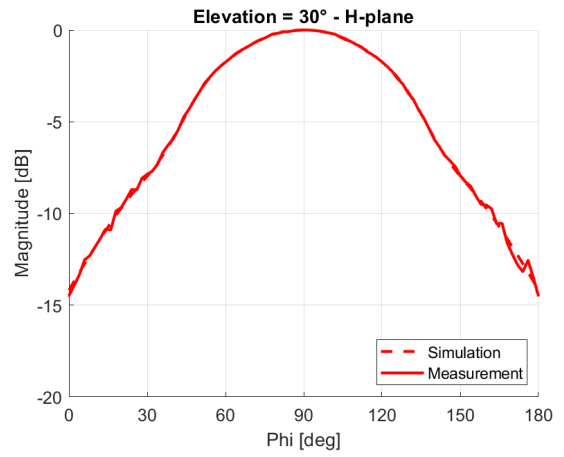
(e)



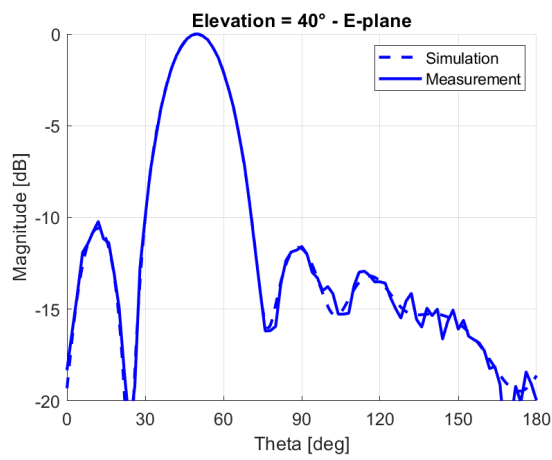
(f)



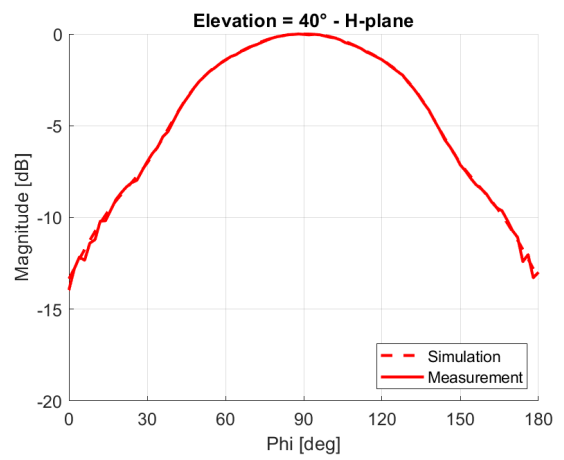
(g)



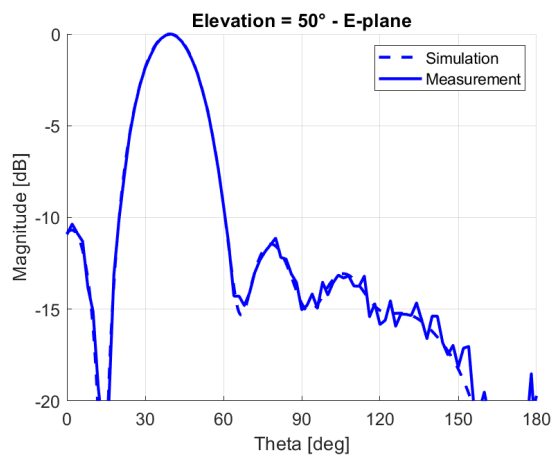
(h)



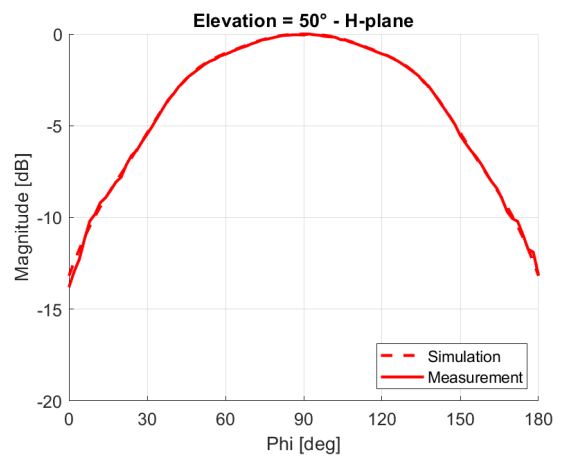
(i)



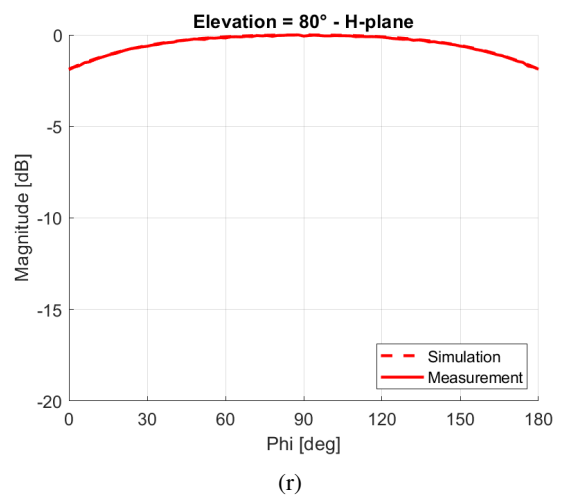
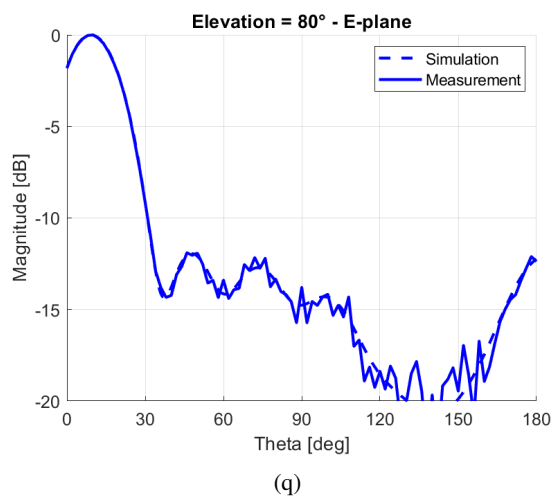
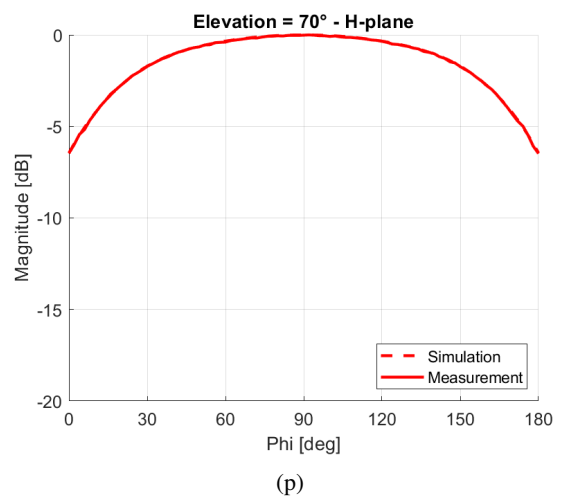
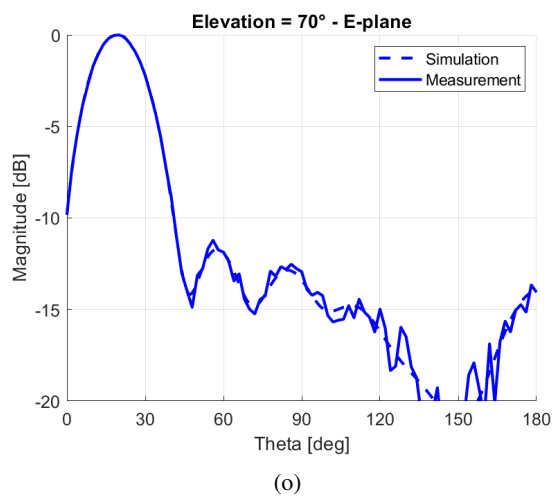
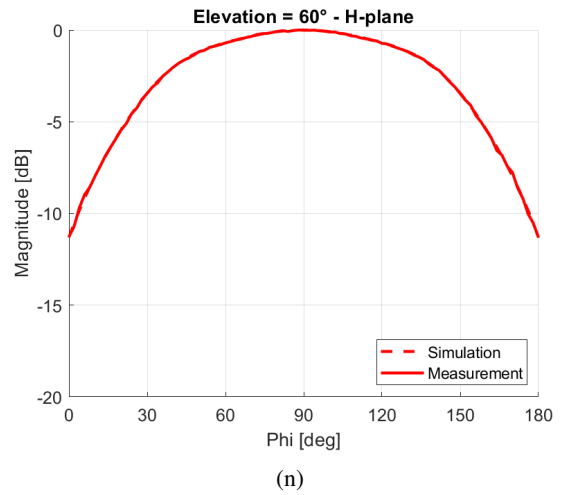
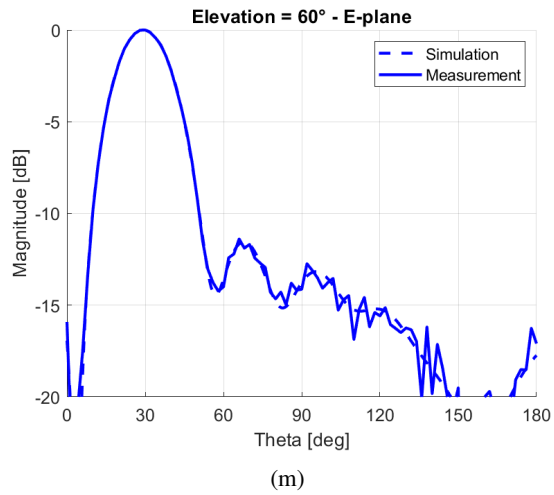
(j)



(k)



(l)



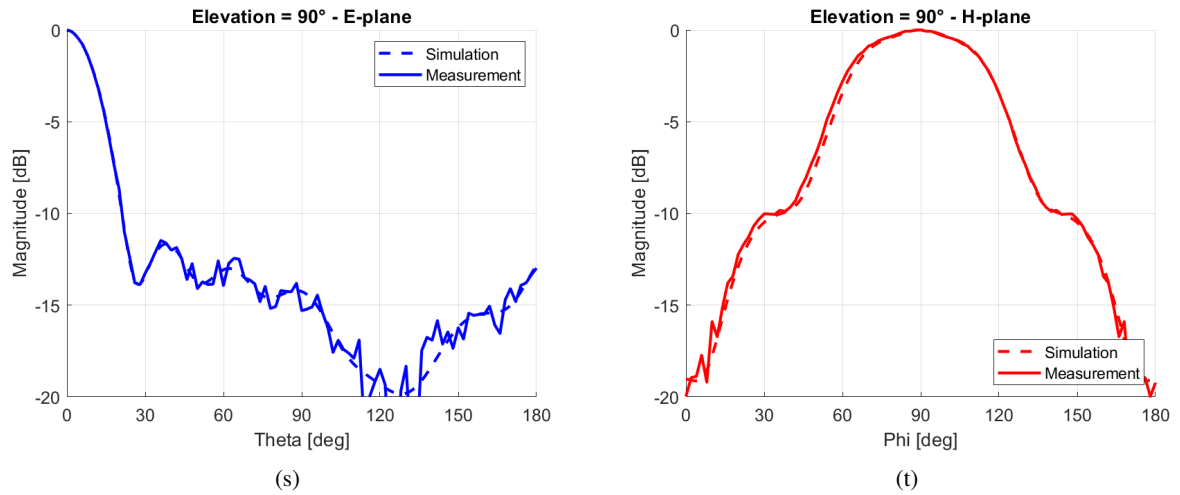


Figure 5.1 – Radiation pattern of the toroidal lens for the WR90 conformal antenna pointed at different elevation angles.

Therefore, it is seen that the measurements have a good fit with the predicted results from FEM simulations, proving that the 3D-printed toroidal lens can accomplish its functionalities.

# 6

## CONCLUSION

---

3D-printing enables a new variety of methods for the realization of gradient index lenses. Without this technology, the possible shapes, material, and methodology were limited by the particularities of the machining process. In this work, the 3D-printing technique was initially validated for the studied structure by means of a section sample of a toroid, showing that the printing orientation was feasible, with the necessary characteristics of radial infill ratio variation. Then, a toroidal lens prototype was presented and measured on the far-field, attached to a WR90 open-ended conformal waveguide antenna. Despite the small imperfections noted on the printing, the lens could still work as predicted by simulations, as a result of robustness of the optical solution.

The radiation pattern of the lens+antenna set was evaluated for the antenna at different elevation angles, and it was verified that the beams on the electric plane have similar shape, due to the similar geometry of the cross section on the vertical plane. Moreover, for the magnetic (H) plane, it was noticed a variation on the beam shape, with larger beamwidth as the elevation angle increases, effect of the different distribution of permittivity across the H-plane for different elevation angles.

Given the new structural possibilities, the toroidal lens became feasible with less complexity and more reliability, and the torus shape could be explored for multi-directional antenna sets, which can be applied to radars and MIMO systems. The toroidal Luneburg lens that was previously proposed by the patent identified on the bibliographic research received a quantitative analysis as a function of the electrical size (in terms of wavelength) of the structure.

The directivity of the toroidal lens is close to the cylindrical lens of same dimension, but the torus presented a reduction of the side lobe level. The isolation between waveguide antennas on an emulated MIMO antenna setup is satisfactory, mainly for differences in elevation angles above 30°, where it achieves values below -15 dB.

To construct the lens with the appropriate accuracy and confidence, it was necessary to characterize the ABS in terms of its relative permittivity, using TRL calibration and NRW retrieval method. Since the model obtained from several measurements express  $\epsilon_r$  as a non-linear function of the infill ratio, the nominal dielectric constant information by itself is not sufficient to build the gradient index lens. The model for the dielectric constant and the density correction factor encountered are close to the results from similar work pairs.

### 6.1 FUTURE WORKS

A future work suggested is to use different types of antennas, such as dipole, Vivaldi, and patch. The use of conformal patch antennas could reduce the weight of the assembly, and increase the number of possible channels, due to the potentially smaller dimension of such devices.

The use of materials with lower dielectric constant, such as pure Polypropylene, can optimize the

dynamic range of the infill ratio along the lens. This is useful when designing electrically large lenses.

Moreover, it is proposed the construction of a lens using magnetic inclusions to control the magnetic permeability, as mentioned in Section 2.12.1, with the proposal of eliminating the reflections of the wave inside the lens and reducing the weight of the structure.

Despite the fact that the lens with higher number of layers can approximate the Luneburg Lens equation with a fair performance, it still yields a discontinuous structure. Varying the infill ratio continuously, following the Luneburg equation would eliminate those discontinuities and approximate even more the results to the predictions from the optical theory.

Finally, the analytical solution of the electromagnetic fields can be done in toroidal coordinates, using the theory described in Appendix A. The use toroidal coordinates would inherently result in non-concentric circles profile, but simulations show that it possible to achieve a similar radiation pattern. Still, some adjusts are necessary to achieve better performance, which can be done using optimizations based on the analytical model.

## BIBLIOGRAPHY

---

- 1 KADĚRA, P. et al. Gradient-index-based frequency-coded retroreflective lenses for mm-wave indoor localization. *IEEE Access*, v. 8, p. 212765–212775, 01 2020.
- 2 BLACK, E. J. Holographic Beam Forming and MIMO. *Pivotal Commware*, 2017.
- 3 RONDINEAU, S.; HIMDI, M.; SORIEUX, J. A Sliced Spherical Luneburg Lens. *Antennas and Wireless Propagation Letters, IEEE*, v. 2, p. 163 – 166, 02 2003.
- 4 ZHANG, S. et al. 3d-printed planar graded index lens. In: . [S.l.: s.n.], 2018.
- 5 ZIMMERMAN et al. *Luneburg Lens and Methods of Constructing Same*. October 14, 1997.
- 6 BUGAJ, J.; WNUK, M.; BUGAJ, M. Parametric study of the cylindrical microstrip antenna. In: *2015 IEEE International Conference on Microwaves, Communications, Antennas and Electronic Systems (COMCAS)*. [S.l.: s.n.], 2015. p. 1–4.
- 7 BEENAMOLE, K.; SREEJITH, C. A.; SHANKAR, G. Studies on conformal antenna arrays placed on cylindrical curved surfaces. In: *2016 International Symposium on Antennas and Propagation (APSYM)*. [S.l.: s.n.], 2016. p. 1–3.
- 8 LEVCHENKO, S. N.; KHARLANOV, Y. Y. *Scanning toroidal lens antenna*. CL 7 H 01 Q 15/08., 27.03.2000. Disponível em: <<https://russianpatents.com/patent/214/2147150.html>>.
- 9 RODRIGUES, H. et al. Wideband Omnidirectional Slotted-Waveguide Antenna Array Based on Trapezoidal Slots. *International Journal of Antennas and Propagation*, v. 2019, 10 2019.
- 10 ORFANIDIS, S. J. *Electromagnetic waves and antennas*. Rutgers University New Brunswick, NJ, 2016.
- 11 BALANIS, C. A. *Antenna theory: analysis and design*. [S.l.]: John wiley & sons, 2015.
- 12 LUNEBURG, R. K. *Mathematical theory of optics*. [S.l.]: University of California Press, 2021.
- 13 OXBURGH, S.; TYC, T.; COURTIAL, J. Dr TIM: Ray-tracer TIM, with additional specialist scientific capabilities. *Computer Physics Communications*, v. 185, n. 3, p. 1027–1037, 2014. ISSN 0010-4655. Disponível em: <<https://www.sciencedirect.com/science/article/pii/S0010465513003767>>.
- 14 EIA RS-261-B. *Rectangular Waveguides (WR3 to WR2300)*. [S.l.]: Standard of the Electronic Industries Association of the United States of America, 1979.
- 15 ZHANG, J. et al. Resistivity and its anisotropy characterization of 3D-printed acrylonitrile butadiene styrene copolymer (ABS)/carbon black (CB) composites. *Applied Sciences*, Multidisciplinary Digital Publishing Institute, v. 7, n. 1, p. 20, 2017.
- 16 STRATASYS. *FDM Support Materials*. Disponível em: <<https://support.stratasys.com/en/materials/fdm/fdm-support-materials>>.
- 17 BATES, J. W.; LEWIS, H. R. Hamiltonian description of toroidal magnetic fields in vacuum. *Physics of Plasmas*, American Institute of Physics, v. 4, n. 7, p. 2619–2630, 1997.
- 18 MIAO, J. *Ka-band 2D luneburg lens design with glide-symmetric metasurface*. 2017.
- 19 BOSILJEVAC, M. et al. Non-Uniform Metasurface Luneburg Lens Antenna Design. *IEEE Transactions on Antennas and Propagation*, v. 60, n. 9, p. 4065–4073, 2012.



- 20 LUNEWAVE. *Lunewave – Cutting edge antenna and sensor technology for automotive (ADAS/AV), wireless communications, robotics and drones*. Disponível em: <<https://lunewave.com/>>.
- 21 SAHLI, E. et al. Beamforming techniques for massive MIMO systems in 5G: overview, classification, and trends for future research. *Frontiers of Information Technology & Electronic Engineering*, v. 18, p. 753–772, 06 2017.
- 22 LUNEBERG. *Luneberg – Radar Reflector Solutions*. Disponível em: <<https://luneberg.com/>>.
- 23 ALLAM, A.; SABRA, K.; ERTURK, A. 3D-Printed Gradient-Index Phononic Crystal Lens for Underwater Acoustic Wave Focusing. *Physical Review Applied*, v. 13, 06 2020.
- 24 LU, C. et al. GRIN metamaterial generalized Luneburg lens for ultra-long acoustic jet. *Applied Physics Letters*, v. 118, n. 14, p. 144103, 2021. Disponível em: <<https://doi.org/10.1063/5.0044436>>.
- 25 KIM, S.-H. Cylindrical acoustic Luneburg lens. In: *2014 8th International Congress on Advanced Electromagnetic Materials in Microwaves and Optics*. [S.l.: s.n.], 2014. p. 364–366.
- 26 RONDINEAU, S. *Modelisation de lentilles spheriques a gradient d'indice et sources conformes associees*. Tese (Doutorado) — L'Universite de Rennes 1, 2002.
- 27 LIANG, M. et al. A 3-D Luneburg Lens Antenna Fabricated by Polymer Jetting Rapid Prototyping. *IEEE Transactions on Antennas and Propagation*, v. 62, n. 4, p. 1799–1807, 2014.
- 28 ZHANG, S. et al. 3D-printed graded index lens for RF applications. In: *2016 International Symposium on Antennas and Propagation (ISAP)*. [S.l.: s.n.], 2016. p. 90–91.
- 29 YIN, M. et al. All-dielectric three-dimensional broadband Eaton lens with large refractive index range. *Applied Physics Letters*, v. 104, n. 9, p. 094101, 2014. Disponível em: <<https://doi.org/10.1063/1.4867704>>.
- 30 JOSEFSSON, L.; PERSSON, P. *Conformal array antenna theory and design*. [S.l.]: John Wiley & sons, 2006.
- 31 MALTSEV, A. et al. Millimeter-wave Toroidal Lens-Array Antennas Experimental Measurements. In: *2018 IEEE International Symposium on Antennas and Propagation USNC/URSI National Radio Science Meeting*. [S.l.: s.n.], 2018. p. 607–608.
- 32 MALTSEV, A. et al. Steerable Toroidal Bifocal Lens-Array Antenna In 57–64 GHz Range. *Journal of the Russian Universities. Radioelectronics*, v. 22, n. 3, p. 36–47, 2019.
- 33 MALTSEV, A.; BOLKHOVSKAYA, O.; SELEZNEV, V. Scanning Toroidal Lens-Array Antenna With a Zoned Profile for 60 GHz Band. *IEEE Antennas and Wireless Propagation Letters*, v. 20, n. 7, p. 1150–1154, 2021.
- 34 HORST, R. L. *Non-Uniform Dielectric Toroidal Lenses*. June 7, 1966.
- 35 HANSEN, J. E. *Spherical Near-field Antenna Measurements*. [S.l.: s.n.].
- 36 MATHWORLD, W. *Toroidal Coordinates*. Disponível em: <<https://mathworld.wolfram.com/ToroidalCoordinates.html>>.
- 37 WESTON, V. *Solutions of the toroidal wave equation and their applications*. Tese (Doutorado) — University of Toronto, 1956.
- 38 WESTON, V. Toroidal wave functions. *Quarterly of Applied Mathematics*, v. 16, n. 3, p. 237–257, 1958.

- 39 WESTON, V. On toroidal wave functions. Wiley Periodicals, Inc., 1960.
- 40 POZAR, D. M. *Microwave engineering*. [S.l.]: John Wiley & sons, 2011.
- 41 FUCHS, B. et al. Design Optimization of Multishell Luneburg Lenses. *IEEE Transactions on Antennas and Propagation*, v. 55, n. 2, p. 283–289, 2007.
- 42 SIHVOLA, A.; KONG, J. Effective permittivity of dielectric mixtures. *IEEE Transactions on Geoscience and Remote Sensing*, v. 26, n. 4, p. 420–429, 1988.
- 43 ARAÚJO, A. F. P. d. Modernização de uma Impressora Stratasys. *Trabalho de Conclusão de Curso (Bacharelado em Engenharia Eletrônica)*, Universidade de Brasília, 2019.
- 44 LIU, P. et al. A Novel E-plane-Focused Cylindrical Luneburg Lens Loaded With Metal Grids for Sidelobe Level Reduction. *IEEE Transactions on Antennas and Propagation*, v. 68, n. 2, p. 736–744, 2020.
- 45 ANSYS. *Ansys HFSS Best-In-Class 3D High Frequency Electromagnetic Simulation Software*. Disponível em: <<https://www.ansys.com/products/electronics/ansys-hfss>>.
- 46 REDDY, J. N. *Introduction to the finite element method*. [S.l.]: McGraw-Hill Education, 2019.
- 47 ANSYS. *HFSS Help*. Disponível em: <<https://ansyshelp.ansys.com/>>.
- 48 LUO, C.-M.; HONG, J.-S.; ZHONG, L.-L. Isolation Enhancement of a Very Compact UWB-MIMO Slot Antenna With Two Defected Ground Structures. *IEEE Antennas and Wireless Propagation Letters*, v. 14, p. 1766–1769, 2015.
- 49 CYPRESS. *Antenna Placement Guidelines For 2x2 MIMO WLAN*. Disponível em: <[https://www.infineon.com/dgdl/Infineon-AN214810\\_Antenna\\_Placement\\_Guidelines\\_For\\_2\\_2\\_MIMO\\_WLAN-ApplicationNotes-v03\\_00-EN.pdf?fileId=8ac78c8c7cdc391c017d0d27bb9962ec](https://www.infineon.com/dgdl/Infineon-AN214810_Antenna_Placement_Guidelines_For_2_2_MIMO_WLAN-ApplicationNotes-v03_00-EN.pdf?fileId=8ac78c8c7cdc391c017d0d27bb9962ec)>.
- 50 CHEN, X.; ZHANG, S.; LI, Q. A Review of Mutual Coupling in MIMO Systems. *IEEE Access*, v. 6, p. 24706–24719, 2018.
- 51 3D-FILA. *Filamento ABS Premium+*. Disponível em: <<https://3dfila.com.br/produto/filamento-abs-premium>>.
- 52 ROHDE & SCHWARZ. *Measurement of Dielectric Material Properties*. 2012.
- 53 BAKER-JARVIS, J. *Transmission/Reflection and Short-Circuit Line Permittivity Measurements*. Disponível em: <<https://nvlpubs.nist.gov/nistpubs/Legacy/TN/nbstechnicalnote1341.pdf>>.
- 54 KEYSIGHT. *Full 2-Port Calibration*. Disponível em: <[https://ena.support.keysight.com/e5061b/manuals/webhelp/eng/measurement/calibration/basic\\_calibrations/full\\_2\\_port\\_calibration.htm](https://ena.support.keysight.com/e5061b/manuals/webhelp/eng/measurement/calibration/basic_calibrations/full_2_port_calibration.htm)>.
- 55 NICOLSON, A. M.; ROSS, G. F. Measurement of the Intrinsic Properties of Materials by Time-Domain Techniques. *IEEE Transactions on Instrumentation and Measurement*, v. 19, n. 4, p. 377–382, 1970.
- 56 WEIR, W. B. Automatic measurement of complex dielectric constant and permeability at microwave frequencies. *Proceedings of the IEEE*, v. 62, n. 1, p. 33–36, 1974.
- 57 EZZAT, M.; SABIHA, N.; IZZULARAB, M. Accurate model for computing dielectric constant of dielectric nanocomposites. *Applied Nanoscience*, Springer, v. 4, n. 3, p. 331–338, 2014.

- 58 COLELLA, R.; CHIETERA, F. P.; CATARINUCCI, L. Analysis of FDM and DLP 3D-printing technologies to prototype electromagnetic devices for RFID applications. *Sensors*, Multidisciplinary Digital Publishing Institute, v. 21, n. 3, p. 897, 2021.
- 59 COUDERC, H. et al. Fabrication and dielectric properties of highly loaded polypropylene micro- and nano-composites. In: *2016 IEEE Conference on Electrical Insulation and Dielectric Phenomena (CEIDP)*. [S.l.: s.n.], 2016. p. 534–537.
- 60 MARTINS, N. et al. Misturas físicas de polipropileno com aditivos condutores: obtenção, caracterização e aplicação para blindagem eletromagnética. Florianópolis, SC, 2012.
- 61 ISOLAPLAST. *Polipropileno (PP) [Polypropylene] - Datasheet*. Disponível em: <<https://isolaplast.com.br/wp-content/uploads/2019/10/Ficha-PPN-.pdf>>.
- 62 BRASKEM. *FL100PP [Polypropylene] - Datasheet*. Disponível em: <<https://www.braskem.com.br/portal/Principal/arquivos/impressao-3d-produtos/Folha%20de%20dados%20-%20FL100PP%20-%20PT.pdf>>.
- 63 LI, Y. et al. Multibeam 3-D-Printed Luneburg Lens Fed by Magnetolectric Dipole Antennas for Millimeter-Wave MIMO Applications. *IEEE Transactions on Antennas and Propagation*, v. 67, n. 5, p. 2923–2933, 2019.
- 64 YIN, M. et al. Design and fabrication of integrated micro/macrostructure for 3D functional gradient systems based on additive manufacturing. *Optics Communications*, Elsevier, v. 414, p. 195–201, 2018.
- 65 ULTIMAKER. *Ultimaker Cura*. Disponível em: <<https://ultimaker.com/software/ultimaker-cura>>.
- 66 MARLIN. *G-code Index*. Disponível em: <<https://marlinfw.org/meta/gcode/>>.
- 67 ANSARI, M. et al. A Highly Efficient Spherical Luneburg Lens for Low Microwave Frequencies Realized With a Metal-Based Artificial Medium. *IEEE Transactions on Antennas and Propagation*, v. 69, n. 7, p. 3758–3770, 2021.
- 68 PYPI. *PyQt5 - Python bindings for the Qt cross platform application toolkit*. Disponível em: <<https://pypi.org/project/PyQt5/>>.
- 69 NIST. *Spherical Bessel Functions*. [S.l.]. Disponível em: <<https://dlmf.nist.gov/10.47#E4>>.

# **APPENDIX**

# A STUDY ON THE ANALYTICAL SOLUTION FOR THE TOROIDAL LENS

## A.1 TOROIDAL COORDINATES

The toroidal coordinate system will be used. It is illustrated in Fig. A.1.

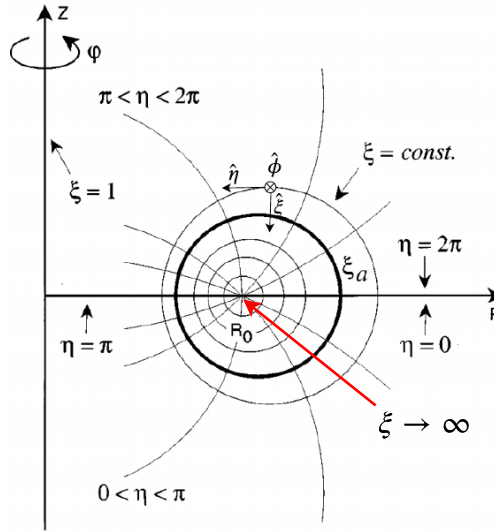


Figure A.1 – Toroidal Coordinate System. Source: [17] (Adapted)

There will be used discrete layers lenses, where the layer's boundaries are defined by the circles  $\xi = \xi_a$ .

The relations with the Cartesian system are:

$$\begin{aligned} x &= \frac{d \sinh \xi \cos \phi}{\cosh \xi - \cos \eta}, \\ y &= \frac{d \sinh \xi \sin \phi}{\cosh \xi - \cos \eta}, \\ z &= \frac{d \sin \eta}{\cosh \xi - \cos \eta} \end{aligned} \quad (\text{A.1})$$

Where  $d = R_0$  is the radius around which the torus is defined.

The metric coefficients are:

$$\begin{aligned} h_\xi = h_\eta &= \frac{d}{\cosh \xi - \cos \eta}, \\ h_\phi &= \frac{d \sinh \xi}{\cosh \xi - \cos \eta} \end{aligned} \quad (\text{A.2})$$

It will be used the variable  $s$  instead of  $\xi$ , related by:

$$s = \cosh \xi \quad (\text{A.3})$$

The orthonormal direct base is then given by

$$\{\hat{\xi}, \hat{\eta}, \hat{\phi}\}$$

## A.2 TOROIDAL WAVE FUNCTIONS

### A.2.1 Basis functions

For electromagnetic problems described in toroidal coordinates, the following wave functions were presented in [38]:

$$\psi_{esN}^M(s, \eta, \phi) = e^{jm\phi} V_{s[M+2l]}^M(s, \eta) \quad (\text{A.4})$$

$$\psi_{osN}^M(s, \eta, \phi) = e^{jm\phi} W_{s[M+2l+1]}^M(s, \eta) \quad (\text{A.5})$$

$s$  indicates the type of wave, according to [35], which will be used later in this section:

- $s = 1 \rightarrow$  Similar to the Spherical **Bessel** function representing a radial **standing wave, finite at the origin**.
- $s = 2 \rightarrow$  Similar to the Spherical **Neumann** function representing a radial **standing wave, infinite at the origin**.
- $s = 3 \rightarrow$  Similar to the Spherical **Hankel** function of the **first kind**, representing a radial **outgoing wave**, infinite at the origin.
- $s = 4 \rightarrow$  Similar to the Spherical **Hankel** function of the **second kind**, representing a radial **incoming wave**, infinite at the origin.

With the expression for the outgoing wave ( $s = 3$ ), still from [38]:

$$V_{3N}^M = S_N^M + j(-1)^{N+1} S_{-N-1}^M \quad (\text{A.6})$$

$$W_{3N}^M = T_N^M + j(-1)^{N+1} T_{-N-1}^M \quad (\text{A.7})$$

$$S_N^M = \frac{(N+M)! \sqrt{\pi} (-1)^M (kd)^N}{(N-M)! 2^{(M+N)/2+1} (s - \cos \eta)^{(M+N)/2}} \sum_{p=0}^{\infty} \frac{(kd)^{2p} (-1)^p K_p^1}{(s - \cos \eta)^{p+1}} \quad (\text{A.8})$$

$$T_N^M = \frac{(N+M)! \sqrt{\pi} (-1)^M \sin \eta (kd)^N}{(N-M)! 2^{(M+N+3)/2} (s - \cos \eta)^{(M+N+1)/2}} \sum_{p=0}^{\infty} \frac{(kd)^{2p} (-1)^p K_p^2}{(s - \cos \eta)^{p2p}} \quad (\text{A.9})$$

$$K_p^1 = \frac{1}{p! \Gamma(N + 3/2 + p)} \sum_{r=0}^l \frac{\left(\frac{M-N}{2}\right)_r \left(\frac{N+M+1}{2}\right)_r (s^2 - 1)^{r/2}}{r! (s - \cos \eta)^r} P_{p+(M+N)/2}^{-M-r}(s) \quad (\text{A.10})$$

$$K_p^2 = \frac{1}{p! \Gamma(N + 3/2 + p)} \sum_{r=0}^l \frac{\left(\frac{M-N+1}{2}\right)_r \left(\frac{N+M}{2} + 1\right)_r (s^2 - 1)^{r/2}}{r! (s - \cos \eta)^r} P_{p+(M+N-1)/2}^{-M-r}(s) \quad (\text{A.11})$$

Where:

$e$  - even,  $o$  - odd,  $N = M + 2l$ ,  $l \in \mathbb{N}$ ,  $M = |m|$ ,  $m \in \mathbb{Z}$ ,  $\Gamma(x) = (x-1)!$ , and  $(x)_r \equiv \frac{\Gamma(x+n)}{\Gamma(x)}$  is the Pochhammer symbol.

From [38], the functions on equations A.6 and A.7 converges to spherical wave functions at the limit:

$$\lim_{d \rightarrow 0} V_N^M = h_N^{(1)}(kR) P_N^M(\cos \theta)$$

$$\lim_{d \rightarrow 0} W_N^M = h_N^{(1)}(kR) P_N^M(\cos \theta)$$

In spherical coordinates, the outgoing wave function is represented with  $h_N^{(1)}$  and the incoming waves are represented by  $h_N^{(2)}$  [35].

From [69]:

$$h_n^{(1)}(z) = j_n(z) + jy_n(z) \quad (\text{A.12})$$

$$h_n^{(2)}(z) = j_n(z) - jy_n(z) \quad (\text{A.13})$$

Therefore, by similarity, it is possible to apply the equations from [38] into the models from the Spherical Wave equations in [35], leading us to the representations:

incoming wave ( $s = 4$ ):

$$V_{4N}^M = S_N^M - j(-1)^{N+1} S_{-N-1}^M \quad (\text{A.14})$$

$$W_{4N}^M = T_N^M - j(-1)^{N+1} T_{-N-1}^M \quad (\text{A.15})$$

The standing wave, finite at the origin ( $s = 1$ ):

$$V_{1N}^M = S_N^M \quad (\text{A.16})$$

$$W_{1N}^M = T_N^M \quad (\text{A.17})$$

And the standing wave, infinite at the origin ( $s = 2$ ):

$$V_{2N}^M = S_{-N-1}^M \quad (\text{A.18})$$

$$W_{2N}^M = T_{-N-1}^M \quad (\text{A.19})$$

With this at hand, we can set the basis for the vectorial Helmholtz equation:

$$\begin{aligned} \vec{M}_{\sigma s N}^M &= \nabla \times (\psi_{\sigma s N}^M \hat{\xi}) \\ \vec{N}_{\sigma s N}^M &= \frac{1}{\kappa} \nabla \times \vec{M}_{\sigma s N}^M \\ \vec{L}_{\sigma s N}^M &= \nabla \psi_{\sigma s N}^M \end{aligned} \quad (\text{A.20})$$

Where  $\kappa = k_\xi$  is the wave number of the wave propagated in the direction  $\hat{\xi}$ .

Being A.20 a complete basis, the electric field can be expressed as a linear combination of its components:

$$\vec{E} = \sum_{\sigma s M N} a_{\sigma s N}^M \vec{M}_{\sigma s N}^M + b_{\sigma s N}^M \vec{N}_{\sigma s N}^M + c_{\sigma s N}^M \vec{L}_{\sigma s N}^M \quad (\text{A.21})$$

### A.2.1.1 Convergence

For the radiation condition ( $s \rightarrow 1$ ) Weston [38] mathematically shows how the problem converges to the one described by spherical coordinates, which is very well dominated in literature [26]. This analysis is made by setting  $d \rightarrow 0$ , and is also intuitive because it will centers the torus core at the origin, overlapping it for every  $\phi$ , indeed turning the torus into a sphere.

For the case  $s \rightarrow \infty$ , *i. e.* internal problem, the infinitesimally thin torus (core) is analyzed. As shown by Weston, and also numerically verified, functions  $S$  and  $T$  (equations A.8 and A.9) converges under the wave number condition:

$$s > kd$$

This is also verified to be true by the limit



$$\lim_{s \rightarrow \infty} \frac{(kd)^N}{(s - \cos \eta)^{(M+N)/2}} = 0, \text{ if } s > kd \quad \forall M \quad (\text{A.22})$$

### A.2.2 Charge-less medium

From Maxwell's equations, assuming a medium without charges  $\nabla \cdot \vec{E} = 0$ . Then, using the divergent distributive property:

$$\nabla \cdot \vec{E} = \sum_{\sigma s M l} a_{\sigma s N}^M \nabla \cdot \vec{M}_{\sigma s N}^M + b_{\sigma s N}^M \nabla \cdot \vec{N}_{\sigma s N}^M + c_{\sigma s N}^M \nabla \cdot \vec{L}_{\sigma s N}^M = 0 \quad (\text{A.23})$$

Since

$$\nabla \cdot \nabla \times \vec{a} = 0 \quad (\text{A.24})$$

It is easy to see that  $c_{\sigma s N}^M = 0$ .

Hence, in a charge-free medium, the electric field can be defined as:

$$\vec{E} = \sum_{\sigma s M l} a_{\sigma s N}^M \vec{M}_{\sigma s N}^M + b_{\sigma s N}^M \vec{N}_{\sigma s N}^M \quad (\text{A.25})$$

Also using Maxwell's equation, the magnetic field is obtained:

$$\begin{aligned} \nabla \times \vec{E} &= -j\omega\mu\vec{H} \\ \vec{H} &= \frac{j}{\omega\mu} \nabla \times \vec{E} \end{aligned} \quad (\text{A.26})$$

Using distributive properties of curl, it is calculated each term of  $\nabla \times \vec{E}$

$$\nabla \times \vec{M}_{\sigma s N}^M = \kappa \vec{N}_{\sigma s N}^M \quad (\text{A.27})$$

$$\nabla \times \vec{N}_{\sigma s N}^M = \frac{1}{\kappa} \nabla \times \nabla \times \vec{M}_{\sigma s N}^M = \frac{1}{\kappa} \left[ \nabla \nabla \cdot \vec{M}_{\sigma s N}^M - \nabla^2 \vec{M}_{\sigma s N}^M \right] = -\frac{1}{\kappa} \nabla^2 \vec{M}_{\sigma s N}^M \quad (\text{A.28})$$

Therefore

$$\vec{H} = \frac{j\kappa}{\omega\mu} \sum_{\sigma s M l} a_{\sigma s N}^M \vec{N}_{\sigma s N}^M + b_{\sigma s N}^M \vec{M}_{\sigma s N}^M \quad (\text{A.29})$$

### A.2.3 Parallel functions

Parallel vectorial functions are defined with reference to a propagation vector. The parallel vectorial functions describes the function tangent to the surface of the object. The definition is as follows:

$$\vec{A}_{//} = \vec{A} - A_{\xi} \hat{\xi} = A_{\eta} \hat{\eta} + A_{\phi} \hat{\phi} \quad (\text{A.30})$$

Where  $\hat{\xi}$  is the propagation vector.

### A.2.4 Continuity relations

To analyze the fields over multiple torus layers, we must assume that the field is continuous over the interfaces. Thereby, for an interface between layers  $\alpha$  and  $\alpha+1$ , the parallel ( $//$ ) fields are equal at the limit of both sides, independently of the materials:

$$\begin{aligned} \vec{E}_{\alpha, //} &= \vec{E}_{\alpha+1, //} \\ \vec{H}_{\alpha, //} &= \vec{H}_{\alpha+1, //} \end{aligned} \quad (\text{A.31})$$

or

$$\begin{aligned} \vec{E}_{\alpha} \times \hat{\xi}_p &= \vec{E}_{\alpha+1} \times \hat{\xi}_p \\ \vec{H}_{\alpha} \times \hat{\xi}_p &= \vec{H}_{\alpha+1} \times \hat{\xi}_p \end{aligned} \quad (\text{A.32})$$

$\forall \eta \in [0, 2\pi[, \forall \phi \in [0, 2\pi[$

Applying those conditions in the fields expression:

$$\begin{aligned} \sum_{\sigma s M l} a_{\sigma s N}^{M[\alpha]} \vec{M}_{\sigma s N}^{M[\alpha]} \times \hat{\xi}_p + b_{\sigma s N}^{M[\alpha]} \vec{N}_{\sigma s N}^{M[\alpha]} \times \hat{\xi}_p &= \sum_{\sigma s M l} a_{\sigma s N}^{M[\alpha+1]} \vec{M}_{\sigma s N}^{M[\alpha+1]} \times \hat{\xi}_p + b_{\sigma s N}^{M[\alpha+1]} \vec{N}_{\sigma s N}^{M[\alpha+1]} \times \hat{\xi}_p = \dots \\ \dots &= \sum_{\sigma s M l} \vec{Q}_{\sigma s N}^M[\alpha] = \sum_{\sigma s M l} \vec{Q}_{\sigma s N}^M[\alpha + 1] \end{aligned} \quad (\text{A.33})$$

$$\begin{aligned} \frac{j\kappa^{[\alpha]}}{\omega\mu^{[\alpha]}} \sum_{\sigma M N} a_{\sigma s L}^{M[\alpha]} \vec{N}_{\sigma s N}^{M[\alpha]} \times \hat{\xi}_p + b_{\sigma s N}^{M[\alpha]} \vec{M}_{\sigma s N}^{M[\alpha]} \times \hat{\xi}_p \dots \\ \dots &= \frac{j\kappa^{[\alpha+1]}}{\omega\mu^{[\alpha+1]}} \sum_{\sigma s M l} a_{\sigma s N}^{M[\alpha+1]} \vec{N}_{\sigma s N}^{M[\alpha+1]} \times \hat{\xi}_p + b_{\sigma s N}^{M[\alpha+1]} \vec{M}_{\sigma s N}^{M[\alpha+1]} \times \hat{\xi}_p \dots \\ \dots &= \sum_{\sigma s M l} \vec{W}_{\sigma s N}^M[\alpha] = \vec{W}_{\sigma s N}^M[\alpha + 1] \end{aligned} \quad (\text{A.34})$$

To have those continuity relations over the whole surface of any torus ( $\xi = \xi_0$ ), we take the inner product of the parallel components of wave functions at  $\xi = \xi_0$ . By this step, the continuity equations A.33 and A.34 become independent of  $\eta$  and  $\phi$ .

$$\begin{aligned}
\sum_{\sigma s M l M' l'} \langle \vec{Q}_{\sigma s N}^M[\alpha], \vec{M}_{\sigma' s N' //}^{M' -} \rangle &= \sum_{\sigma s M l M' l'} \langle \vec{Q}_{\sigma s N}^M[\alpha + 1], \vec{M}_{\sigma' s N' //}^{M' +} \rangle \\
\sum_{\sigma s M l M' l'} \langle \vec{Q}_{\sigma s N}^M[\alpha], \vec{N}_{\sigma' s N' //}^{M' -} \rangle &= \sum_{\sigma s M l M' l'} \langle \vec{Q}_{\sigma s N}^M[\alpha + 1], \vec{N}_{\sigma' s N' //}^{M' +} \rangle \\
\sum_{\sigma s M l M' l'} \langle \vec{W}_{\sigma s N}^M[\alpha], \vec{M}_{\sigma' s N' //}^{M' -} \rangle &= \sum_{\sigma s M l M' l'} \langle \vec{W}_{\sigma s N}^M[\alpha + 1], \vec{M}_{\sigma' s N' //}^{M' +} \rangle \\
\sum_{\sigma s M l M' l'} \langle \vec{W}_{\sigma s N}^M[\alpha], \vec{N}_{\sigma' s N' //}^{M' -} \rangle &= \sum_{\sigma s M l M' l'} \langle \vec{W}_{\sigma s N}^M[\alpha + 1], \vec{N}_{\sigma' s N' //}^{M' +} \rangle
\end{aligned} \tag{A.35}$$

### A.2.5 Inner products

It is known that

$$\vec{M}_{\sigma s N //}^M = \vec{M}_{\sigma s N}^M$$

The inner products between the vectorial wave functions are given by:

From Equation 9.1 in [38], choosing a weight function  $\alpha(\xi, \eta) = kdh_\phi$  for the inner product, we have

$$\langle \psi_{\sigma s N}^M, \psi_{\sigma' s N'}^{M'} \rangle = \int_0^{2\pi} \int_0^{2\pi} \psi_{\sigma s N}^M \psi_{\sigma' s N'}^{M'*} \alpha(\xi, \eta) d\phi d\eta = 0, \quad M \neq M' \text{ or } \sigma \neq \sigma' \tag{A.36}$$

Therefore:

$$\begin{aligned}
\langle \vec{M}_{\sigma s N //}^M, \vec{M}_{\sigma' s N' //}^{M'} \rangle &= \int_0^{2\pi} \int_0^{2\pi} (\nabla \times \psi_{\sigma s N}^M \hat{\xi}) \cdot (\nabla \times \psi_{\sigma' s N'}^{M'*} \hat{\xi}) \alpha(\xi, \eta) d\phi d\eta \\
&= \int_0^{2\pi} \int_0^{2\pi} (\partial_\phi \psi_{\sigma s N}^M) (\partial_\phi \psi_{\sigma' s N'}^{M'*}) d\phi d\eta = 2\pi m' m \int_0^{2\pi} \int_0^{2\pi} \psi_{\sigma s N}^M \psi_{\sigma' s N'}^{M'*} \alpha(\xi, \eta) d\phi d\eta = 0, \\
&\quad M \neq M' \text{ or } \sigma \neq \sigma'
\end{aligned} \tag{A.37}$$

Other cases can be evaluated numerically, yielding:

$$\langle \vec{M}_{\sigma s N //}^M, \vec{N}_{\sigma' s N' //}^{M'} \rangle = 0, \quad \forall \{M, M', N, N', \sigma, \sigma'\} \tag{A.38}$$

$$\langle \vec{N}_{\sigma s N //}^M, \vec{N}_{\sigma' s N' //}^{M'} \rangle = 0, \quad M \neq M' \text{ or } \sigma \neq \sigma' \text{ or } N \neq N' \tag{A.39}$$

The remaining cases

$$\left\langle \vec{N}_{\sigma s N //}^M, \vec{N}_{\sigma s N //}^M \right\rangle \quad \text{and} \quad \left\langle \vec{M}_{\sigma s N //}^M, \vec{M}_{\sigma s N' //}^M \right\rangle$$

are not orthogonal.

## A.2.6 Inner product matrices

Defining the sets of inner products as matrices:

$$[MM]_{\sigma s //}^m = \begin{bmatrix} \left\langle \vec{M}_{\sigma s 0 //}^m, \vec{M}_{\sigma s 0 //}^m \right\rangle & \cdots & \left\langle \vec{M}_{\sigma s L //}^m, \vec{M}_{\sigma s 0 //}^m \right\rangle \\ \vdots & \ddots & \vdots \\ \left\langle \vec{M}_{\sigma s 0 //}^m, \vec{M}_{\sigma s L //}^m \right\rangle & \cdots & \left\langle \vec{M}_{\sigma s L //}^m, \vec{M}_{\sigma s L //}^m \right\rangle \end{bmatrix} \quad (\text{A.40})$$

$$[NN]_{\sigma s //}^m = \begin{bmatrix} \left\langle \vec{N}_{\sigma s 0 //}^m, \vec{N}_{\sigma s 0 //}^m \right\rangle & \cdots & \left\langle \vec{N}_{\sigma s L //}^m, \vec{N}_{\sigma s 0 //}^m \right\rangle \\ \vdots & \ddots & \vdots \\ \left\langle \vec{N}_{\sigma s 0 //}^m, \vec{N}_{\sigma s L //}^m \right\rangle & \cdots & \left\langle \vec{N}_{\sigma s L //}^m, \vec{N}_{\sigma s L //}^m \right\rangle \end{bmatrix} = \text{diag} \left( \left\langle \vec{N}_{\sigma s L //}^m, \vec{N}_{\sigma s L //}^m \right\rangle \right) \quad (\text{A.41})$$

$$[MN]_{\sigma s //}^m = \begin{bmatrix} \left\langle \vec{M}_{\sigma s 0 //}^m, \vec{N}_{\sigma s 0 //}^m \right\rangle & \cdots & \left\langle \vec{M}_{\sigma s L //}^m, \vec{N}_{\sigma s 0 //}^m \right\rangle \\ \vdots & \ddots & \vdots \\ \left\langle \vec{M}_{\sigma s 0 //}^m, \vec{N}_{\sigma s L //}^m \right\rangle & \cdots & \left\langle \vec{M}_{\sigma s L //}^m, \vec{N}_{\sigma s L //}^m \right\rangle \end{bmatrix} = [0]_{L \times L} \quad (\text{A.42})$$

The coefficients can be put in vectorial form:

$$\vec{a}_{\sigma s}^m = \begin{bmatrix} a_{\sigma s 0}^m \\ \vdots \\ a_{\sigma s L}^m \end{bmatrix} \quad (\text{A.43})$$

$$\vec{b}_{\sigma s}^m = \begin{bmatrix} b_{\sigma s 0}^m \\ \vdots \\ b_{\sigma s L}^m \end{bmatrix} \quad (\text{A.44})$$

In which setting the limit  $L$  for the index  $l$ .

Because of the orthogonality conditions, some indices can be taken out of the sum, and we are able to state the continuity relations for each of those indices separately.

Using the vectors presented, Equation A.35 can be expressed as:

$$[MM]_{\sigma s//}^{m-} \vec{a}_{\sigma s}^{m[\alpha]} = [MM]_{\sigma s//}^{m+} \vec{a}_{\sigma s}^{M[\alpha+1]} \quad (\text{A.45})$$

$$[NN]_{\sigma s//}^{m-} \vec{b}_{\sigma s}^{m[\alpha]} = [NN]_{\sigma s//}^{m+} \vec{b}_{\sigma s}^{m[\alpha+1]} \quad (\text{A.46})$$

$$\frac{j\kappa^{[\alpha]}}{\omega\mu^{[\alpha]}} [MM]_{\sigma s//}^{m-} \vec{b}_{\sigma s}^{m[\alpha]} = \frac{j\kappa^{[\alpha+1]}}{\omega\mu^{[\alpha+1]}} [MM]_{\sigma s//}^{m+} \vec{b}_{\sigma s}^{m[\alpha+1]} \quad (\text{A.47})$$

$$\frac{j\kappa^{[\alpha]}}{\omega\mu^{[\alpha]}} [NN]_{\sigma s//}^{m-} \vec{a}_{\sigma s}^{m[\alpha]} = \frac{j\kappa^{[\alpha+1]}}{\omega\mu^{[\alpha+1]}} [NN]_{\sigma s//}^{m+} \vec{a}_{\sigma s}^{m[\alpha+1]} \quad (\text{A.48})$$

Which holds for every  $\{\sigma, m, \alpha\}$

It is verified numerically that the matrices  $[MM]_{\sigma s//}^m$  and  $[NN]_{\sigma s//}^m$  are invertible. Therefore, the relations between coefficients from two interfacing toroidal layers  $\alpha$  and  $\alpha + 1$  can be found:

$$\vec{a}_{\sigma s}^{m[\alpha+1]} = \left[ [MM]_{\sigma s//}^{m+} \right]^{-1} [MM]_{\sigma s//}^{m-} \vec{a}_{\sigma s}^{m[\alpha]} \quad (\text{A.49})$$

$$\vec{b}_{\sigma s}^{m[\alpha+1]} = \left[ [NN]_{\sigma s//}^{m+} \right]^{-1} [NN]_{\sigma s//}^{m-} \vec{b}_{\sigma s}^{m[\alpha]} \quad (\text{A.50})$$

### A.3 MULTILAYER TORUS

To characterize an interface between two media, we use the radial coordinate  $\xi_a$  to define the limit surface bounding layer  $\alpha$ , and the wave number  $k$  inside the material to define in which side of the interface we are.

So we express the coefficients as:

$$\vec{a}_{\sigma s}^{m[\alpha+1]} = \left[ [MM]_{\sigma s//}^m(k_{\alpha+1}, \xi_a) \right]^{-1} [MM]_{\sigma s//}^m(k_{\alpha}, \xi_a) \vec{a}_{\sigma s}^{m[\alpha]} \quad (\text{A.51})$$

$$\vec{b}_{\sigma s}^{m[\alpha+1]} = \left[ [NN]_{\sigma s//}^m(k_{\alpha+1}, \xi_{\alpha}) \right]^{-1} [NN]_{\sigma s//}^m(k_{\alpha}, \xi_{\alpha}) \vec{b}_{\sigma s}^{m[\alpha]} \quad (\text{A.52})$$

The continuity equations can be propagated to a multilayer toroidal structure by cumulative effects.

Then, for a structure of  $n$  layers:

$$\vec{a}_{\sigma s}^{m[n+1]} = T_{\sigma sn}^{am} \vec{a}_{\sigma s}^{m[1]} \quad (\text{A.53})$$

$$\vec{b}_{\sigma s}^{m[n+1]} = T_{\sigma sn}^{bm} \vec{b}_{\sigma s}^{m[1]} \quad (\text{A.54})$$

Where layer 1 is the core cell of the toroidal structure, and layer  $n + 1$  is the free space.

$T_{\sigma sn}^m$  is understood as the scattering matrix of the whole structure, defined as

$$T_{\sigma sn}^{am} = \prod_{\alpha=1}^n \left[ [MM]_{\sigma s//}^m(k_{\alpha+1}, \xi_{\alpha}) \right]^{-1} [MM]_{\sigma s//}^m(k_{\alpha}, \xi_{\alpha}) \quad (\text{A.55})$$

$$T_{\sigma sn}^{bm} = \prod_{\alpha=1}^n \left[ [NN]_{\sigma s//}^m(k_{\alpha+1}, \xi_{\alpha}) \right]^{-1} [NN]_{\sigma s//}^m(k_{\alpha}, \xi_{\alpha}) \quad (\text{A.56})$$

With the definition

$$\prod_{i=1}^k A_i = A_1 \cdot A_2 \cdots A_k \quad (\text{A.57})$$

## A.4 CALCULATION OF COEFFICIENTS

Coefficients  $a_{\sigma mn}$  can be calculated using the Method of Reciprocity [35]:

$$\int_S (\vec{E}_1 \times \vec{H}_2 - \vec{E}_2 \times \vec{H}_1) \cdot d\vec{S} = \int_V (\vec{E}_2 \cdot \vec{J}_1^e - \vec{E}_1 \cdot \vec{J}_2^e - \vec{H}_2 \cdot \vec{J}_1^m + \vec{H}_1 \cdot \vec{J}_2^m) dV \quad (\text{A.58})$$

Where  $\vec{J}_\alpha^e$  and  $\vec{J}_\alpha^m$  are the *electric* and *magnetic* current on medium  $\alpha$ , respectively.

Therefore, for the exterior problem:

$$\vec{J}_2^e = \vec{J}_2^m = \vec{0}$$

$$\alpha = \frac{jk}{\omega\mu}$$

For the left part:

$$\begin{aligned} \int_S (\vec{E}_1 \times \vec{H}_2 - \vec{E}_2 \times \vec{H}_1) \cdot d\vec{S} &= \int_S \sum_{m\sigma l} \left[ (a_{\sigma 1l}^m \vec{M}_{\sigma 1l}^m + b_{\sigma 1l}^m \vec{N}_{\sigma 1l}^m) \times \alpha (a_{\sigma 3l}^m \vec{N}_{\sigma 3l}^m + b_{\sigma 3l}^m \vec{B}_{\sigma 3l}^m) \right. \\ &\quad \left. - (a_{\sigma 3l}^m \vec{M}_{\sigma 3l}^m + b_{\sigma 3l}^m \vec{N}_{\sigma 3l}^m) \times \alpha (a_{\sigma 1l}^m \vec{N}_{\sigma 1l}^m + b_{\sigma 1l}^m \vec{B}_{\sigma 1l}^m) \right] \cdot d\vec{S} \end{aligned} \quad (\text{A.59})$$

$$\begin{aligned} \dots &= \alpha \int_S \sum_{m\sigma l} \left[ a_{\sigma 1l}^m a_{\sigma 3l}^m (\vec{M}_{\sigma 1l}^m \times \vec{N}_{\sigma 3l}^m) + b_{\sigma 1l}^m b_{\sigma 3l}^m (\vec{N}_{\sigma 1l}^m \times \vec{M}_{\sigma 3l}^m) \right. \\ &\quad \left. - a_{\sigma 3l}^m a_{\sigma 1l}^m (\vec{M}_{\sigma 3l}^m \times \vec{N}_{\sigma 1l}^m) - b_{\sigma 3l}^m b_{\sigma 1l}^m (\vec{N}_{\sigma 3l}^m \times \vec{M}_{\sigma 1l}^m) \right] \cdot d\vec{S} \end{aligned} \quad (\text{A.60})$$

$$\dots = \alpha \int_S \sum_{m\sigma l} \left[ (a_{\sigma 1l}^m a_{\sigma 3l}^m + b_{\sigma 1l}^m b_{\sigma 3l}^m) (\vec{M}_{\sigma 1l}^m \times \vec{N}_{\sigma 3l}^m - \vec{M}_{\sigma 3l}^m \times \vec{N}_{\sigma 1l}^m) \right] \cdot d\vec{S} \quad (\text{A.61})$$

Defining:

$$\vec{r}_i \equiv \{\vec{\xi}_i, \vec{\eta}_i, \vec{\phi}_i\} \quad (\text{A.62})$$

For an infinitesimal dipole moment, the currents can be expressed as:

$$\vec{J}_1^e = \frac{\vec{p}_e}{A} \cdot \delta(\vec{r}_0) \quad (\text{A.63})$$

$$\vec{J}_1^m = \frac{\vec{p}_m}{A} \cdot \delta(\vec{r}_0) \quad (\text{A.64})$$

Where  $dV = Ad\xi d\eta d\phi$  is the volume element for toroidal coordinates.

$$A = \frac{d^2 \sinh \xi}{(\cos \xi - \cos \eta)^3} \quad (\text{A.65})$$

In that way:

Taking  $\vec{J}_e$  as a surface current at  $\xi = \xi_0$ :

$$\int_V (\vec{E}_2 \cdot \vec{J}_1^e - \vec{E}_1 \cdot J_2^e - \vec{H}_2 \cdot \vec{J}_1^m + \vec{H}_1 \cdot \vec{J}_2^m) dV = \int_S (\vec{E}_2 \cdot \vec{p}_e - \vec{H}_2 \cdot \vec{p}_m) dS \quad (\text{A.66})$$

For the electrical infinitesimal dipole ( $\vec{p}_m = \vec{0}$ ):

$$\int_S (\vec{E}_1 \times \vec{H}_2 - \vec{E}_2 \times \vec{H}_1) \cdot d\vec{S} = \int_S (\vec{E}_2 \cdot \vec{p}_e - \vec{H}_2 \cdot \vec{p}_m) dS \quad (\text{A.67})$$

$$\int_S (\vec{E}_1 \times \vec{H}_2 - \vec{E}_2 \times \vec{H}_1) \cdot d\vec{S} = \int_S (\vec{E}_2 \cdot \vec{p}_e) dS \quad (\text{A.68})$$

$$\int_S (\vec{E}_1 \times \vec{H}_2 - \vec{E}_2 \times \vec{H}_1) \cdot \hat{\xi} dS = \int_S (\vec{E}_2 \cdot \vec{p}_e) dS \quad (\text{A.69})$$

$$(\vec{E}_1 \times \vec{H}_2 - \vec{E}_2 \times \vec{H}_1) \cdot \hat{\xi} = (\vec{E}_2 \cdot \vec{p}_e) \quad (\text{A.70})$$

$$(\vec{E}_1 \times \vec{H}_2 - \vec{E}_2 \times \vec{H}_1) \cdot \hat{\xi} = a_{\sigma 3l}^m \vec{p}_e \cdot \vec{M}_{\sigma 3l}^m(\vec{r}_0) + b_{\sigma 3l}^m \vec{p}_e \cdot \vec{N}_{\sigma 3l}^m(\vec{r}_0) \quad (\text{A.71})$$

$$(a_{\sigma 1l}^m a_{\sigma 3l}^m + b_{\sigma 1l}^m b_{\sigma 3l}^m) (\vec{M}_{\sigma 1l}^m \times \vec{N}_{\sigma 3l}^m - \vec{M}_{\sigma 3l}^m \times \vec{N}_{\sigma 1l}^m) = a_{\sigma 3l}^m \vec{p}_e \cdot \vec{M}_{\sigma 3l}^m(\vec{r}_0) + b_{\sigma 3l}^m \vec{p}_e \cdot \vec{N}_{\sigma 3l}^m(\vec{r}_0) \quad (\text{A.72})$$



# B DRAWINGS

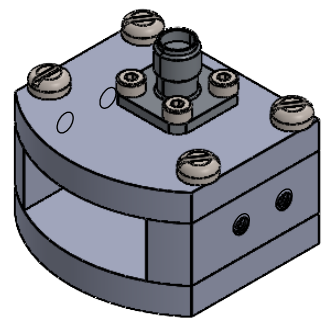
---

The following page present the drawing of the antenna used in this work.

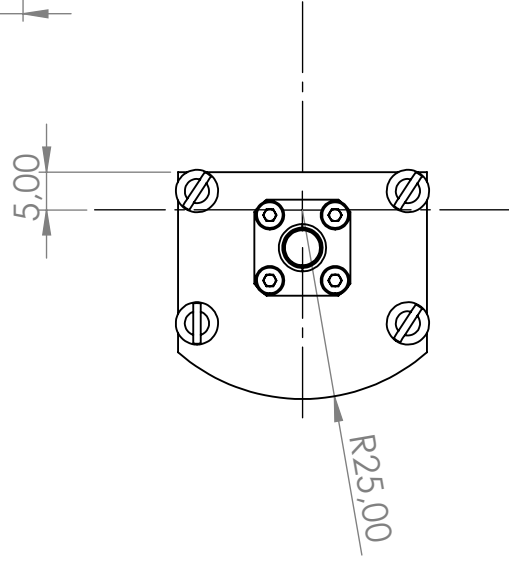
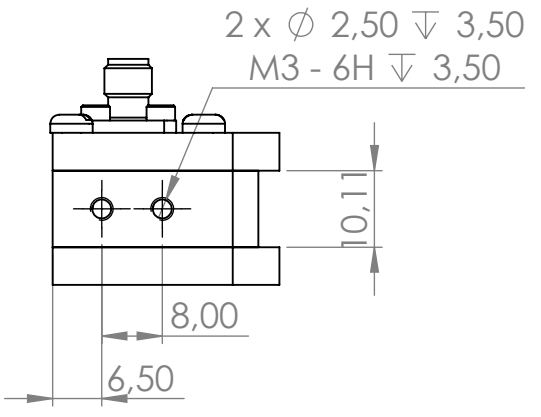
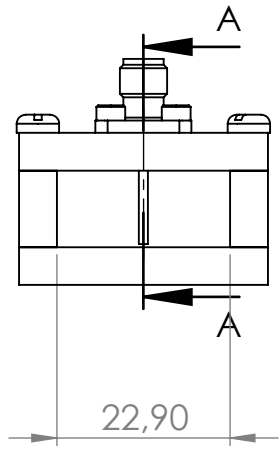
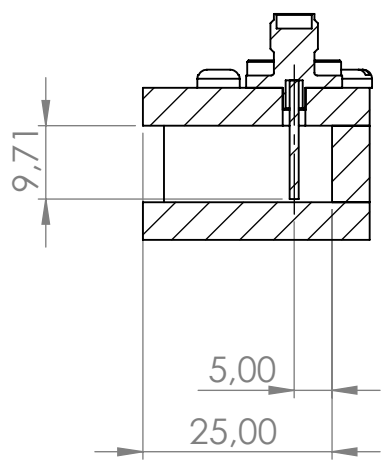
4 3 2 1

F

F



SECTION A-A



D

D

C

C

B

B

SE NÃO ESPECIFICADO:  
DIMENSÕES EM MILÍMETROS  
ACABAM. SUPERFÍCIE:  
TOLERÂNCIAS:  
LINEAR:  
ANGULAR:

ACABAMENTO:

REBARBAR E  
QUEBRAR  
ARESTAS  
AGUDAS

NÃO MUDAR ESCALA DO DESENHO

REVISÃO

	NOME	ASSINATURA	DATA	
DESEN.				
VERIF.				
APROV.				
MANUF				
QUALID				

TÍTULO:

DES. Nº

**WG\_cut**

A4

PESO:

ESCALA:1:1

FOLHA 1 DE 1

A

A

4 3 2 1